

AMERICAN UNIVERSITY OF BEIRUT

Design, Reconfiguration and Analysis of Antenna  
Systems for Mobile and IoT Devices

by

FATIMA ALZAHRAA BASSAM ASADALLAH

A dissertation  
submitted in partial fulfillment of the requirements  
for the degree of Doctor of Philosophy  
to the Department of Electrical and Computer Engineering  
of the Maroun Semaan Faculty of Engineering and Architecture  
at the American University of Beirut

Beirut, Lebanon  
April 2019

# AMERICAN UNIVERSITY OF BEIRUT

## Design, Reconfiguration and Analysis of Antenna Systems for Mobile and IoT Devices

by

FATIMA ALZAHRAA BASSAM ASADALLAH

Approved by:

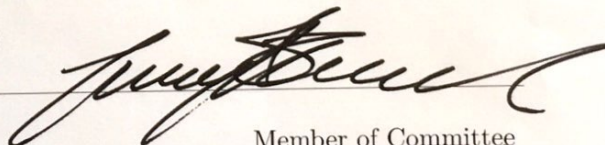
Prof. Zaher Dawy, Assistant Provost  
Electrical and Computer Engineering

Chair of Committee



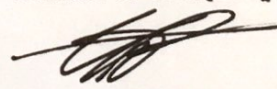
Prof. Joseph Costantine, Associate Professor  
Electrical and Computer Engineering

Advisor



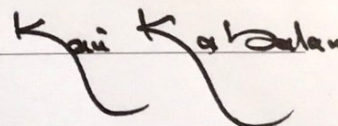
Prof. Ali Hajj, Professor  
Electrical and Computer Engineering

Member of Committee



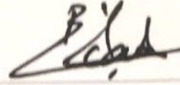
Prof. Karim Kabalan, Professor  
Electrical and Computer Engineering

Member of Committee



Prof. Riad Chedid, Professor  
Electrical and Computer Engineering

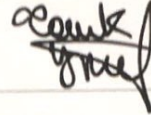
Member of Committee



---

Prof. Youssef Tawk, Assistant Professor  
Electrical and Computer Engineering

Member of Committee



---

Prof. Fabien Ferrero, Full Professor  
LEAT Laboratoire, University Cote D'Azur

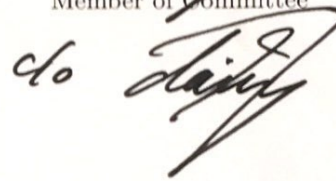
Member of Committee



---

Prof. Leonardo Lizzi, Associate Professor  
LEAT Laboratoire, University Cote D'Azur

Member of Committee



---

Date of thesis defense: April 17, 2019

# AMERICAN UNIVERSITY OF BEIRUT

## THESIS, DISSERTATION, PROJECT RELEASE FORM

Student Name: \_\_\_\_\_  
AsadAllah                      Fatima AlZahraa                      Bassam


Master's Thesis               Master's Project               Doctoral Dissertation

I authorize the American University of Beirut to: (a) reproduce hard or electronic copies of my thesis, dissertation, or project; (b) include such copies in the archives and digital repositories of the University; and (c) make freely available such copies to third parties for research or educational purposes.

I authorize the American University of Beirut, to: (a) reproduce hard or electronic copies of it; (b) include such copies in the archives and digital repositories of the University; and (c) make freely available such copies to third parties for research or educational purposes after: **One** \_\_\_ year from the date of submission of my thesis, dissertation or project.

Two \_\_\_ years from the date of submission of my thesis, dissertation or project.

Three  years from the date of submission of my thesis, dissertation or project.

  
Signature

17/5/2019  
Date

This form is signed when submitting the thesis, dissertation, or project to the University Libraries

# Acknowledgements

I would like first to thank God for all the benefits you have given me to accomplish my dissertation.

I am heartily thankful to my advisor Prof. Joseph Costantine for all his assistance and support during this work and throughout my graduate studies. He encouraged and guided me from start to finish in developing a deep understanding of the subject. His instructive comments and evaluation guided and challenged my thinking, substantially improving the dissertation outcome.

I would like to thank Prof. Youssef Tawk for his support and fruitful comments throughout my research.

I would like to thank Prof. Fabien Ferrero and Prof. Leonardo Lizzi from University Cote D'Azur for the internship opportunity they offered in the LEAT laboratory.

I would like to acknowledge my thesis committee members, Prof. Zaher Dawy, Prof. Ali Hajj, Prof. Karim Kabalan, Prof. Raid Chedid, Prof. Youssef Tawk, Prof. Fabien Ferrero and Prof. Leonardo Lizzi for their dedicated time and constructive comments. I am also greatly thankful to the Electrical and Computer Engineering Department and AUB University Research Board (URB).

My family and my love, no words can express my gratitude to them for their endless love, support and sacrifice. I would like to thank them for their continuous encouragements and believe in me.

I would like to thank Aline Eid, my first friend at AUB. As I always tell her, she is a gift from GOD. I would like to thank her for being such an honest friend.

I would like to thank all my other friends at AUB especially Nadine Abbass and Nour Kouzayha, in addition to all the RF lab members. Thank you guys for all the wonderful days we spent doing measurements, fabrication, soldering, meetings, organizing the lab, purchasing new equipment, etc. I wish this lab the best achievements and success.

# An Abstract of the Thesis of

Fatima AlZahraa Bassam AsadAllah for Doctor of Philosophy  
Major: Electrical and Computer  
Engineering

Title: Design, Reconfiguration and Analysis of Antenna Systems for Mobile and IoT Devices

With the rapid development of wireless communication systems, and the rise of the age of internet of things (IoT), the requirements on communication systems are increasing significantly. In fact, radio frequency (RF) front end systems will be responsible for the communication needs of billions of devices by 2025. Therefore, designers and researchers are seeking compact multi-functional transceiver systems that cater for the pressing wireless communication needs, while at the same time preserving the respective standards' requirements. The various transceiver components including antenna elements must be compact, adaptive, tunable, and at the same time high performing. Such requirements present a challenge for antennas and RF designers worldwide.

Therefore, this dissertation discusses a holistic solution that designs a full reconfigurable communication system for mobile and IoT devices. Such solution starts with an analysis of the different switching techniques and their effects on an antenna performance. More specifically, the impact of positive-intrinsic-negative (PIN) diodes, Radio Frequency micro-electromechanical switch (RF MEMS), varactors and digital tunable capacitors (DTC) on an antenna's gain, power dissipated, radiation efficiency, linearity and switches' biasing requirements are evaluated and compared. Such analysis allows antenna designers to always commit to an informed decision on the reconfiguring components choice during the early stages of the design process.

This analysis is first executed on a novel reconfigurable multiple input multiple output (MIMO) printed inverted F antenna (PIFA) system. The PIFA elements are reconfigured by relying on PIN diodes, RF MEMS, or varactors in order to cover the needed frequencies of operation, as well as radiation requirements that are necessary in mobile and compact terminals. In addition, the isolation between

the antenna elements of the proposed MIMO system is also reconfigured by relying on a reconfigurable band reject filter that is incorporated in the ground plane between the antenna elements. The reconfigurable frequency rejection achieved by this band reject filter relies on the same switching mechanisms as the MIMO PIFA elements. In addition, the isolation is reconfigured simultaneously as the reconfiguration of the radiating elements. It is proven in this dissertation that the proposed reconfigurable and dynamic isolation enhances the MIMO performance of the proposed system far beyond the capabilities of a multi-band static isolation filter. This technique's concept is proven and can be extended to other MIMO systems with a larger number of elements as expected and needed in modern communication systems.

With MIMO systems that are integrated with a dynamic isolation potential, this dissertation ventures into exploring additional reconfiguring components as well as various types of antenna components. The reconfiguration mechanisms investigated on the 2 element PIFA MIMO system are all analog switching mechanisms that regulate a direct current (DC) output to operate. While providing tuning and antenna current reconfiguration, a digitally tunable capacitor (DTC) relies on a 5-bit digital input to provide 32 states of antenna reconfiguration possibilities. Such technique can be integrated on the antenna structure or within its feeding network. As a result, we explore the possibility of shifting this reconfiguration technique into the feeding line of an antenna in order to achieve reconfiguration. A DTC based tunable filter is integrated within the feeding line of a slot antenna in order to tune its operating frequency. The resulting filtenna (filter+antenna) is now digitally tuned and can be easily software controlled. Such technique enables an IoT antenna designer to propose digitally tunable antennas for easier integration in a software defined or cognitive radio systems within a MIMO environment. The digitally tuned filtenna is also compared with a PIN diode or varactor tuned filtenna structures where digital tuning clearly establishes a superior performance.

As a result of this analysis, it is proven that the choice of a reconfiguring component directly impacts the antenna application environment within a MIMO setting. For example, long distance communications require mobile devices to exhibit a high radiation efficiency. Our analysis indicates that PIN diodes in that case must be avoided, while varactors have displayed the highest possible radiation efficiency at the expense of very high DC power consumption. A DTC or an RF MEMS represent a compromise in that case, while keeping in mind that DTC are digital with less needed DC biasing power. DTC can also be great candidates for integration with more compact devices such as wearable smart watches, or other small wearable accessories.

Taking this analysis to the next level and proving that it can be valid even with very compact antenna structures as well as for much lower frequency operations represents another challenge tackled in this dissertation. A three dimensional volumetrically folded antenna structure is proposed as an element in a MIMO

system for operation within the white spaces of the TV bands (575 MHz and 760 MHz). Such antenna element must be very compact exhibiting miniaturization ratios of 80% with radiation efficiencies that are between 40% and 62% can be proposed for cognitive radio in areas that lack the needed infrastructure such as rural areas, a distant refugee camp or in the aftermath of a disaster. It is shown in this dissertation as a result of our analysis that RF MEMS are perfect candidates for such structures. They enable the antenna to be viably operational at such low UHF bands while at the same time preserving acceptable radiation efficiencies.

All the proposed techniques have been implemented into antenna components that are suitable for integration in a compact IoT device. Such antenna component requires an RF transceiver that is the backbone of any communication system. Hence, the last part of this dissertation tackles the design of a reconfigurable transceiver system that can cater for the evolving need of a dynamic MIMO IoT communication system. This reconfigurable transceiver is designed to operate at tunable frequencies within the microwave range and for multiple modulation schemes such as Quadrature Phase Shift Keying (QPSK) and Direct Sequence Spread Spectrum (DSSS). The transceiver architecture is optimized to exhibit a tunable response while minimizing noise and power requirements. As a result, various components are tuned by relying on the same switching mechanisms implemented within the antenna elements. Furthermore, the transceiver system benefits from wideband components that tackle all the needed ranges of the microwave bands. Hence, this dissertation proposes a novel modern transceiver architecture that benefits from both reconfigurable and wideband technologies in order to provide the optimal solution for an IoT MIMO communication system. The entire system along with the various antennas' front ends have been fabricated and measured to verify predicted and simulated results with great agreement. In addition, it is verified that the complete proposed communication systems verify the applicable standards as presented in the literature.

As a conclusion, this dissertation analyzes the impact of reconfigurable components on the antennas and the full communication systems of any portable and compact IoT terminal. In addition, recommendations are presented for future extensions of this work into a variety of applications and devices that cater for the future of communication well within 5G and beyond.



# Contents

<b>Acknowledgements</b>	<b>v</b>
<b>Abstract</b>	<b>vi</b>
<b>1 Introduction</b>	<b>1</b>
1.1 Thesis Objectives and Contributions . . . . .	3
1.2 Organization of the Dissertation . . . . .	4
<b>2 Literature Review</b>	<b>6</b>
2.1 Introduction . . . . .	6
2.2 Review of Previously Designed Reconfigurable MIMO Antenna Systems . . . . .	6
2.2.1 Reconfigurable Antennas . . . . .	6
2.2.2 MIMO Antenna Systems . . . . .	7
2.2.3 MIMO Antenna Systems with Enhancements Techniques . . . . .	10
2.3 Review of Previously Designed Reconfigurable Transceiver Systems	11
<b>3 An Isolation Enhanced MIMO PIFA System with Multiple Re-configuration Techniques</b>	<b>13</b>
3.1 Introduction . . . . .	13
3.2 PIFA ANTENNA DESIGN USING DIFFERENT RECONFIGURABLE COMPONENTS . . . . .	15
3.2.1 PIFA Antenna Design using PIN Diode . . . . .	15
3.2.2 PIFA Antenna Design using RF MEMS . . . . .	18
3.2.3 Varactor based Reconfigurable PIFA Design . . . . .	21
3.3 Impact of Switches' Integration on The Design and Characteristics of the Reconfigurable PIFA . . . . .	23
3.3.1 Number of switches . . . . .	23
3.3.2 Biasing . . . . .	23
3.3.3 RF Power Dissipated . . . . .	23
3.3.4 Radiation Efficiency . . . . .	24

3.3.5	Non-Linearity . . . . .	24
3.3.6	Reliability . . . . .	25
3.3.7	Bandwidth . . . . .	25
3.4	MIMO Implementation of The Reconfigurable PIFA System . . .	25
3.4.1	MIMO System Evaluation Basics . . . . .	26
3.4.2	Design of a reconfigurable MIMO PIFA system with a multi- band reject filter for isolation enhancement . . . . .	27
3.4.3	Reconfiguration using Varactors . . . . .	29
3.4.4	MIMO Implementation using PIN diodes . . . . .	32
3.4.5	MIMO Implementation using RF MEMS . . . . .	33
3.4.6	Impact of Switches on MIMO System Performance . . . .	33
3.5	Discussion . . . . .	36
<b>4</b>	<b>Analysis of Different Switching Techniques on a Novel Filtenna Design</b>	<b>37</b>
4.1	Introduction . . . . .	37
4.2	Design Guidelines for the Coupled-Line Tunable Bandpass Filter . . . . .	38
4.3	DTC-Tuned Filtenna . . . . .	39
4.4	Filtenna Design Using Different Reconfigurable Components . . . . .	43
4.4.1	Filtenna Design using PIN Diode . . . . .	43
4.4.2	Varactor based tunable filtenna design: . . . . .	44
4.5	Impact of Switches' Integration on the Design and Characteristics of the Filtenna . . . . .	47
4.5.1	Biasing . . . . .	47
4.5.2	RF Power Dissipated . . . . .	47
4.5.3	Radiation Efficiency . . . . .	48
4.5.4	Non-Linearity . . . . .	48
4.6	Discussion . . . . .	49
<b>5</b>	<b>Multi-layered Folded Miniaturized Reconfigurable Antenna</b>	<b>50</b>
5.1	Introduction . . . . .	50
5.2	Antenna Topology and Design . . . . .	51
5.2.1	Meandered Loop Design . . . . .	51
5.2.2	Reconfigurable Antenna Performance . . . . .	52
5.2.3	Folding the reconfigurable structure . . . . .	54
5.2.4	Enhancing the Matching Network . . . . .	55
5.3	Reconfigurable Multi-layered Folded Antenna . . . . .	57
5.3.1	Final Design . . . . .	57
5.3.2	Feeding . . . . .	58
5.3.3	Results and Measurements . . . . .	58
5.4	Discussion . . . . .	60

<b>6</b>	<b>A Digitally Reconfigurable Volumetrically Folded Miniaturized Antenna</b>	<b>63</b>
6.1	Introduction . . . . .	63
6.2	A Volumetrically Folded Antenna Design . . . . .	64
6.2.1	Folded Two Arms Bowties . . . . .	64
6.2.2	Semi-Bowtie Design . . . . .	65
6.3	Digitally Reconfigurable Semi Bowtie Antenna . . . . .	67
6.3.1	Reconfigurable Semi-Bowtie . . . . .	67
6.3.2	Measurements and Results . . . . .	70
6.4	Discussion . . . . .	74
<b>7</b>	<b>Novel Reconfigurable Transmit/Receive System</b>	<b>75</b>
7.1	Introduction . . . . .	75
7.2	Block Diagram of the Proposed TX/RX System . . . . .	75
7.3	Design Considerations for the TX/RX System system . . . . .	76
7.4	Receiver Performance Evaluation . . . . .	77
7.5	Receiver Design . . . . .	78
7.6	Transmitter Design . . . . .	79
7.7	Transmit/Receive Design . . . . .	79
7.8	Conclusion . . . . .	82
<b>8</b>	<b>Conclusions and Future Work</b>	<b>83</b>
8.1	Future Work . . . . .	84
<b>A</b>	<b>Abbreviations</b>	<b>86</b>

# List of Figures

2.1	Reconfigurable Antenna Design [1] . . . . .	7
2.2	Reflection Coefficient in dB [1] . . . . .	7
2.3	The reconfigurable antenna design [2] . . . . .	7
2.4	The VSWR of the antenna design [2] . . . . .	8
2.5	The radiation efficiency of the antenna for different capacitance value [2] . . . . .	8
2.6	The Four Folded MIMO Antenna System Design [3] . . . . .	8
2.7	The Reflection Coefficient in dB [3] . . . . .	9
2.8	The MIMO Antenna System Design [4] . . . . .	9
2.9	The Reflection Coefficient in dB [4] . . . . .	9
2.10	The MIMO Antenna System Design [5] . . . . .	10
2.11	The Reflection Coefficient in dB [5] . . . . .	10
2.12	The Eight MIMO Antenna System Design [6] . . . . .	11
2.13	The Reflection Coefficient in dB [6] . . . . .	11
2.14	Multistandard transceiver Architecture [7] . . . . .	12
2.15	Reconfigurable transceiver Architecture [8] . . . . .	12
3.1	Reconfigurable PIFA structure along with its fabricated prototype (a) 3D view, (b) side view, (c) detailed dimensions, and (d) fabricated prototype . . . . .	16
3.2	The simulated and measured reflection coefficient in dB for different switches configurations using pin diodes . . . . .	17
3.3	The simulated and measured radiation pattern of the reconfigurable PIFA for $\phi = 90^\circ$ at (a) 1.8 GHz when S2 is ON, (b) 2.1 GHz when S1 is ON, (c) 900 MHz when M1 is ON, (d) 1.8 GHz when M2 is ON, (e) 900 MHz when the varactor has an equivalent capacitance of 0.94pF and (f) 1.8 GHz when the varactor has an equivalent capacitance of 0.74 pF . . . . .	17
3.4	The reconfigurable PIFA structure (a) using RF-MEMS and (b) using varactor . . . . .	17
3.5	The simulated and measured reflection coefficient in dB for the different biasing of the RF MEMS . . . . .	19
3.6	The simulated and measured reflection coefficient in dB for different biasing voltage of the varactor . . . . .	22

3.7	Implementation of MIMO reconfigurable antenna prototype (a) using pin diodes and multiband reject slots, (b) using varactors and reconfigurable varactor-based band reject, (c) using RF-MEMS and (d) using pin diode . . . . .	28
3.8	The comparison in isolation values between the various operating frequencies at the different elements configurations . . . . .	28
3.9	(a) The filter prototype, (b) the current paths before the addition of any active component, (c) the equivalent LC circuit model of the presented filter, (d) detailed dimensions of the various slots along with the location of the integrated varactor and resistor . . . . .	30
3.10	Comparison between the transmission and reflection coefficients of the proposed LC equivalent circuit and the filter 3D structure . . . . .	31
3.11	(a) The front side and (b) bottom side of the reconfigurable band reject filter structure . . . . .	31
3.12	The variation of the transmission coefficient in dB for different varactor capacitance . . . . .	32
3.13	The active reflection coefficient for the various configurations of the MIMO system with (a) pin diode integration, (b) RF-MEMS integration and (c) varactor integration . . . . .	34
3.14	The diversity gain when S1 is ON and S2 is OFF at 2.1 GHz . . . . .	35
4.1	Equivalent circuit model schematic of the employed DTC [9] . . . . .	38
4.2	Structure of the tunable coupledline bandpass filter . . . . .	39
4.3	A fabricated prototype of the tunable DTC based coupledline bandpass filter . . . . .	39
4.4	Simulated S-parameters of the tunable DTC based coupled-line bandpass filter . . . . .	40
4.5	Measured and Simulated S-parameters of the tunable coupledline bandpass filter . . . . .	41
4.6	Structure of the wideband antenna . . . . .	41
4.7	Fabricated prototype of the wideband antenna . . . . .	41
4.8	Simulated and measured reflection coefficient of the wideband antenna . . . . .	42
4.9	Structure of the tunable filtenna . . . . .	42
4.10	Structure of the tunable filtenna . . . . .	42
4.11	Measured reflection coefficient of the tunable filtenna . . . . .	43
4.12	Normalized radiation pattern of the filtenna for different states . . . . .	43
4.13	Radiation efficiency along with the gain of the filtenna for different states . . . . .	44
4.14	RF power dissipated for various switches over different states . . . . .	44
4.15	Pin diode and varactor based Filtenna . . . . .	45
4.16	The simulated and measured reflection coefficient in dB for different switches configurations using pin diode . . . . .	45

4.17	The radiation pattern of the filtenna for $\phi = 90^\circ$ and $\phi = 0^\circ$ at 1.65 GHz in ON state and 2.56 GHz in OFF state . . . . .	45
4.18	Radiation efficiency along with the gain of the filtenna for different switches techniques . . . . .	46
4.19	The simulated and measured reflection coefficient in dB for different switches configurations using varacator . . . . .	46
4.20	The radiation pattern of the filtenna for $\phi = 90^\circ$ and $\phi = 0^\circ$ for different varactor capacitance . . . . .	47
5.1	Meandered loop antenna (a) cascaded layers, (b) radiating part, and (c) transmission line . . . . .	52
5.2	Meandered loop antenna (a) reflection Coefficient and (b) radiation pattern . . . . .	53
5.3	Reconfigurable loop antenna (a) loop antenna along with the extended lines, (b) matching line, (c) reflection coefficient results and (d) radiation pattern around 760 MHz . . . . .	53
5.4	Electric Coupled Field for (a) the non-folded design and (b) the folded one . . . . .	54
5.5	Folded loop antenna design (a) left side view, (b) right side view and (c) matching line . . . . .	54
5.6	The folded loop antenna (a) reflection coefficient, (b) 3D radiation pattern at 575 MHz and (c) 3D radiation pattern around 760 MHz . . . . .	55
5.7	Methodology to choose the optimal L- matching network . . . . .	56
5.8	Smith chart matching of the (a) $Z_{OFF}$ and (b) $Z_{ON}$ with the final TL and shunt . . . . .	57
5.9	Final Matching Network . . . . .	57
5.10	The antennas reflection coefficient in dB after adding the L-matching network . . . . .	58
5.11	Loop Antenna Design, (a) antenna top view, (b) folds view and (c) layers composition view . . . . .	59
5.12	Current path for (a) RF MEMS OFF and (b) RF MEMS ON . . . . .	59
5.13	Final Prototype . . . . .	60
5.14	Small Antenna Measurements . . . . .	60
5.15	Simulated and Measured Reflection Coefficient in dB for different switch state . . . . .	61
5.16	Simulated and Measured radiation patterns (a) Co-polarization at 575 MHz in the x-z plane, (b) cross-polarization at 575 MHz in the x-z plane, (d) cross-polarization at 575 MHz in the y-z plane, (c) Co-polarization at 575 MHz in the y-z plane, (e) Co-polarization at 760 MHz in the x-z plane, (f) cross-polarization at 760 MHz in the x-z plane, (g) Co-polarization at 760 MHz in the y-z plane, (h) cross-polarization at 760 MHz in the y-z plane. . . . .	62

6.1	Basic bowtie antenna (a) design, (b) reflection coefficient and (c) gain plot . . . . .	65
6.2	Folded two arm bowtie with slot and slit integration . . . . .	66
6.3	Semi bowtie antenna (a) design, (b) reflection coefficient and (c) gain pattern at 868 MHz . . . . .	67
6.4	3D folded semi-bowtie design . . . . .	68
6.5	Input impedance of the antenna (a) Real and (b) Imaginary . . .	68
6.6	Semi Bowtie Antenna design (a) left tilted 3D view presenting the left folded side and (b) right tilted 3D view representing the right folded side . . . . .	69
6.7	Reflection coefficient of the antenna at different states . . . . .	70
6.8	Fabricated prototype of the semi bowtie antenna design . . . . .	71
6.9	Small antenna measurements techniques for the bowtie antenna design . . . . .	72
6.10	Simulated and Measured Reflection Coefficient in dB for different DTC States . . . . .	73
6.11	The radiation pattern of the antenna at (a) 2.1 GHz, (b) 1.8 GHz, (c) 1 GHz, (d) 915 MHz and (e) 868 MHz from different DTC state at $\phi 90^\circ$ . . . . .	73
7.1	Block Diagram of the proposed TX/RX System . . . . .	76
7.2	Receiver Fabricated System . . . . .	79
7.3	Testing Senario . . . . .	80
7.4	Transmitter Fabricated System . . . . .	80
7.5	Standard Spectral Mask [10] . . . . .	80
7.6	Transmitter testing Scenario . . . . .	81
7.7	Assembled TX/RX System . . . . .	81

# List of Tables

3.1	The Operating frequencies for various switches configurations along with the corresponding maximum gains, radiation efficiencies and RF power dissipated for pin diodes . . . . .	18
3.2	Operation frequencies for various switches configurations along with corresponding maximum gains, radiation efficiencies and RF power dissipated for RF MEMS . . . . .	20
3.3	Operation frequencies for various switches configurations along with corresponding maximum gains, radiation efficiencies and RF power dissipated for varactors . . . . .	20
3.4	The radiation efficiency for various switches . . . . .	24
3.5	Bandwidth comparison between different switches . . . . .	26
3.6	The inductance and capacitance values for the three current paths . . . . .	30
3.7	The correlation coefficient for the MIMO system with (a) pin diode integration, (b) RF-MEMS and (c) varactors . . . . .	33
3.8	The MEG ratios for the two antenna elements of MIMO system with (a) the pin diode integration, (b) RF-MEMS inegration and (c) varactor integration . . . . .	35
3.9	Comparative Analysis between pin diodes, MEMS and varactors . . . . .	36
5.1	Comparative table between the proposed design and literature . . . . .	61
6.1	Antenna radiation efficiency and size reduction for various DTC states along with its corresponding frequency . . . . .	71
6.2	Comparative table between the proposed design and literature . . . . .	72
7.1	Targeted Commercial Wireless Standard Key Specifications . . . . .	77
7.2	Receiver Requirements . . . . .	78
7.3	Receiver Spread Sheet . . . . .	78
7.4	Receiver Main Performance Evaluation . . . . .	78
8.1	Comparison between Different Switching Techniques . . . . .	84



# Chapter 1

## Introduction

The number of connected devices is expected to increase significantly to reach 75.44 billions by 2025 [11], establishing the Internet of things (IoT) as a fact of our reality and no longer a future vision. As a result, new challenges face antenna and radio frequency (RF) circuit designers. Hence a need for the design of compact multi-functional transceiver systems arises in order to satisfy the pressing wireless communication needs, while at the same time preserving the respective standards' requirements. The various transceiver components including antenna elements must be compact, adaptive, tunable, and at the same time high performing.

Proposed antenna designs that are able to operate at a multitude of frequencies are defined as multiband antennas. Various techniques are used to ensure this multiband performance such as truncation, folding, slots integration and vias incorporation [12]. In addition, the integration of antenna systems in portable devices necessitates that such antennas exhibit compact sizes without compromising their radiation characteristics such as gain, radiation efficiency and power radiated [13–18]. However, a trade off always exists between the multiband performance and antennas' dimensions. Therefore, reconfigurable antennas are presented as solution where a single antenna element operates at various frequencies with a reduced landscape and with the same radiation characteristics. Furthermore, reconfigurable antennas are also able to reconfigure their radiation patterns, polarization or exhibit a combination of adaptive properties on demand and based on the user's request.

In fact, by definition, a reconfigurable antenna is an antenna that changes the radiating fields of the antennas aperture [19]. It is based on a change in the current distribution or the radiating edges. There exist different types of antennas' reconfiguration. An antenna that is able to change its polarization is called polarization reconfigurable antenna; an antenna that changes its radiation pattern is called a pattern reconfigurable antenna, and the antenna that changes its frequency of operation is called frequency reconfigurable antenna [20]. Frequency reconfigurable antennas appear as a solution that can achieve more compact structures

with a great performance especially in comparison to multiband antennas. Their operation allows the change of their operational frequencies on demand, based on the specifications of the needed applications. Reconfiguring antenna structures is achieved through various means, where electrical switches constitute a dominant choice [2, 21–34]. Examples of electrical switches are positive intrinsic negative (PIN) diodes, varactors, radio frequency micro-electromechanical systems (RF MEMS), or digital tunable capacitors (DTC) [2, 20–22]. However, choosing the appropriate switching technique is always one of the main challenges facing an antenna designer.

For antennas specifically purposed for integration within small portable devices, additional miniaturization and size reduction are required. Several miniaturized antennas have been proposed in literature for implementation in portable devices for the internet of things [35–38]. However, designing a miniaturized antenna comes with a cost on the antennas radiation efficiency. Furthermore, modern IoT devices must be equipped with multiple connectivity options. New wireless standards for Low Power Wide Area Networks (LPWAN), such as LoRa or Sigfox, well match the low data-rate needed by IoT applications. In addition, GPS and Bluetooth are needed for localization and communication with personal objects (e.g., mobile phones). To that extent, a compact reconfigurable frequency operation that allows the IoT device’s antenna to communicate over multiple bands is required. It is important to note here that a reconfigurable antenna design must take into consideration the different characteristics of the integrated reconfiguring component and its effect on the radiation performance of the antenna itself.

Furthermore, and to fit within the IoT environment, reconfigurable antennas are integrated in a Multiple input multiple output (MIMO) system in order to increase the capacity and reduce the multipath effects. This method is essential for efficient wireless communication applications and it is especially needed for antenna integration into portable devices. Several MIMO antenna designs are investigated and presented in literature [3–6, 39–46] where various techniques are proposed to improve the isolation between the different antenna elements. One of the separation techniques that is used in [5] is based on introducing two stubs and one slot in the partial ground plane. Orthogonality between elements has also been used as a technique for better isolation [42]. However, with the enormous increase in the number of connected devices, increased isolation is a need.

For any communication system that is terminated with an antenna element, an RF transceiver is required. A full transceiver system is composed of a transmitter and a receiver system that entail a multitude of cascaded of RF components and a digital signal processing (DSP) unit [?]. Within the transmitter, the information is modulated in the DSP part and then converted into a radio frequency wave in the RF front end part in order to be transmitted by the antenna in free space. At the receiver side, the antenna captures the RF signal; then, the RF front end converts it back to its modulated form to be demodulated and extracted in the

DSP part. A transmitter is composed of a filter, amplifier, up converter mixer, power amplifier, and an antenna while a receiver starts with an antenna, followed by a low noise amplifier, down converter mixer, filter and variable gain amplifier . For a full transceiver system, the transmitter and the receiver are connected to a single antenna through a duplex or a circulator. In order to achieve a reconfigurable transceiver, all frequency dependent components are either wide band to cover the entire band of operation or frequency reconfigurable. Having a closer look on the components, reconfiguration must be applied to the filter and antenna components, while the remaining components can remain wide band.

## 1.1 Thesis Objectives and Contributions

The dissertation objectives are divided into three main parts. The first objective is based on analyzing different switching techniques and their effect on an antenna performance. The second objective is based on implementing the analysis findings and test its functionality by further designing reconfigurable antennas under extreme miniaturization conditions. The last objective of this dissertation tackles the design of a reconfigurable transceiver system that caters for the evolving need of a dynamic MIMO IoT communication system.

The major contributions of this work reside in the following points:

### 1- Analysis of Analog Switching Techniques on a Novel MIMO PIFA System

Objective 1: Analyzing MIMO PIFA Performance due to Different Analog Switches Integration.

Objective 2: Implementing a Novel Reconfigurable Isolation Technique.

### 2- Analysis of Various Analog and Digital Switching Techniques on a Novel Filtenna

Objective 3: Analyzing Filtenna Performance due To Different Switches Integration.

Objective 4: Increasing filtering ability of a signal by adding a filter into the feeding line of the antenna.

Objective 5: Improving reconfiguration ability and reducing its effect through the integration of a reconfiguring component within the feeding line of an antenna.

### 3- Validation of Analysis on Miniaturized Antenna Structures

Objective 6: Implementing the analysis finding and testing its functionality by further designing reconfigurable antennas under extreme miniaturization condi-

tions.

Objective 7: Implementing Novel Reconfigurable Volumetric Miniaturization Technique in order to ensure optimal size reduction within a limited landscape..

#### **4- Design of a Novel Reconfigurable Transceiver**

Objective 8: Assembling the transceiver with the reconfigurable antennas and test the performance of the full system under various reconfiguration techniques.

## **1.2 Organization of the Dissertation**

The dissertation is organized as follows:

Chapter 2 presents a comprehensive literature review on existing approaches considering MIMO systems, miniaturized reconfigurable antennas, reconfigurable filtennas and reconfigurable transceivers for mobile systems and IoT devices. For each section, the proposed approaches, objectives and contributions are highlighted and compared. Finally, the main contributions of this dissertation are compared to the literature.

Chapter 3 presents the analysis of different analog switching techniques on a novel reconfigurable MIMO PIFA system. The PIFA elements are reconfigured by relying on PIN diodes, RF MEMS, or varactors in order to cover the needed frequencies of operation, as well as radiation requirements that are necessary in mobile and compact terminals. In addition, this chapter discusses a novel reconfigurable isolation technique between the antenna elements for the proposed MIMO system. It is proven in this chapter that the proposed reconfigurable and dynamic isolation enhances the MIMO performance of the proposed system far beyond the capabilities of a multi-band static isolation filter. This technique's concept is verified and can be extended to other MIMO systems with a larger number of elements as expected and needed in modern communication systems.

Chapter 4 highlights the possibility of shifting the reconfiguration techniques into the feeding line of an antenna in order to reduce the effect of reconfiguring components on the antenna performance. An additional digital switch is investigated in order to study its impact on the antenna performance. Therefore, this chapter discusses a novel DTC based tunable filter that is integrated within the feeding line of a slot antenna in order to tune its operating frequency. The resulting filtenna (filter+antenna) is digitally tuned and can be easily software controlled. Such technique enables an IoT antenna designer to propose digitally tunable antennas for easier integration in a software defined or cognitive radio systems within a MIMO environment. The digitally tuned filtenna is also compared with a PIN diode or varactor tuned filtenna structures where digital tuning clearly establishes a superior performance.

Chapter 5 illustrates the ability of this method to be applied in extreme miniaturization techniques. A three dimensional multilayered folded antenna structure is proposed as an element in a MIMO system for operation within the white spaces of the TV bands (575 MHz and 760 MHz). Such an antenna element must be very compact exhibiting miniaturization ratios of 80% with radiation efficiencies that vary between 40% and 62%. This reconfigurable element can be proposed for cognitive radio in areas that lack the needed infrastructure such as rural areas, a distant refugee camp or in the aftermath of a disaster. It is shown in this Chapter as a result of our analysis that RF MEMS are perfect candidates for such structures. They enable the antenna to be viably operational at such low UHF bands while at the same time preserving acceptable radiation efficiencies.

Chapter 6 shows the ability of the DTC to achieve reconfiguration in addition to its tunability. A three dimensional volumetrically folded antenna structure is proposed as an element in a MIMO system for operation at ISM bands, GSM and LTE. Such an antenna element must be very compact exhibiting miniaturization ratios of 84% with radiation efficiencies above 88%. It can be proposed for IoT devices. It is shown in this Chapter as a result of our analysis that DTC are perfect candidates for such structures.

Chapter 7 proposes a novel modern transceiver architecture that benefits from both reconfigurable and wideband technologies in order to provide the optimal solution for an IoT MIMO communication system. The assembly of a reconfigurable transceiver system with a reconfigurable miniaturized antenna completes this thesis with a full communication system that is suitable for IoT integration.

Finally, Chapter 8 summarizes the main contributions of this dissertation. Moreover, it identifies the state-of-art RF systems for shortcomings wireless technologies and highlights the needs for enhancing design approaches in order to facilitate the implementation of reconfigurable transceiver systems in upcoming wireless networks.

# Chapter 2

## Literature Review

### 2.1 Introduction

In this chapter, a general overview of the literature is presented. Such overview discusses implemented concepts of reconfigurable antenna designs and MIMO systems for incorporation within miniaturized devices and mobile terminals. Miniaturization techniques merged with reconfiguration mechanisms are presented and analyzed. In addition, the implementation of a full transceiver system within a communication device is also detailed in this chapter through available resources in the literature.

### 2.2 Review of Previously Designed Reconfigurable MIMO Antenna Systems

#### 2.2.1 Reconfigurable Antennas

A frequency reconfigurable antenna design is presented in Fig 2.1. This antenna requires three switches in order to configure its operation to reach the desired frequencies. As a result, the authors resort to two PIN diodes in order to accomplish the required functionality. The switches are positioned as shown in Fig. 1. The reflection coefficient of the antenna design is presented in Fig 2.2 [1]. The antenna operates at 700 MHz and 2.4 GHz when both switches are off. When the switch S1 is OFF and the switch S2 is ON the antenna's resonance shifts to 900 MHz and 2.1 GHz. When only S1 is ON the antenna resonates solely at 1.8 GHz. The antenna's dimension are  $1 * 5 * 125mm^3$ .

Another example of a compact frequency reconfigurable antenna is presented in [2]. A reconfigurable antenna is presented for internet of things application as shown in Fig. 2.3 [2]. It operates at 700 MHz and 900 MHz for LTE and GSM applications at its lower band, a middle band for DCS/PCS, UMTS, LTE 1800/2600 (MB); and high band for emerging 3.5 GHz standard (HB) as shown

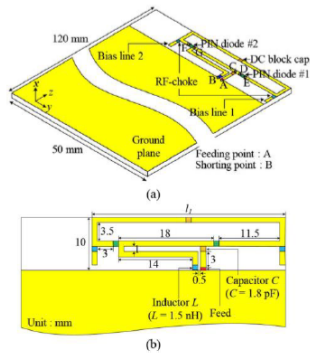


Figure 2.1: Reconfigurable Antenna Design [1]

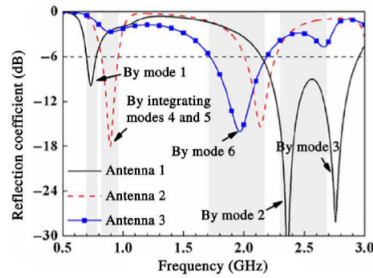


Figure 2.2: Reflection Coefficient in dB [1]

in Fig.2.4. For reconfiguration, a digitally tunable capacitor (DTC) is used. The radiation efficiency ranges between 40 and 60 % as presented in Fig. 2.5 [2]. The antennas dimensions are  $40 * 10 * 6mm^3$ .

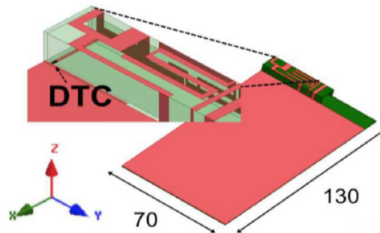


Figure 2.3: The reconfigurable antenna design [2]

## 2.2.2 MIMO Antenna Systems

### Wideband 4x4 MIMO System

A four element MIMO antenna system is viewed in Fig 2.6. The antenna element is a folded antenna design with  $10 * 10 * 5mm^3$  dimensions. The antenna system

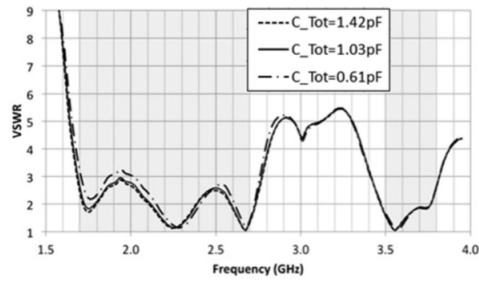


Figure 2.4: The VSWR of the antenna design [2]

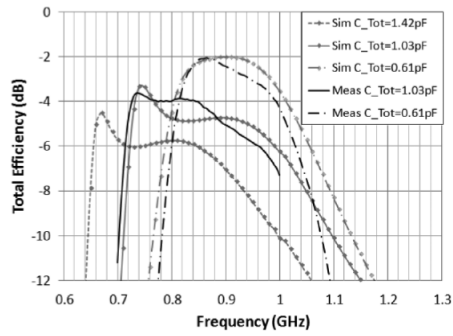


Figure 2.5: The radiation efficiency of the antenna for different capacitance value [2]

has a wideband performance ranging from 1.84 GHz till 2.69 GHz. So, it can cover the GSM1900, LTE2300 and LTE2500 systems for mobile terminals. Fig 2.7 represents the reflection coefficient of the antenna element. In the MIMO system, the antennas are separated by  $128 * 58mm^2$  distance. The isolation between the antenna elements is less than -14.5 dB over the entire operational range and the correlation is maintained below 0.03.

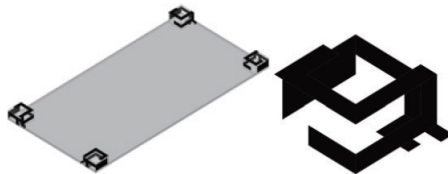


Figure 2.6: The Four Folded MIMO Antenna System Design [3]

### Frequency Reconfigurable MIMO System

A reconfigurable MIMO antenna system is introduced in Fig 2.8. The antenna is of  $1 * 5 * 125mm^3$  dimensions. Two pin diodes are integrated on the radiator



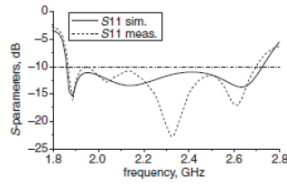


Figure 2.7: The Reflection Coefficient in dB [3]

part to insure frequency operation over the desired band. When the switches S1 and S2 are ON, the antenna operates at 770 MHz. The antenna resonates at 850 MHz and 1.5 GHz when both switches are OFF as represented in Fig 2.9. The MIMO system is implemented by separating two antenna elements by 260 mm distance. The isolation between the elements is less than -20 dB over the entire operational frequency. Also, the correlation coefficient is less than 0.07.

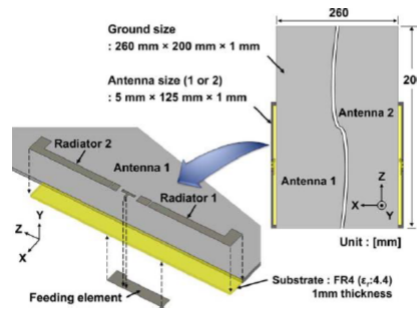


Figure 2.8: The MIMO Antenna System Design [4]

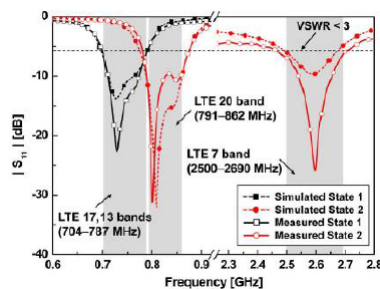


Figure 2.9: The Reflection Coefficient in dB [4]

## 2.2.3 MIMO Antenna Systems with Enhancements Techniques

### T-shaped Isolation Enhancement Technique for Mobile MIMO System

A MIMO antenna is presented in Fig 2.10 for 770 MHz band operation for LTE applications. A T-shaped common radiator is used between the two antenna elements. This radiator allows the high isolation between the antenna elements with lower separation distances. The antenna is meandered based with  $5 * 15 * 60mm^3$  dimensions. Such antenna operates at 770 MHz as presented in Fig 2.11. The antennas are separated by 27 mm distance that is equivalent to the T-shaped common radiator width. The isolation is -19 dB with an envelope correlation coefficient of 0.04.

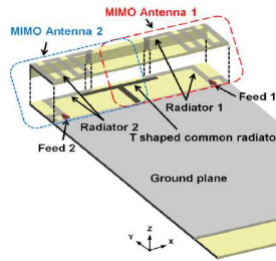


Figure 2.10: The MIMO Antenna System Design [5]

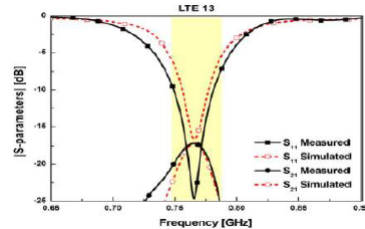


Figure 2.11: The Reflection Coefficient in dB [5]

### A Miniaturized Extremely Close-Spaced Four-Element Dual-Band MIMO Antenna System

A miniaturized design of a four-element dual-band multiple-input-multiple-output (MIMO) antenna system is shown in Fig. ???. The dual-band function is obtained by etching an L slot in the radiating patch. The edge-to-edge elements spacing is only  $0.023\lambda$ . A decoupling structure consisting of cross-shaped metal strips shorted to the ground plane using vias is first introduced. Then, metalized walls are used to enhance the isolation level by realizing the pattern diversity. The

measured resonant frequencies are centered at 3.5 and 5.7 GHz with bandwidths of 58 and 43 MHz, peak gains of 2.7 and 2.85 dBi, and peak efficiencies of 63% and 65%, respectively. A considerable measured mutual coupling reduction of 10.8 dB in the lower band and 15.6 dB in the upper band is realized. The overall size of the design is  $0.41\lambda * 0.41\lambda * 0.04\lambda$  with minimum isolation levels of 18.4 and 22.7 dB in the lower and upper bands, respectively. The envelope correlation coefficient is lower than 0.08 across both operating bandwidths. The measured results validate the good diversity performance of the MIMO system.

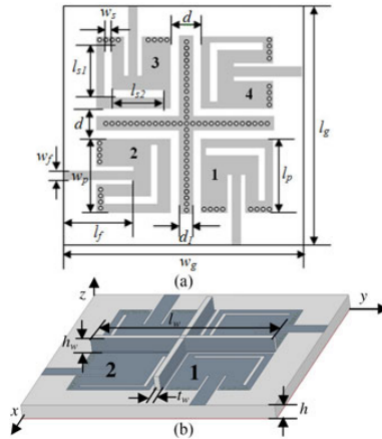


Figure 2.12: The Eight MIMO Antenna System Design [6]

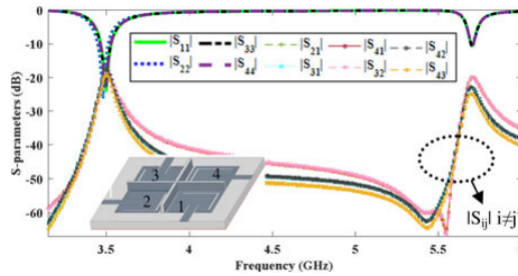


Figure 2.13: The Reflection Coefficient in dB [6]

## 2.3 Review of Previously Designed Reconfigurable Transceiver Systems

The design of a transceiver system and its implementation for a specific frequency operation has been discussed extensively in the literature. For example, in [7], a multistandard single band transceiver design is investigated. Fig. 2.14 shows the

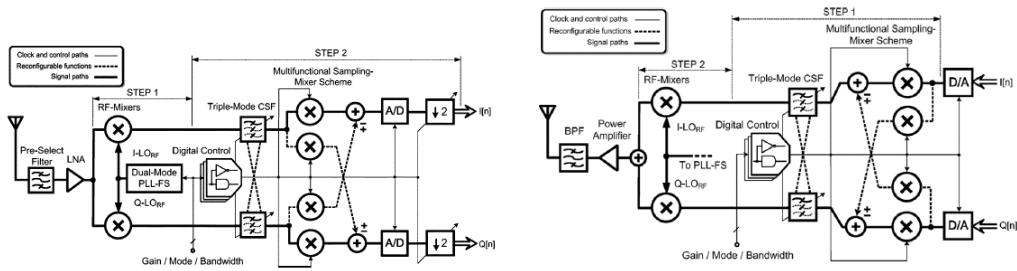


Figure 2.14: Multistandard transceiver Architecture [7]

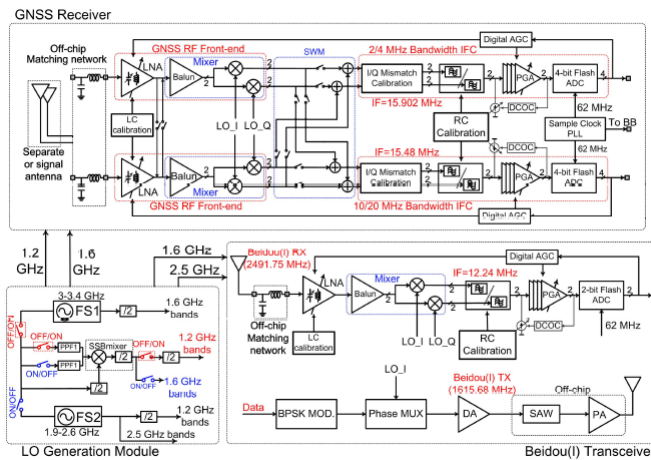


Figure 2.15: Reconfigurable transceiver Architecture [8]

proposed transceiver architecture. Even though this transceiver targets several standards; however, it has a direct conversion over a single frequency.

Another example in [8] presents a CMOS transceiver architecture that is applied over different frequency bands; however, it target only a single modulation scheme. The architecture is presented in Fig. 2.15

# Chapter 3

## An Isolation Enhanced MIMO PIFA System with Multiple Reconfiguration Techniques

### 3.1 Introduction

With the rapid development of wireless communication systems, and the rise of the age of internet of things (IoT), the requirements on communication systems is increasing significantly. In fact, RF front end systems will be responsible for the communication needs of more than 75 billion devices in 2025 as reported in [11]. Therefore, designers and researchers are seeking compact antenna systems that cater for the pressing wireless communication needs, while at the same time preserve their radiation characteristics. With the addition of needed antennas, a higher caliber of isolation will be required between the various elements. On the other hand, reconfigurable antenna systems present a solution that mitigates strong signal interference and can cope with the changing environmental conditions. Reducing the size of these antennas and their integration as part of dynamic MIMO systems can present a very well needed solution. Reconfiguring the antenna operation allows the antenna to dynamically alter its topology on demand to satisfy users needs. In reality, reconfiguration of an antenna is achieved by changing the antennas current distribution or its radiating edges. Such change results in a reconfiguration in the operating frequency, radiation pattern, or polarization scheme. Electrical switches, mechanical actuators and other techniques can be considered to achieve such redistribution [2, 19–21, 23, 47–50].

Electrical switches are the most popular components that can be incorporated on antenna structures to achieve reconfiguration [2, 19–21, 47–50]. Examples of electrical switches are PIN diodes [20, 47–49], varactors [50], or RF-MEMS [21]. Integrating a reconfigurable antenna within a MIMO system, contributes by an added agility to the MIMO system in addition to the improved functionality. In

reality, a MIMO system implementation increases the capacity of the channel and reduces the multipath effects [39]. A major challenge to MIMO antenna systems is ensuring a high level of isolation between the various radiating elements. Such isolation is instrumental in a communication system that relies on a multitude of antenna components to satisfy the needs of a rich communication environment. Several MIMO antenna designs are investigated and presented in literature [39] where various techniques are proposed to improve the isolation between the different antenna elements. One of the techniques used in [39] is the incorporation of two stubs and one slot in the partial ground plane. Varying the distance of separation between the MIMO elements is also used as a technique for isolation improvement. In addition, orthogonal or out of plane positioning of the antenna elements contribute to the improvement of isolation levels [39].

Hence, the work presented in this chapter introduces a new reconfigurable two-element MIMO system with an enhanced isolation. The antenna elements composing the MIMO system are based on PIFA topologies. The PIFA elements are first reconfigured by relying on PIN diodes, RF MEMS, or varactors in order to cover all the needed frequencies of operation over mobile and compact terminals. Enhancing the isolation between the antenna elements is achieved by simultaneously reconfiguring a ground-integrated-band-reject filter between the PIFA components. The reconfiguration of this new compact dynamic band-reject filter enhances isolation between the elements further beyond a static multiband reject filter [51]. Such reconfiguration exhibits the advantage of providing a dynamic isolation that is far more improved and depends on the users communication needs.

This chapter tackles the analysis of the various reconfiguration techniques' effects on the PIFA radiation characteristics. More specifically, the impact of PIN diodes, RF-MEMS, and varactors on the gain, power dissipated, radiation efficiency, linearity and biasing requirements are evaluated and compared. Such analysis allows antenna designers to always commit to an informed decision on the reconfiguring components choice. Another aspect is the integration of a reconfigurable band reject filter in the ground plane of a reconfigurable MIMO PIFA. The band reject filter is reconfigured by relying on the same reconfiguration technique implemented within the radiating elements. Thus, for every reconfiguration state of the filter, the radiating elements operate at the same frequencies of interest. The band rejection of the filter is coordinated and reconfigured at the same instance as the radiating elements. Such performance of the whole system achieves a reconfigurable isolation that in turns enhances the overall MIMO performance. Novelty can also be identified in the compact MIMO implementation where the two antenna elements are integrated in close proximity and still meet the rigid MIMO criteria. This is due to the fact that the band reject filter exhibits the same slot topology as that of the radiating elements.

Section 3.2 of this chapter discusses the reconfigurable PIFA structure that is reconfigured using either PIN diodes, RF-MEMs or varactors. Section 3.3

presents a detailed analysis and a comparative study between the different reconfigurable structures and their effects on the systems performance. Section 3.4 presents the MIMO system that includes a reconfigurable isolating band reject filter within its ground plane. In addition, Section 3.4 details the improvement in isolation between the radiating elements and the impact of the various reconfiguration techniques on the MIMO performance. Section 3.5 concludes the chapter.

## 3.2 PIFA ANTENNA DESIGN USING DIFFERENT RECONFIGURABLE COMPONENTS

### 3.2.1 PIFA Antenna Design using PIN Diode

The proposed PIFA structure is composed of a rectangular patch with dimensions of  $25 * 15mm^2$ . The patch is based on Rogers Duroid 5880 substrate with a dielectric constant of 2.2 and a thickness of 1.6 mm. The substrate is suspended away from the ground plane by 4.4 mm. The antennas ground plane plane is taken to represent the size of a typical mobile phone and is considered to have an overall dimension of  $105 * 70mm^2$  as shown in Fig.3.1. A shorting sheet of width 3.5 mm is incorporated at a distance of 2 mm from the feeding point as shown in Fig. 3.1. The patch and shorting sheet are designed such that the sum of the length and width of the patch subtracted by the shorting sheet width is equal to 34.5mm ( $\lambda/4$  at 1.8 GHz) [15].

One capacitive slot is etched from the rectangular patch that has the length of  $\lambda/2$  at 900 MHz. The slots topology has an almost rectangular spiral shape as shown in Fig. 3.1. Such topology ensures better compactness for the antennas radiating surface. Two switches (S1, S2) are mounted on the slot at strategic optimized locations to achieve the required frequency reconfiguration. The first incorporated switches in this work are SMP 1320-079LF PIN diodes [52]. The different switches states allow the variation of the slots length and hence enables the antenna to reconfigure its frequency operation. The pin diodes can be biased separately due to the etching of a DC isolation gap that is shown in Fig. 3.1. Two 110 nH L-07WR11KV4T [53] RF chokes are introduced through vias at optimized locations to connect the pin diodes to the direct current (DC) power supply. The RF chokes are chosen such that their Self Resonance Frequency is 11 GHz that is outside the operation range of the antenna design. They prevent RF leakage from the antenna towards the DC biasing circuit. The location of the RF chokes as well as the shorting pins are studied to minimize their impact and thus are connected through vias as indicated in Fig. 3.1. The integrated switches get their connections to the ground plane through the shorting sheet of the PIFA

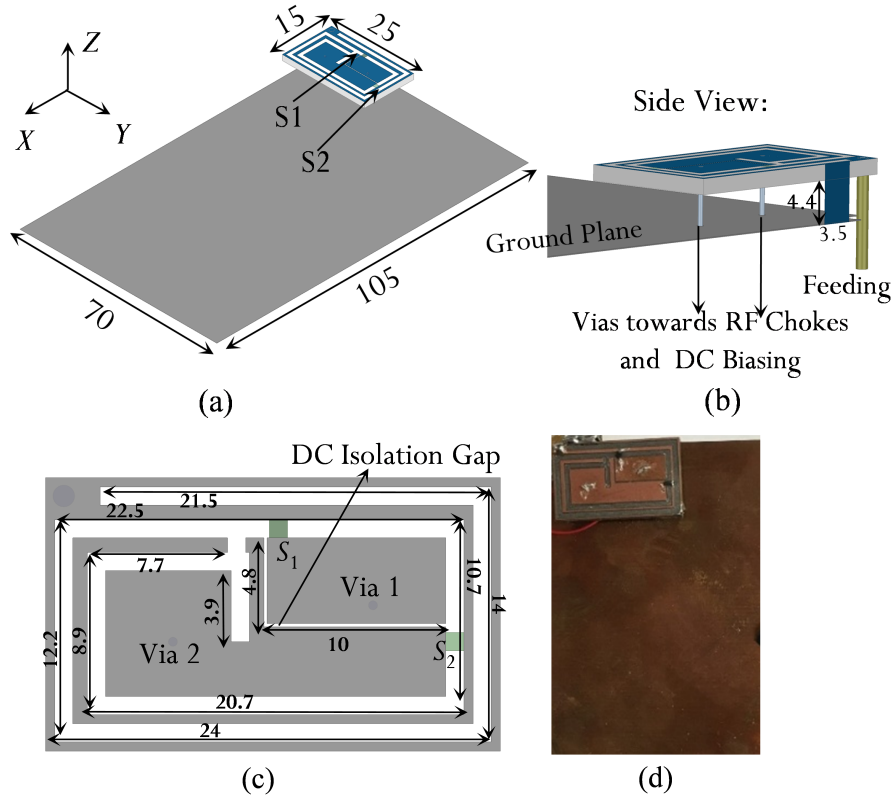


Figure 3.1: Reconfigurable PIFA structure along with its fabricated prototype (a) 3D view, (b) side view, (c) detailed dimensions, and (d) fabricated prototype

structure. The fabricated prototype of the single element reconfigurable PIFA is presented in Fig. 3.1.

Fig. 3.3 shows the comparison between the measured and simulated reflection coefficient of the reconfigurable design for different combinations of the PIN diodes states. The antenna is able to cover the following frequencies (770 MHz, 900 MHz, 1.54 GHz, 1.8 GHz, 2.1 GHz and 2.4 GHz) for different modes of operation of the two integrated switches. These frequencies allow the antenna to operate at various wireless communication applications such as LTE, GSM, GPS, 3G and Wi-Fi. Fig. 3.3 represent the comparison between the measured and simulated radiation patterns at 2.1 GHz when the PIN diode switch S1 is ON and 1.8 GHz when the PIN diode switch S2 is ON. The antennas simulated and measured maximum realized gain for various configurations and various frequencies as well as the antennas radiation efficiency along with the RF power dissipated at the various operating frequencies are presented in Table 3.2.1. The antenna operating bandwidth for each band is also summarized in Table 3.2.1.



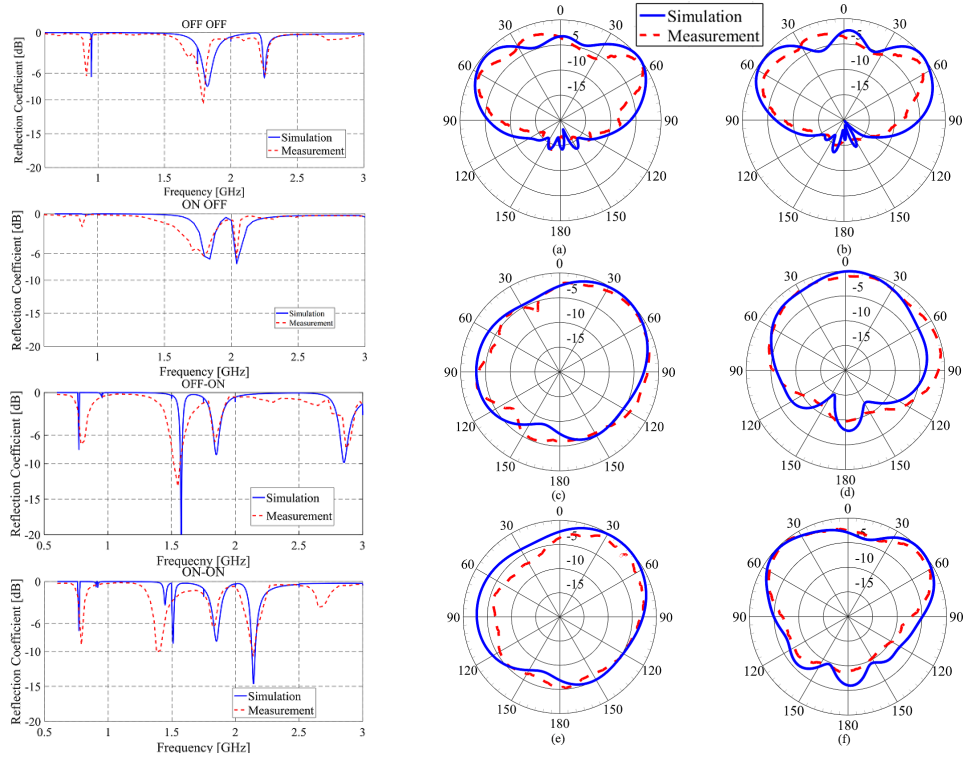


Figure 3.2: The simulated and measured reflection coefficient in dB for different switches configurations using pin diodes

Figure 3.3: The simulated and measured radiation pattern of the reconfigurable PIFA for  $\phi = 90^\circ$  at (a) 1.8 GHz when S2 is ON, (b) 2.1 GHz when S1 is ON, (c) 900 MHz when M1 is ON, (d) 1.8 GHz when M2 is ON, (e) 900 MHz when the varactor has an equivalent capacitance of 0.94pF and (f) 1.8 GHz when the varactor has an equivalent capacitance of 0.74 pF

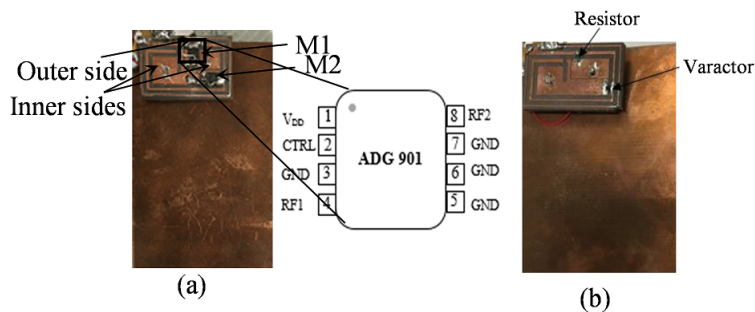


Figure 3.4: The reconfigurable PIFA structure (a) using RF-MEMS and (b) using varactor

Table 3.1: The Operating frequencies for various switches configurations along with the corresponding maximum gains, radiation efficiencies and RF power dissipated for pin diodes

Switch State	Operating Freq. (GHz)	Bandwidth (MHz)	Max. Gain (dB)		Radiation efficiency (%)		Power Dissipated (dBm)
			Simulated	Measured	Sim.	Meas.	
S1 OFF & S2 OFF	0.9	10	0.5	0.45	32	28	5.6
	1.8	50	4	3.7	15	12.5	12.6
	2.4	20	4	3.8	17	16	11.6
S1 OFF & S2 ON	0.77	10	0.5	0.5	40	38	4.3
	1.54	30	1	0.98	30	28	6.1
	1.8	40	4	3.82	14	12.5	12.7
S1 ON & S2 OFF	2.66	70	4	3.9	16	14	12.2
	1.8	40	4	3.9	12.5	12.3	12.8
	2.1	30	3.5	3.37	25	24.5	9.2
S1 ON & S1 ON	0.77	10	0.5	0.5	38	37.5	8.9
	1.54	30	1	0.98	28	27	6.1
	1.8	40	4	3.9	11	10	17
	2.1	30	3.5	3.37	22	20	12

### 3.2.2 PIFA Antenna Design using RF MEMS

In order to investigate and study the effect of the reconfiguring component on the performance of the reconfigurable antenna, the same antenna structure is re-designed using RF-MEMS. The antenna is integrated into the simulation environment with RF-MEMS instead of PIN diodes, where the locations of the switches remain the same. The fabricated prototype is shown in Fig. 3.4. Two ADG901 MEMS [54] along with their respective biasing networks and a shorting sheet are integrated within the antenna to ensure a successful frequency reconfigurable operation. This switch is an eight-pin analog device. Its pin configuration is shown in Fig. 3.4. The RF supply pin 1 (RF1) and the DC supply pin (VDD) are connected to the inner side of the antenna. This side of the antenna is connected to 110 nH L-07WR11KV4T [53] through vias. Inductors are used to prevent the leakage of the RF signal back to the DC power source. The ground (GND) pins and the RF2 pin are connected to the outer side of the antenna. The CTRL pin is connected to VDD when the RF-MEMS is operating in the ON state. When the RF-MEMS is OFF, it is connected to GND.

Two RF-MEMS can guarantee four states of operation. Similar to the case of pin diodes, three states are sufficient to achieve the required bands of operation (770 MHz, 900 MHz, 1.54 GHz, 1.8 GHz, 2.1 GHz and 2.4 GHz). Fig. 4.5 shows the comparison of the reflection coefficient results between the simulation and measurement for the various states of the switches. A good agreement is observed between both sets of results. The reflection coefficients for RF-MEMS have

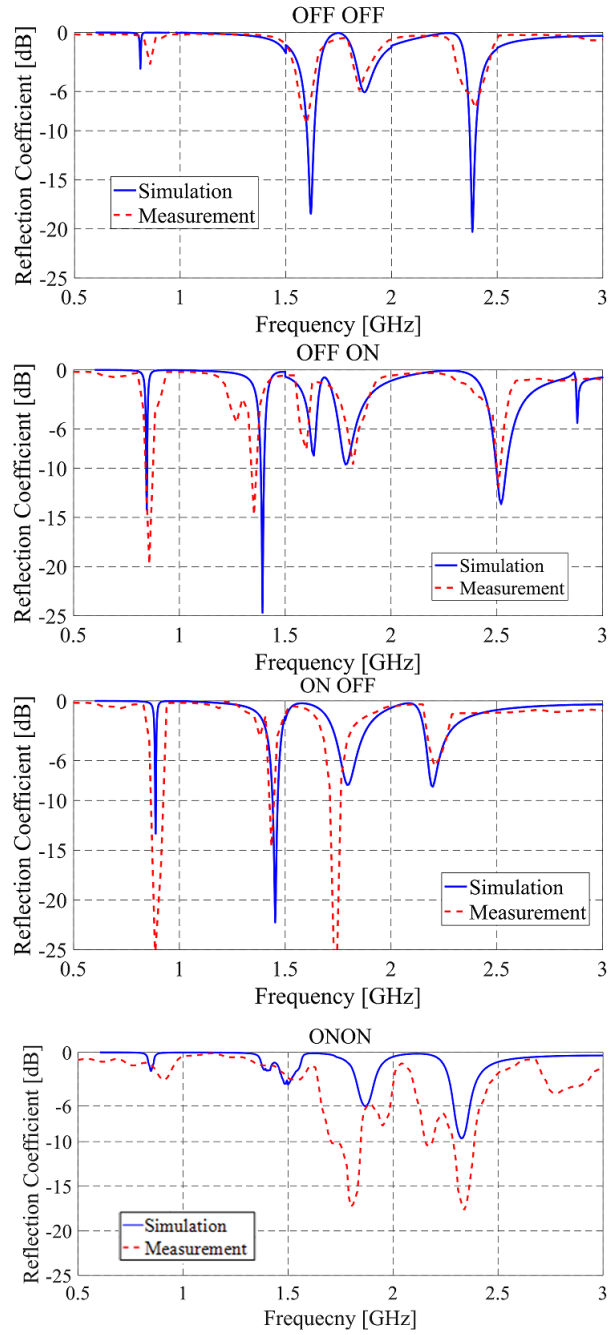


Figure 3.5: The simulated and measured reflection coefficient in dB for the different biasing of the RF MEMS

Table 3.2: Operation frequencies for various switches configurations along with corresponding maximum gains, radiation efficiencies and RF power dissipated for RF MEMS

Switch State	Operating Freq. (GHz)	Bandwidth (MHz)	Max. Gain (dB)		Radiation Efficiency (%)		Power Dissipated (dBm)
			Simulated	Measured	Sim.	Meas.	
M1 OFF & M2 OFF	1.54	20	4.5	4	95	93	4.2
	2.4	100	5.1	5	95	93	5.2
M1 OFF & M2 ON	0.77	10	0.4	0.37	61	63	2.3
	1.54	20	2.72	2.9	78	78	3.8
	1.8	40	4.6	4.3	95	93	4.5
	2.66	90	4.5	4.3	97	93	4.5
M1 ON & M2 OFF	0.9	12	0	0.2	48	50	3.1
	1.54	40	2.8	2.1	73	72	3.4
	1.8	70	4.1	4.07	88	85	4.7
	2.1	60	3.7	3.5	78	73	4.7
M1 ON & M2 ON	1.8	30	2	2	90	89	7
	2.4	70	4.29	4	83	80	7

Table 3.3: Operation frequencies for various switches configurations along with corresponding maximum gains, radiation efficiencies and RF power dissipated for varactors

Varactor capacitance	Operating Freq. (GHz)	Bandwidth (MHz)	Max. Gain (dB)		Radiation Efficiency (%)		Power Dissipated (dBm)
			Sim.	Meas.	Sim.	Meas.	
0.64	0.77	6	1.3	1.23	74	78	1.06
	1.47	40	4.4	4.3	95	93	0.3
	1.775	70	4	3.98	95	93	0.26
	2.1-2.13	40	4.54	4.5	97	95	0.16
	2.44-2.46	20	3.8	3.73	93	89	0.5
0.74	0.86	6	1.2	1.1	73	76	1.16
	1.45-1.48	30	4.3	4.2	99	93	0.26
	1.73-1.8	70	3.75	3.6	97	95	0.16
	2.08-2.11	30	4.33	4.1	97	95	0.16
	2.39-2.42	30	4	2.9	96	95	0.06
0.84	0.865	10	1.2	1.1	73	79	0.96
	1.48-1.5	20	4.1	4.1	95	95	0.16
	1.75-1.8	50	3.66	3.6	98	93	0.26
	2.07-2.09	20	4.1	4	97	95	0.16
	2.36-2.4	40	4	3	97	96	0.06
0.94	0.865	10	1.2	1.1	73	76	1.16
	1.77-1.8	30	3.7	3.68	98	91	0.36
	2.06-2.07	10	3.7	3.53	95	91	0.36
	2.33-2.38	50	4.3	4	98	91	0.36

smaller magnitudes than the ones for pin diodes configurations. This is due to the different capacitance and resistance values of the switches. The simulated and measured maximum realized gains and radiation efficiency at the various frequencies of operation are displayed in Table 2. This table also includes the operating bandwidth and RF power dissipated for various states of the two RF-MEMs. The measured gain levels range from 0.2 dB to 4.3 dB for various frequencies at different configurations. The variation is due to the different current distributions at various frequencies. It can be noticed that the radiation efficiency and the RF power dissipated in this case are better than that of pin diodes. The comparison between measured and simulated radiation patterns at 900 MHz and 1.8 GHz are shown in Fig. 3.3.

### 3.2.3 Varactor based Reconfigurable PIFA Design

Designing a reconfigurable antenna using varactors forces the designer to consider their tunable capacitance. Implementing such components on a reconfigurable PIFA instead of PIN diodes or RF-MEMS adds tuning ability to the antenna design and alters its performance. In reality, the tunable capacitance value also leads to frequency tuning and can provide reconfiguration to the antenna design. After analysis, it is found that the required reconfigurable antenna functionality can be achieved with only one varactor and one resistor. Hence, the number of switching components can be reduced, which impacts the biasing requirements as well. The antenna structure shown in Fig. 3.4 relies on the SMV1247-079LF varactor [55]. Its capacitance changes from 8.86 pF to 0.64 pF with a varying input voltage. This variable capacitance enables frequency tuning and allows the antenna to cover the required bands. A comparison between the simulated and measured reflection coefficients is shown in Fig. 3.6. Table 3 represents the bandwidths covered upon tuning the capacitance values of the varactor. Also, Table 3 presents the measured and simulated peak gain values of the PIFA for the different operating frequencies. The gain ranges between 1.1 dB and 4.5 dB. Good performance is observed for the various states of the varactor. In addition, Table 3 shows the radiation efficiency and RF power dissipated in the antenna design for various varactor capacitances. It is noticed that by relying on a varactor, the antenna tunes its operational bandwidths and thus covers all the required uplink/downlink channels for the desired applications. This performance advantage lacks from the case of integrated PIN diodes and RF MEMS. In addition, the radiation efficiency of the antenna and the RF power dissipated in this case is better than that of pin diodes and RF MEMS. The radiation patterns at 900 MHz when the varactor has an equivalent capacitance of 0.94 pF and 1.8 GHz when the varactor has an equivalent capacitance of 0.74 pF are presented in Fig. 3.3 where good agreement is achieved between the simulation and measurement.

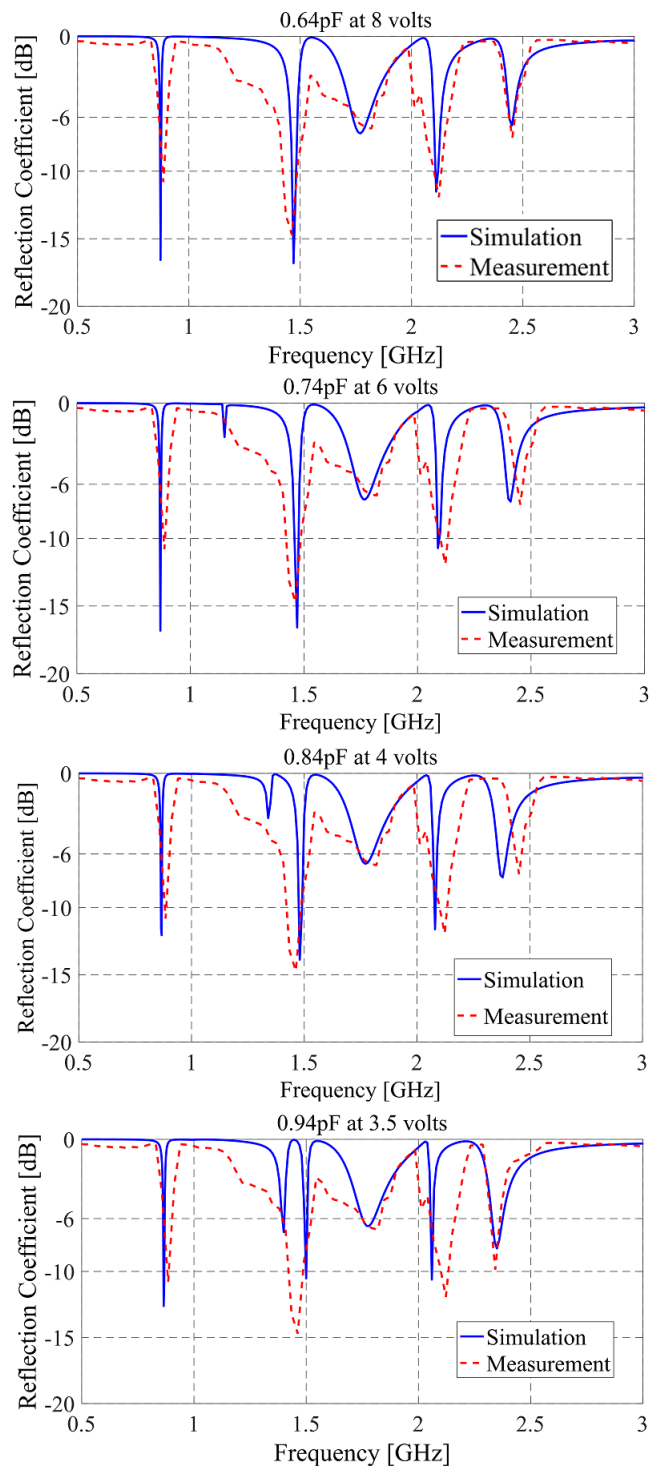


Figure 3.6: The simulated and measured reflection coefficient in dB for different biasing voltage of the varactor

### 3.3 Impact of Switches' Integration on The Design and Characteristics of the Reconfigurable PIFA

The choice of the reconfiguring component to be integrated within the antenna structure impacts the performance of the antenna and its radiation characteristics. It also impacts the design process of the antenna itself as discussed in the previous sections. In this section, the effects of the various integrated switches onto the design and performance of the presented reconfigurable PIFA is detailed.

#### 3.3.1 Number of switches

In this PIFA design, two PIN diodes and two RF MEMS are needed to achieve the desired operation at the needed wireless communication applications. However, only one varactor is sufficient to reach the desired frequencies.

#### 3.3.2 Biasing

The three types of switches analyzed in this chapter require analog input power for biasing. For the PIN diode to operate in the ON state, it requires a voltage of 1 volt with a 10-mA current resulting in 10 mWatt DC input power. The used RF-MEMS require 2.2 volts with 78 mA current and thus 171 mWatt DC input power. However, in the case of varactors the voltage needed reaches 8 V and thus 250 mW dissipated power. Therefore, the reconfiguring component requiring less DC input power is the PIN diode, followed by RF-MEMS, then varactors.

#### 3.3.3 RF Power Dissipated

The RF power dissipated represents the ohmic losses due to switches and other ohmic factors such as dielectric losses. This power is defined as the difference between the power radiated divided by the gain and the power accepted as shown in Eq. 3.1. The accepted power is the difference between the incident power and the reflected one as shown in Eq. 3.2.

$$P_d = (P_r/G) - P_a \quad Eq.3.1$$

$$P_a = (1 - |S_{11}|^2)P_i \quad Eq.3.2$$

The RF power dissipated is calculated for different switches at various configurations. Since, the dielectric losses are constant for all frequencies, the variation in the power dissipated is due to the capacitance and resistance variation in the switches. In the case of a pin diode, the power dissipated ranges between 4.3 dBm and 12.8 dBm. For the RF-MEMS, the power dissipated values vary between 2.3 dBm and 7 dBm. In the case of varactors, the power varies between 0.06 dBm

and 1.16 dBm. Since the power dissipated represents the ohmic losses, the switch that exhibits the lowest power consumption is the varactor in this case.

### 3.3.4 Radiation Efficiency

The radiation efficiency of an antenna is related to how much power can an antenna radiate with respect to a certain accepted power as shown in Eq. 3.3 [45]. In order to have fair comparison between different switches and over various frequencies, the radiation efficiency is recalculated in order to eliminate the effect of the reflection coefficient on the radiation efficiency. This is accomplished by considering a constant accepted power for the various operational frequencies. Power accepted is defined to be the input power considering the power reflected. The radiation efficiency of the antenna is measured for different switches as shown in Table 4. It is apparent that the PIN diode reconfigured PIFA displays a lower efficiency in comparison to RF MEMS and varactors reconfigured PIFAs. The radiation efficiencies when the PIN diode is integrated ranges between 44% and 18%, for RF MEMS the radiation efficiencies vary between 94% and 67%, for the varactor integrated in this antenna structure the radiation efficiencies vary between 97% and 80%.

Table 3.4: The radiation efficiency for various switches

Operating Freq. (GHz)	Radiation Efficiency (%)		
	PIN Diodes	RF MEMS	Varactors
0.87	44	67	80
1.54	32	94	95
1.8	15	94	96
2.1	28	75	96
2.4	18	94	97

$$R_e = P_r/P_a \quad Eq.3.3$$

### 3.3.5 Non-Linearity

A Pin diode is a semiconductor switch that has a nonlinear Current-Voltage curve as clearly illustrated in [56]. When such a switch is integrated into an antenna structure, this nonlinearity effect leads to low radiation efficiency and less radiated power in comparison with RF-MEMS and varactors. On the other hand, an RF-MEMS is an electromechanical switch that relies on a mechanical movement. It operates as a relay that closes when subjected to a voltage and opens when



connected to the ground. Therefore, RF-MEMS has a linear I-V performance as shown in [57] and this leads to a higher radiation efficiency, when integrated in an antenna structure. Moreover, a varactor is a semiconductor diode that relies on increasing its capacitance value by increasing the depletion region. The depletion region increases when reverse voltage is applied. The variation of the capacitance values occurs with respect to the reverse bias. Since the varactor requires reverse voltage, the current will be near zero for all voltage values. Therefore, a varactor has a linear I-V function as shown in [56] that can lead to a higher radiation efficiency when integrated in an antenna structure.

### 3.3.6 Reliability

The mechanism governing the operation of PIN diodes and varactors is based on the high-level injection of electrons. Therefore, when PIN diodes or varactors are used as switches in antennas, they offer a higher reliability, better mechanical ruggedness, and faster switching speed than electro-mechanical designs. Skyworks application notes [58, 59] proves the high reliability of pin diodes and varactors. However, a lot of studies are held in order to also address the reliability of RF MEMS [60]. The main reason behind an RF MEMS reliability concern is due to the friction effects between the metal to metal (resistive switches) or metal to insulator contacts (capacitive case) [55].

### 3.3.7 Bandwidth

Bandwidth is an important criterion to measure in an antenna design performance appraisal. As shown in Table 5, for pin diodes, the antenna is able to cover only the uplink or downlink channels of the design. For the case of RF MEMS, the antenna can cover the uplink and some of the downlink channels. However, for the case of varactors, the tunable performance allows the operation over a larger bandwidth and thus enables covering all the uplink and downlink channels for all desired applications.

## 3.4 MIMO Implementation of The Reconfigurable PIFA System

The reconfigurable PIFA design presented in section 3.3 is now proposed for integration as part of a two element MIMO system. Such MIMO implementation is instrumental in ensuring the appropriate performance needed from the communication devices in a heavily loaded and connected environment. The MIMO system will be evaluated using the three reconfiguration techniques.

Table 3.5: Bandwidth comparison between different switches

Switch State	Operating Freq. (GHz)	BW (MHz)	Switch State	Op. Freq. (GHz)	BW (MHz)	Varactor capacitance	Operating Freq. (GHz)	Bandwidth (MHz)
<b>S1 OFF &amp; S2 OFF</b>	0.9	10	<b>M1 OFF &amp; M2 OFF</b>	1.54	20	<b>0.64</b>	0.77	6
	1.8	50					1.47	40
	2.4	20		1.775	70			
	5.2	60		2.1-2.13	40			
<b>S1 OFF &amp; S2 ON</b>	0.77	10	<b>M1 OFF &amp; M2 ON</b>	2.4	100	<b>0.74</b>	2.44-2.46	20
	1.54	30					0.86	6
	1.8	40		1.45-1.48	30			
	2.66	70		1.73-1.8	70			
<b>S1 ON &amp; S2 OFF</b>	5.2	60	<b>M1 ON &amp; M2 OFF</b>	0.77	10	<b>0.84</b>	2.08-2.11	30
	1.8	40					1.54	20
	2.1	30		1.8	40			
	3.55	70		2.66	90			
<b>S1 ON &amp; S2 OFF</b>	5.2	60	<b>M1 ON &amp; M2 OFF</b>	0.9	12	<b>0.94</b>	0.865	10
	2.1	30					1.48-1.5	20
	3.55	70		1.75-1.8	50			
	5.2	60		2.07-2.09	20			
							2.36-2.4	40
							0.865	10
							1.77-1.8	30
							2.06-2.07	10
							2.33-2.38	50

### 3.4.1 MIMO System Evaluation Basics

In order to verify that a MIMO configuration is successfully implemented and can be integrated into a mobile device, certain parameters must be verified. The first parameter that must be studied is the envelope correlation coefficient. It is a measure of the dependency of the radiation patterns of the various antenna elements in a MIMO system on each other [39]. It can be represented as shown in Eq. 3.4.

$$\rho_e = \int |(F_1) \cdot (F_2^*) d\Omega|^2 / (\sqrt{\int |F_1|^2 d\Omega}) \sqrt{\int |F_2|^2 d\Omega} \quad Eq.3.4$$

In Eq. 3.4, F1 and F2 represent the radiation patterns of both antennas [39]. The MIMO system performance can be evaluated as acceptable if the envelope correlation coefficient of the antenna system is less than 0.5 at the desired operational frequencies. The second parameter that must be checked is the isolation. It evaluates the coupling that exists between the various antenna ports. For a well-designed MIMO system, the isolation must remain less than -15dB. The total active reflection coefficient is also a significant MIMO parameter that must be verified. The active reflection coefficient of the antenna elements measures the reflected power from the total incident power while taking into consideration the coupling that exists between the various antenna elements as shown in Eq. 3.5 [45].

$$\Gamma_a^t = \sqrt{(\sum_{i=1}^N |b_i|^2)} / \sqrt{(\sum_{i=1}^N |a_i|^2)} \quad Eq. 3.5$$

The various a and b represent the incident and reflected signals respectively at the various ports [39]. For an acceptable MIMO performance, the total active reflection coefficient must remain less than -10 dB at the operating frequencies for a typical antenna and less than -6dB for antennas that are proposed for mobile devices [39]. The mean effective gain (MEG) must also be verified for a complete

MIMO analysis. MEG is a statistical measure of the antenna gain in a mobile environment. It is defined by the ratio between the mean received power of the antenna and the total mean incident power when moving the antenna over a random route [39]. It can be expressed mathematically as shown in Eq. 3.6.

$$MEG = \frac{\int (XPR/(1 + XPR)G_{\theta}(\theta, \phi) * P_{\theta}(\theta, \phi) + 1/(1 + XPR)G_{\phi}(\theta, \phi)P_{\phi}(\theta, \phi))\sin\theta d\theta d\phi}{\int (XPR/(1 + XPR)G_{\theta}(\theta, \phi) * P_{\theta}(\theta, \phi) + 1/(1 + XPR)G_{\phi}(\theta, \phi)P_{\phi}(\theta, \phi))\sin\theta d\theta d\phi} \quad Eq. 3.6$$

In Eq. 3.6, XPR is the cross-polarization power ratio, and  $P_{\theta}$  and  $P_{\phi}$  are the theta and phi components of the normalized angular power density functions of the incoming plane waves [39]. These waves are presented in this work by Gaussian distribution [45] in an indoor and outdoor environment. In order to verify that a MIMO system is suitable for implementation, the ratio between the MEGs for the two antenna elements must be close to one, i.e.  $MEG1/MEG2$ .

The final parameter that will be considered for MIMO analysis is the diversity gain (DG). It represents the true benefit of the diversity scheme towards a single-antenna system. It is defined to be the difference between the signal to noise ratio (SNR) of the combined signals of all the radiators of a multi-antenna system and the SNR of the best single antenna of the structure as presented in Eq. 3.7.

$$DG = [SNR_{combined} - MAX(SNR_{barnchi})] \quad Eq.3.7$$

### 3.4.2 Design of a reconfigurable MIMO PIFA system with a multiband reject filter for isolation enhancement

The MIMO system topology is composed of two reconfigurable PIFA elements that are positioned perpendicular to each other. The reconfigurable antenna elements are separated by a distance of 29 mm as indicated in Fig. 3.7. A band reject filter is integrated between the two antenna elements within the shared ground plane. The filter is designed to serve as a compact defected ground plane structure in order to reduce the coupling between the antenna elements. The filter is composed of six nested capacitive slots that are incorporated into the ground plane of the entire antenna system. It is a  $\lambda/2$  open stub filter that can be repurposed to act as a band reject filter as discussed in [61]. The transformation of the stub into a  $\lambda/2$  slot etched from the ground plane of a radiating structure is based on Babinet's principle [61]. Such principle states that a slot etched from a copper surface acts as a copper sheet of the same dimensions placed in free space. After such transformation occurs, the slot etched from the ground plane behaves as a mean to reject undesired bands and thus, accomplishes the performance of a band reject filter for isolation enhancement in the MIMO system.

The length of each of the six nested slots is carefully taken to correspond to half wavelength at the various operating frequencies of the reconfigurable PIFA

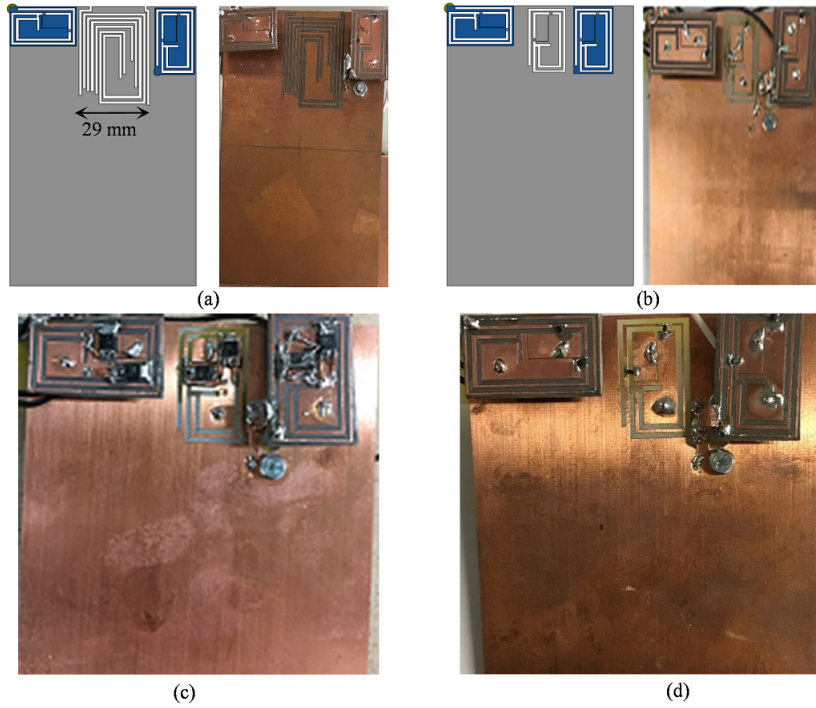


Figure 3.7: Implementation of MIMO reconfigurable antenna prototype (a) using pin diodes and multiband reject slots, (b) using varactors and reconfigurable varactor-based band reject, (c) using RF-MEMS and (d) using pin diode

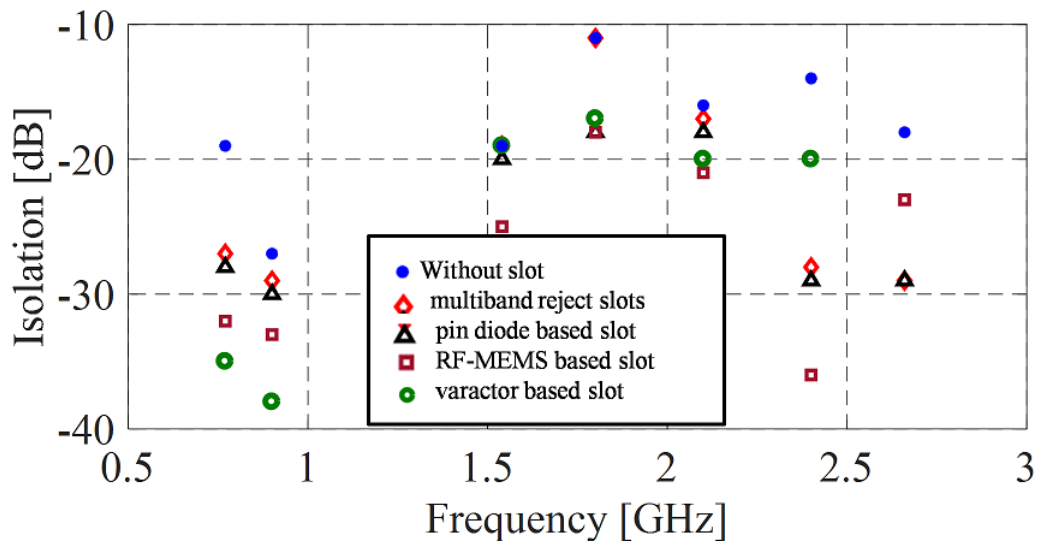


Figure 3.8: The comparison in isolation values between the various operating frequencies at the different elements configurations

discussed previously. The integration of these slots in the ground plane between the antenna elements allows them to band reject their various resonant frequencies. Thus, these slots act as a multi-band reject filter and improve the isolation levels between the two elements of the whole MIMO system. The isolation improvement at the various frequencies of operation is shown in Fig. 3.8. This graph compares the isolation between the antenna elements with and without the presence of the different nested slots. It is shown that the isolation is clearly improved at the frequencies 770 MHz, 900 MHz and 2.66 GHz while no improvement is noticed at 1.8 GHz. This lack of improvement at 1.8 GHz is an indicator that the band reject filter design must be improved in order to ensure isolation improvement at all frequencies of interest. In the next section, the reconfiguration of the band reject filter is proposed alongside the reconfigurable antenna elements to improve the isolation at all the desired frequencies of

### 3.4.3 Reconfiguration using Varactors

In this section, the nested slots filter is reconfigured in order to reject and improve the isolation in accordance with the reconfigurable antenna elements operation. The reconfigurable band reject filter is composed of three layers as shown in Fig. 3.9. The first layer is a  $50 \Omega$  transmission line of 70 mm length. The second layer is a Rogers substrate RO5880 of 1.6 mm thickness and 2.2 dielectric constant. The third layer is the ground plane where a rectangular spiral slot is etched. The spiral slot is centered below the  $50 \Omega$  transmission line. The spiral shape of the slot is intentional in order to reduce the needed landscape and achieve a more compact design. Several current paths can be achieved within the spiral slot structure as highlighted in Fig. 3.9. Each path corresponds to half wavelength at a frequency of interest in order to achieve the needed band rejection. The first path represents a  $\lambda/2$  stub at 900 MHz. The second and third paths corresponds to  $\lambda/2$  slots at 2.1 GHz and 2.4 GHz respectively. These paths can be represented by second order LC equivalent circuits as shown in Fig. 3.9. The inductance and capacitance values depend on the slot impedance and the frequency bands. The values can be calculated according to Eq. 8 and 9 [61]. Table 6 represents the inductance and capacitance values of the proposed equivalent circuit. The detailed dimensions of the slots are shown in Fig. 3.9. The overall design dimension of the filters substrate is  $70 \times 30 \text{ mm}^2$ . Fig. 3.10 shows the transmission and reflection coefficients of the proposed LC equivalent circuit along with the proposed filter design. Both data sets exhibit the same band reject frequencies at 900 MHz, 2.1 GHz and 2.4 GHz. Such results prove that the equivalent circuit model represents closely the proposed filter design operation. Reconfiguring the performance of the proposed band reject filter can be achieved by integrating a varactor and a resistor at specific locations along the slot. Their positions are chosen such that the effective length of the slot along with the equivalent effect of the varactor result in a band reject behavior at the

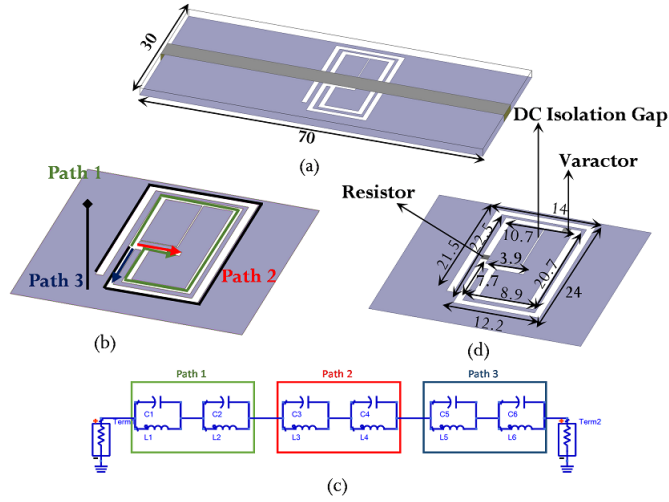


Figure 3.9: (a) The filter prototype, (b) the current paths before the addition of any active component, (c) the equivalent LC circuit model of the presented filter, (d) detailed dimensions of the various slots along with the location of the integrated varactor and resistor

desired frequency bands.

$$L = (Z_o(f_2 - f_1))/(f_1 f_2) \quad \text{Eq. 3.8}$$

$$C = 1/(4Z_o(f_2 - f_1)) \quad \text{Eq. 3.9}$$

Where  $Z_o = \text{line impedance}$ ;  $f_1 = \text{lower cutoff frequency}$ ;  $f_2 = \text{upper cutoff frequency}$ .

Table 3.6: The inductance and capacitance values for the three current paths

Inductance (nH)		Capacitance (pF)	
L1=L2	0.251	C1=C2	136
L3=L4	0.133	C3=C4	42
L5=L6	0.719	C5=C6	6.2

The reconfigurable filter topology along with the integrated varactor and resistor is shown in Fig. 3.9. By varying the biasing voltage that is supplied to the integrated varactor, a reconfigurable band rejection is achieved over different communication frequencies. These frequencies are 900 MHz, 1.54 GHz, 1.8 GHz, 2.1 GHz, and 2.4 GHz accordingly. The presented filter relies on the SMV1247-079LF varactor [55]. Its capacitance changes from 8.86 pF to 0.64 pF with a varying input voltage from 0V to 8 V. Mainly, by biasing the varactor

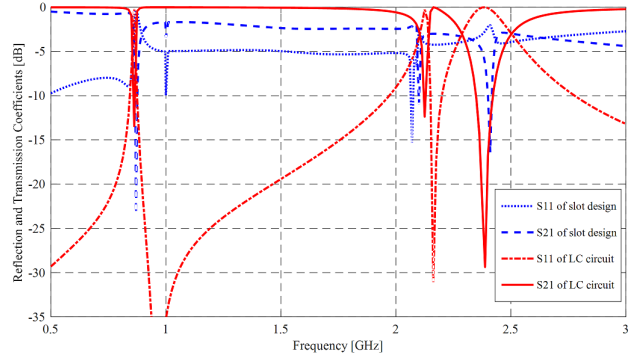


Figure 3.10: Comparison between the transmission and reflection coefficients of the proposed LC equivalent circuit and the filter 3D structure

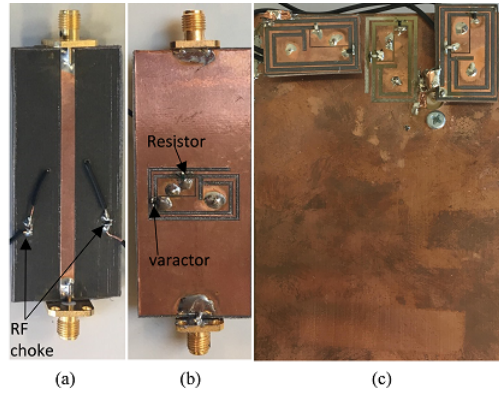


Figure 3.11: (a) The front side and (b) bottom side of the reconfigurable band reject filter structure

with different voltages, the corresponding current path changes depending on the capacitance variation. This enables the band rejection of the filter to occur at multiple desired frequencies. Similar LC equivalent circuit models can be derived for the reconfigurable filter by considering the electrical model of the integrated varactor. Fig. 3.11 shows the fabricated reconfigurable band reject filter. Two 110 nH RF choke are introduced to connect the varactor to the DC power supply as shown in the fabricated prototype in Fig. 3.11. The RF chokes prevent any RF leakage from the filter towards the DC biasing circuit through the two embedded vias. Fig. 3.11 shows the integration of the varactor and the resistor along the slots in the ground plane of the filter. The effect of varying the varactors capacitance on the transmission coefficient of the filter is shown in Fig. 3.12 for the span of frequency from 0.8 GHz - 1 GHz while Fig. 3.12 is dedicated for the 1.5 GHz - 2.5 GHz range. The filter is able to tune its band reject behavior based on the capacitance of the varactor. It is important to note that the reflection

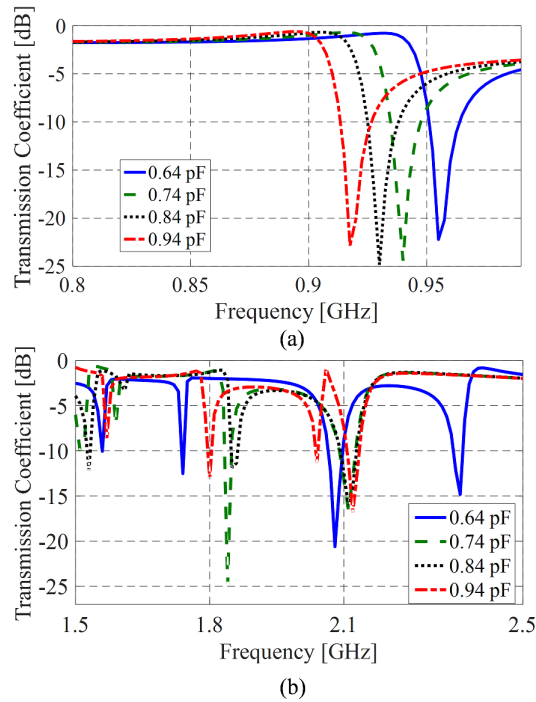


Figure 3.12: The variation of the transmission coefficient in dB for different varactor capacitance

coefficient at each corresponding band reject frequency is maintained as close as possible to 0 dB. Fig. 3.7 shows the MIMO system with the varactor integration on the band reject filter and the antenna elements. Tables 7(c) and 8(c) present the envelope correlation coefficient and the MEG calculation. The isolation improvement is represented in Fig. 3.8. As seen, the MIMO system criteria is met since the correlation coefficient is less than 0.5, the isolation is bigger than 15 dB and all the MEG ratios are around one. Fig. 3.13 shows the active reflection coefficient of the MIMO system. The diversity gain DG is found to be around 10 dB for the various varactors configurations.

### 3.4.4 MIMO Implementation using PIN diodes

The band reject filter in this case is reconfigured using two PIN diode switches as shown in Fig. 3.7, similarly to the two antenna elements. The MIMO performance evaluation in terms of envelope correlation coefficients are shown in Table 7(a). It is clear that this MIMO system meets the isolation and correlation coefficient requirements where all correlation coefficients are less than 0.5 and the isolation is maintained below -15 dB for all operational frequencies as shown in Fig. 3.8. The MEG results are presented in Table 8(a), where the MEG ratio is maintained at approximately 1 for all frequencies of interest. Fig. 3.13 represents the active



Table 3.7: The correlation coefficient for the MIMO system with (a) pin diode integration, (b) RF-MEMS and (c) varactors

Switch State	Op. Freq. (GHz)	Correlation Coefficient		Switch State	Op. Freq. (GHz)	Correlation Coefficient		Varactor cap.	Op. Freq. (GHz)	Correlation Coefficient					
		Sim.	Meas.			Sim.	Meas.			Sim.	Meas.				
S1 OFF & S2 OFF	0.9	0.1854	0.2	M1 OFF & M2 OFF	1.54	0.38	0.3	0.64	0.77	0.027	0.01				
	1.8	0.5	0.4		2.4	0.08	0.02					1.47	0.15	0.08	
	2.4	0.5	0.4	0.77	0.098	0	1.775								0.086
S1 OFF & S2 ON	0.77	0.027	0.03	M1 OFF & M2 ON	1.54	0.07			0.02	0.74	2.1	0.12	0.11		
	1.54	0.3	0.3		1.8	0.06			0					0.84	
	1.8	0.0298	0.04		2.66	0.008	0.05		0.94	2.4	0.09	0.1			
2.66	0.005	0.006	M1 ON & M2 OFF		0.9	0.0786	0.3	0.94					2.4	0.09	0.1
S1 ON & S2 OFF	1.8	0.14		0.16	1.54	0.127	0.12		0.74	2.1	0.12	0.11			
	2.1	0.009		0.01	1.8	0.007	0								
S1 ON & S2 ON	0.77	0.021	0.025	2.1	0.223	0.45	0.94		2.4	0.09	0.1				
	1.54	0.31	0.32	M1 ON & M2 ON	1.8	0.05						0.055			
	1.8	0.03	0.05		2.4	0.09	0.092		0.84	0.9	0.03	0.04			
2.1	0.009	0.01													

(a)

(b)

(c)

reflection coefficient for all switches configurations. The results indicate that the antennas in the MIMO system are fully functional at the required frequencies. Fig.3.14 shows the DG that is equal to 10 dB when only S1 is ON. The DG varies between 10 dB and 10.5 dB for other switches configurations. This highlights the benefit of the diversity scheme towards a single-antenna system.

### 3.4.5 MIMO Implementation using RF MEMS

In this part, the same MIMO system is implemented where pin diodes are replaced by RF-MEMS. Fig. 3.7 represents the RF-MEMS based MIMO system prototype. The band reject filter in the ground is now reconfigurable using two RF-MEMS. The improvement in the isolation is included in Fig. 3.8. Table 7(b) shows the envelope correlation coefficient results for different switch configurations. Similar to pin diodes, the correlation coefficient and the isolation show good results. The MEG results are presented in Table 8(b). Fig. 3.13 represents the active reflection coefficient of the different configurations. The diversity gains ranges between 10 dB and 11 dB for various switches configurations. These results validate that an RF-MEMS based reconfigurable antenna system satisfies the MIMO requirements under various conditions.

### 3.4.6 Impact of Switches on MIMO System Performance

Analyzing the performance of the MIMO system in function of the reconfiguration technique implemented reveals several factors that can push an antenna designer in one direction or the other, especially when it comes to future mobile devices in an IoT era. It is found that the proposed reconfigurable PIFA based MIMO system with varactors display lower envelope correlation coefficient and a higher isolation than that of RF-MEMS and pin diodes. In fact, such enhanced isolation

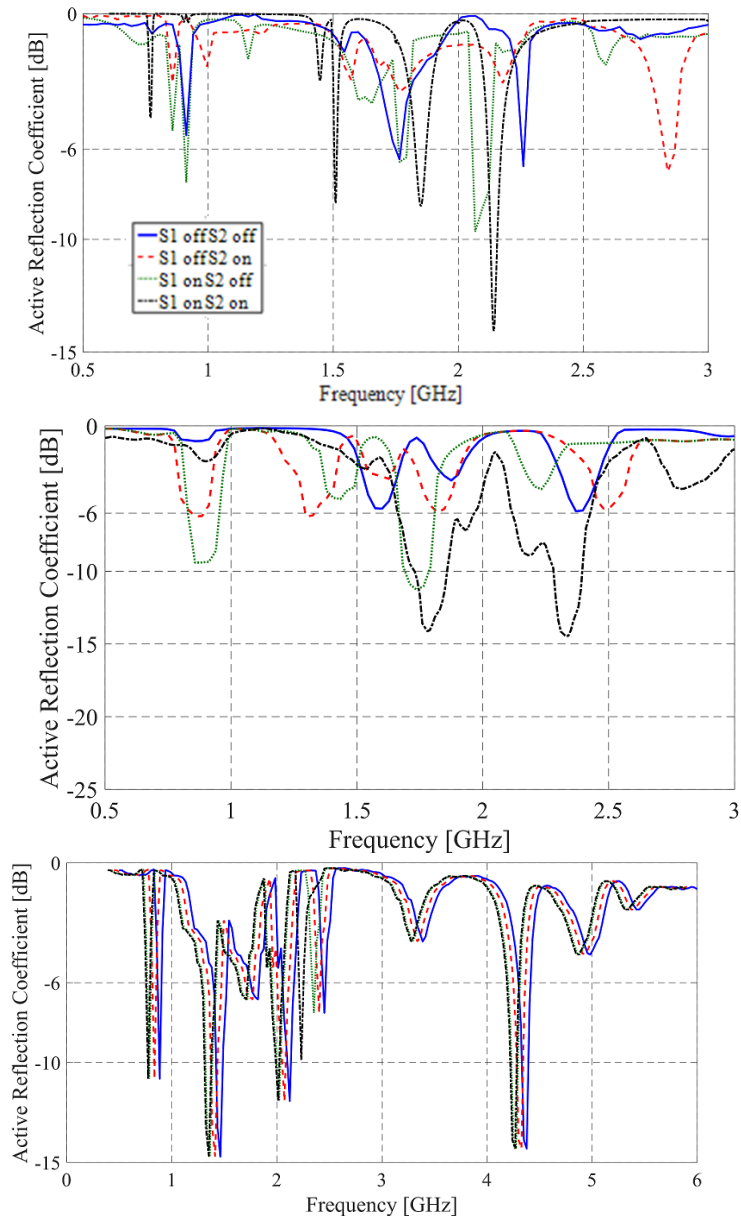


Figure 3.13: The active reflection coefficient for the various configurations of the MIMO system with (a) pin diode integration, (b) RF-MEMS integration and (c) varactor integration

Table 3.8: The MEG ratios for the two antenna elements of MIMO system with (a) the pin diode integration, (b) RF-MEMS integration and (c) varactor integration

Switch State	Op. Freq. (GHz)	Gaussian		Switch State	Op. Freq. (GHz)	Gaussian		op. Freq. (GHz)	Gaussian	
		In	Out			In	Out		Indoor	Outdoor
S1 OFF & S2 OFF	0.9	0.8	0.97	M1 OFF & M2 OFF	1.54	0.95	0.89	0.87	0.8	0.78
	1.8	0.94	0.9		2.4	0.88	0.89			
	2.4	0.92	0.86		0.77	0.9	0.85			
S1 OFF & S2 ON	0.77	0.95	0.96	M1 OFF & M2 ON	1.54	0.88	0.91	1.54	0.8	0.9
	1.8	0.86	0.87		1.8	0.82	0.96			
	2.66	0.8	0.8		2.66	0.86	0.8			
	1.8	0.85	0.91		0.9	0.91	0.97			
S1 ON & S2 OFF	2.1	0.95	0.95	M1 ON & M2 OFF	1.54	0.86	0.93	2.1	0.82	0.8
	0.77	0.95	0.965		1.8	0.83	0.97			
S1 ON & S2 ON	1.54	0.98	0.905	M1 ON & M2 ON	2.1	0.97	0.9	2.4	0.8	0.8
	1.8	0.86	0.87		1.8	0.83	0.95			
	2.1	0.96	0.95		2.4	0.89	0.9			
	0.77	0.95	0.965		0.9	0.91	0.97			

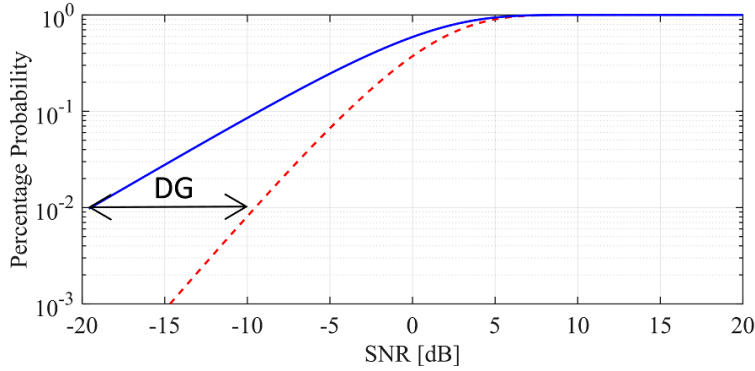


Figure 3.14: The diversity gain when S1 is ON and S2 is OFF at 2.1 GHz

performance presents the MIMO antenna system as a robust component that is suitable for integration in a system where multiple antenna components must co-exist within a limited landscape. Such scenario, realistically existing to satisfy the rising needs of communication, benefits from the reconfigurable isolation performance to enhance its operation. In addition, the choice of a reconfiguration technique to be implemented within the system can be a determining factor and impactful on the successful implementation of such a system in a practical scenario.

One must also note that the difference in the MIMO systems performance is also due to the difference in the single antenna elements characteristics. The number of switches in the varactor-based reconfigurable MIMO system is a total of three (one per antenna element and one for the isolating filter) rather than six (two for each antenna element and two for the isolating filter) as in the case of RF-MEMS and pin diodes. Table 9 summarizes the comparative analysis executed

Table 3.9: Comparative Analysis between pin diodes, MEMS and varactors

ANALYSIS	Pin diodes	MEMS	Varactors
No. of switches per antenna	two switches	two switches	one varactor
Biasing (input dc power)	low dc power requirement (10 mW)	noticeable dc power requirement (171 mW)	high dc power requirement (250 mW)
Power Dissipated (dBm)	High ohmic losses (5.3-12.8 dBm)	Moderate ohmic losses (2.3-5.2 dBm)	lowest ohmic losses (0.06-1.16 dBm)
Radiation Efficiency	low radiation efficiency (18-44%)	considerably high radiation efficiency (67-94%)	high radiation efficiency (80-99%)
Non-linearity	Non-linear	More Linear	Considerably Linear
Reliability	Reliable	Non- Reliable	Reliable
Correlation and Isolation	Acceptable	Acceptable	low

in this chapter.

It can be concluded that no switch can have an ideal no effect on the antenna performance, and hence the MIMO behavior. In other words, no switch is flawless. The switch choice is dependent on the designers constraints. Thus, the determination of the type of switch needed at the earlier stages of the design is a necessity, whose importance increases with the increase of the number of required antenna elements in a mobile communicating terminal. However, as shown in Fig. 3.8, reconfigurable isolation enhances the performance of the MIMO system itself and improves its ability to better mitigate interference.

### 3.5 Discussion

Modern wireless communications need urge antenna designers for efficient, intelligent and compact RF front ends. These systems must be integrated in portable devices while being able to cater for many operational requirements that are dynamic and continuously change on demand. Therefore, in this chapter a novel reconfigurable two element MIMO PIFA antenna system is analyzed with multiple switching components. The MIMO system operates at a multitude of frequency operation, corresponding to a desired set of communication application. In addition, the proposed MIMO system reconfigures band rejection between the radiating elements in order to enhance isolation. The impact of reconfiguring components on the systems performance and requirements is detailed. The system is analyzed, simulated and measured when PIN diodes, RF MEMS, and varactors are incorporated for reconfiguration purposes. Conclusions are drawn onto the effect and impact of switch reconfigurable MIMO PIFA systems integration in a mobile or potable device while taking into consideration various design constraints.

# Chapter 4

## Analysis of Different Switching Techniques on a Novel Filtenna Design

### 4.1 Introduction

The use of tunable bandpass filters to avoid nonlinear distortion of signals in the wanted channel is proposed in [62]. Furthermore, employing antennas with built in filtering, enhances interference rejection along the receiver chain. In [63], techniques of introducing flexible frequency discrimination, which includes tunable bandpass, tunable bandstop filters, and tunable narrowband antennas, are found to reduce spurious spectral content in the transmitter and limit out-of-band interference in the receiver. The above issues bring in frequency tuning as a good antenna attribute, not only to sense the frequency spectrum, but also to communicate.

This is due to the fact that antennas with contained tunable bandpass filtering provide autonomous control to sense/communicate, frequency tuning, suppression of unwanted interference as well as wideband noise, gain flatness, less distraction of radiation characteristics, and better processing of downconverted signals.

The proper incorporation of a well-suited tunable bandpass filter into a wideband antenna is essential to preserve its radiation performance. It is also important to mention that tuning the band pass filter requires appropriate biasing. In [64, 65], tunable bandpass filters with an asymmetrical frequency response, constant absolute bandwidth, or defected ground structures are presented. On the other hand, few tunable filtennas are reported in the literature. In [66], the authors present a varactor-based reconfigurable filtenna, whose contained bandpass filters hexagonal slot is loaded by a varactor to achieve frequency tuning. A narrowband frequency-tunable antenna for cognitive radio applications is also

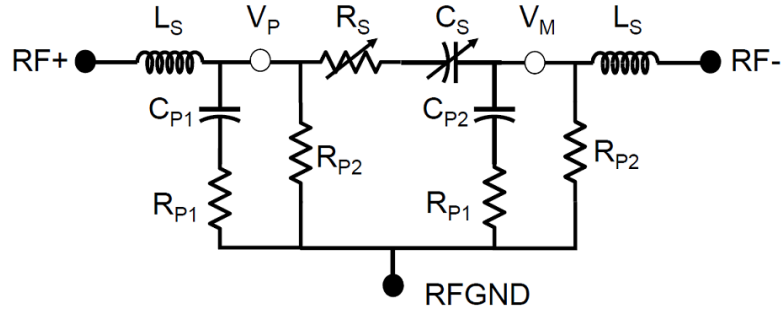


Figure 4.1: Equivalent circuit model schematic of the employed DTC [9]

proposed in [67]. This antenna incorporates a varactor tuned half wavelength open loop resonator based bandpass filter to achieve a tunable narrowband frequency operation.

In this chapter, a digitally tuned filtenna for overlay cognitive radio applications is presented. The novelty of the work presented in this chapter is based on the analysis of the various reconfiguration techniques effects on the filtenna radiation characteristics. This chapter also discusses, the impact of DTC, PIN diodes, and varactors on the gain, power dissipated, radiation efficiency, linearity and biasing requirements of the filtenna system. Such analysis allows designers to always commit to an informed decision on the choice of the reconfiguring components. Another aspect is based on transforming the wideband operation of the antenna into a tunable narrowband one. Accordingly, a reconfigurable coupled-line bandpass filter is integrated into the feeding network of a wideband antenna to achieve frequency tuning without disturbing its radiation characteristics.

## 4.2 Design Guidelines for the Coupled-Line Tunable Bandpass Filter

The tunable coupledline bandpass filter is printed on an RO3206 substrate with a thickness of 1.28 mm. The total dimensions of the filter are  $2550mm^2$ . It comprises a printed resonator between the input and output ports as shown in Fig. 4.1. The 22.5 mm physical length of the resonator approximately corresponds to an electrical length of  $180^\circ$  ( $\lambda g/2$ ) at 2.75 GHz. When the resonator is opencircuited (loading capacitance,  $CL=0$ ), a passband resonance for the filter is attained at the same frequency. The frequency tuning of the filter is achieved by loading the resonator with a pe64907 DTC [9]. DTC loaded resonators witness longer electrical lengths, and thus resonate at lower frequencies, as the loading capacitance is increased. In other words, the adjustment of the 5-bits serial input into the loading DTC will result in tuning of the resonant frequency of the bandpass filter. An STM32 microcontroller [68] is used to adjust the mounted

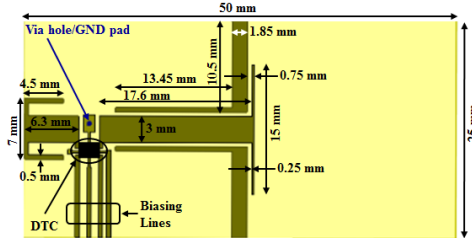


Figure 4.2: Structure of the tunable coupledline bandpass filter

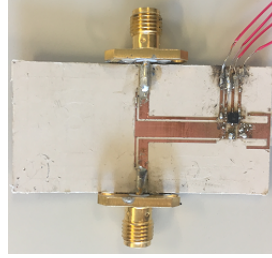


Figure 4.3: A fabricated prototype of the tunable DTC based coupledline bandpass filter

DTCs state and thus digitally tuning the operating frequency of the proposed filter. Fig. 4.1 shows the equivalent circuit model schematic of the employed DTC [9]. The crucial equivalent circuit model parameters that relate to the state values (0, 1, 231) of the DTC are given in equations (4.1) and (4.2).

$$C_s[\text{pF}] = 0.056\text{state} + 0.3 \quad (4.1)$$

$$R_s[\lambda] = 20/(\text{state} + 20/(\text{state} + 0.7)) + 0.7 \quad (4.2)$$

The tunable coupledline bandpass filter is depicted in Fig. 4.2. A PE64907 bridging DTC is put in between the GND pad and Terminal 2 of the resonator. A 47 nH RF choke is mounted between the Vcc pad and Terminal 1 of the resonator in order to avoid any RF/DC leakage, while varying the DTCs serial input bits. A fabricated prototype of the presented filter is given in Fig. 4.3. The simulated and measured S-parameters of the filter for different voltage levels are shown in Fig. 4.4 and Fig. 4.5. Good agreement between simulated and measured results is noticed.

### 4.3 DTC-Tuned Filtenna

A  $50 * 55 * 1.28\text{mm}^3$  RO3206 based wideband antenna is designed as shown in Fig. 5. It is a slot-based antenna with a slot of  $15 * 44\text{mm}^2$  in the ground plane and a 27 mm feeding line. Wideband performance is achieved by designing the feeding line length such that its electrical length corresponds to half wavelength

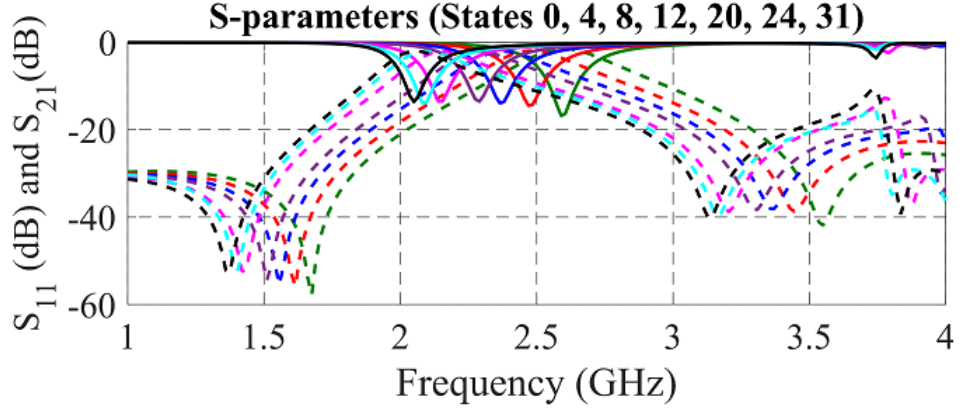


Figure 4.4: Simulated S-parameters of the tunable DTC based coupled-line band-pass filter

of the highest frequency (3 GHz) and the slot length achieves an electrical length corresponding to half wavelength of the lowest frequency (1.7 GHz) as shown in Fig. 4.6. A prototype of the designed antenna is fabricated, as illustrated in Fig. 4.7, and measured. The simulated and measured S11 plots of the antenna are shown in Fig. 4.8, where a good agreement is shown.

The DTC-based tunable coupled-line bandpass filter discussed in section 4.2 and the wideband antenna shown in Fig. 4.6 are now assembled into a single structure, as illustrated in Fig. 4.9. In order to achieve narrowband frequency tuning for the proposed filtenna, the resonator is loaded with an DTC to adjust its electrical length.

The biasing network of the DTC is simple, and does not reside on the filtenna radiating patch. It is similar to the one detailed in Section 4.2. A 15 nH RF choke is incorporated to prevent any RF leakage to the DC supply. The other terminal of the resonator is grounded through a via-hole. Accordingly, the Vcc and GND pads are used to adjust the applied bits across the mounted DTC to tune the resonant frequency of the presented filtenna as shown in Fig. 4.10. The computed reflection coefficients for each state are shown in Fig. 4.11. Despite the same frequency tuning range, the applied states values for the filtenna are different from those of the stand-alone bandpass filter because of the different impedance terminations that the filter sees when attached to the antenna. A prototype of the designed tunable filtenna, as given in Fig. 4.10, is fabricated and measured. Compared to the simulated results, Fig. 4.11 reveals a good agreement with their measured counterparts. The normalized radiation pattern of the proposed filtenna, for different states, is depicted in Fig. 4.12. The radiation pattern of the filtenna, in the XZ plane, is still omnidirectional, and minimally distracted. Moreover, the computed realized gain of the filtenna is 2.5 dB at 2.45 GHz.



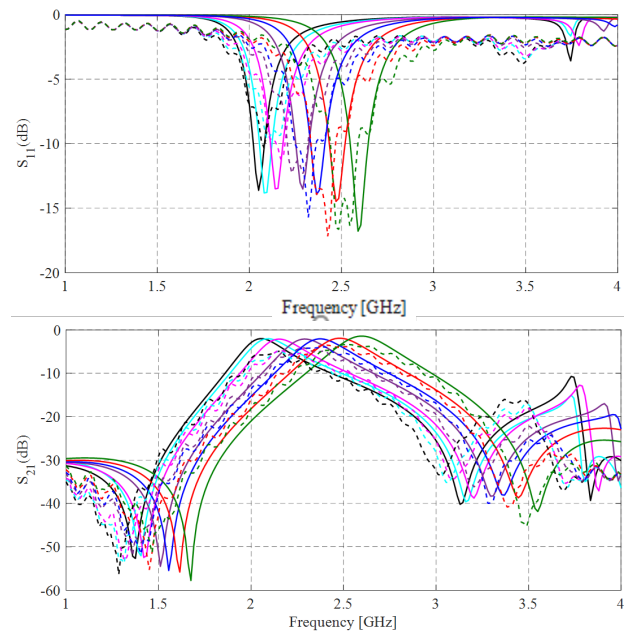


Figure 4.5: Measured and Simulated S-parameters of the tunable coupledline bandpass filter

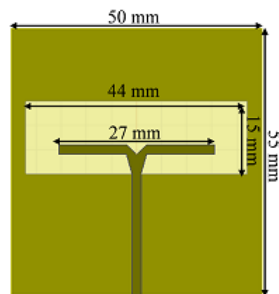


Figure 4.6: Structure of the wideband antenna



Figure 4.7: Fabricated prototype of the wideband antenna

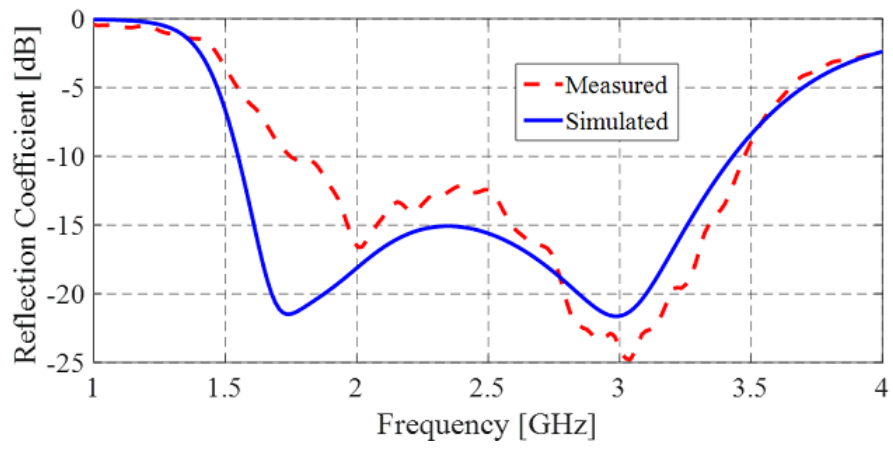


Figure 4.8: Simulated and measured reflection coefficient of the wideband antenna

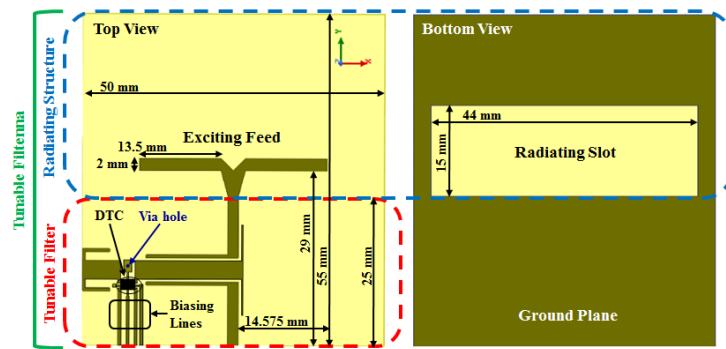


Figure 4.9: Structure of the tunable filtenna



Figure 4.10: Structure of the tunable filtenna

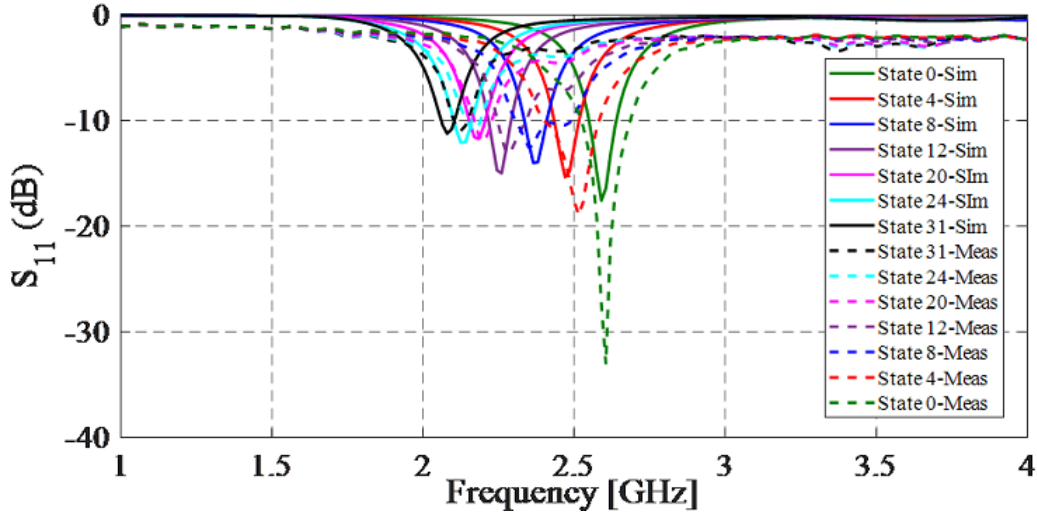


Figure 4.11: Measured reflection coefficient of the tunable filtenna

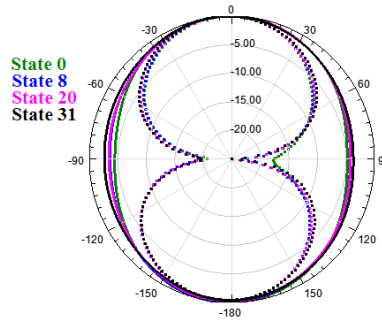


Figure 4.12: Normalized radiation pattern of the filtenna for different states

## 4.4 Filtenna Design Using Different Reconfigurable Components

### 4.4.1 Filtenna Design using PIN Diode

The same filtenna structure as that presented in Fig. 4.9 is tested by replacing the DTC by an SMP 1320-079LF [52] pin diode as shown in Fig. 4.15. Fig. 4.16 shows the comparison between the measured and simulated reflection coefficient of the reconfigurable design for different combinations of the PIN diode's states. The antenna is able to cover only two frequencies, 1.65 GHz when the pin diode is ON and 2.65 GHz when the pin diode is OFF.

Fig. 4.17 represent the comparison between the measured and simulated radiation patterns at 1.65 GHz when the PIN diode is ON and 2.56 GHz when the PIN diode is OFF. The antennas maximum realized gain for various configurations and various frequencies as well as the antennas radiation efficiency along

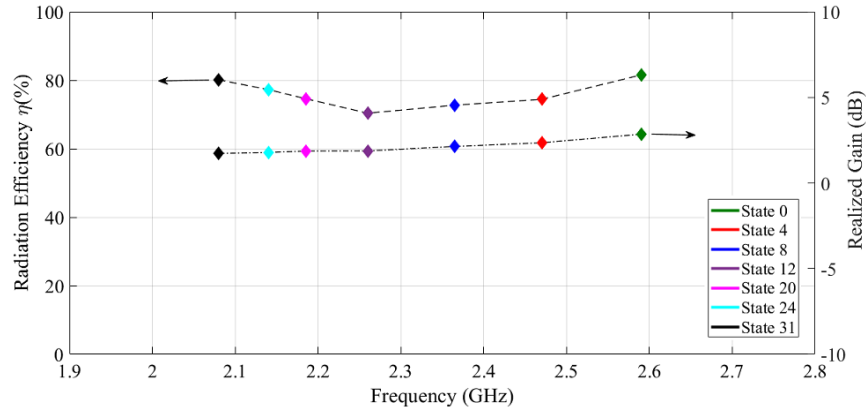


Figure 4.13: Radiation efficiency along with the gain of the filtenna for different states

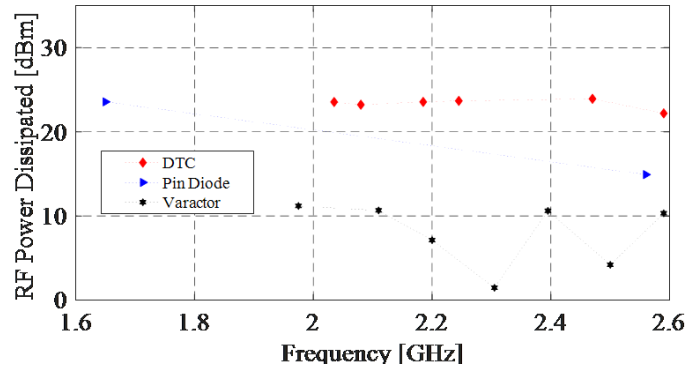


Figure 4.14: RF power dissipated for various switches over different states

with the gain at the various operating frequencies are presented in Fig. 4.18.

#### 4.4.2 Varactor based tunable filtenna design:

The filtenna is re-tested with an integrated varactor as shown in Fig. 4.15. The incorporated varactor is the SMV1247-079LF varactor [55]. Its capacitance changes from 8.86 pF to 0.64 pF with a varying input voltage. A comparison between the simulated and measured reflection coefficients is shown in Fig. 4.19. Fig. 4.18 presents the peak gain values of the Filtenna for the different operating frequencies. The gain ranges between 2 dB and 4 dB. Good performance is observed for the various states of the varactor. In addition, Fig. 4.14 and Fig. 4.18 shows the radiation efficiency and RF power dissipated in the antenna design for various varactor capacitances. In addition, the radiation efficiency of the antenna and the RF power dissipated in this case is better than that of pin diodes and DTC. The measured radiation patterns matches well with the simulated ones as presented in Fig. 4.20.

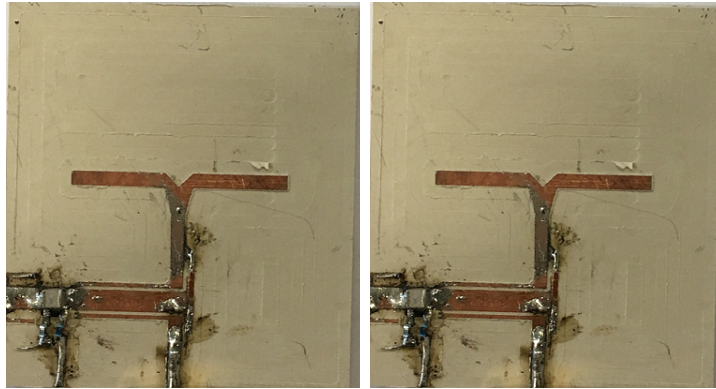


Figure 4.15: Pin diode and varactor based Filtenna

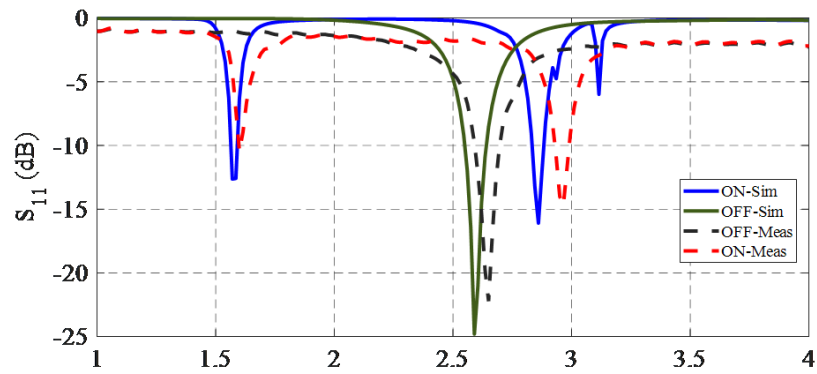


Figure 4.16: The simulated and measured reflection coefficient in dB for different switches configurations using pin diode

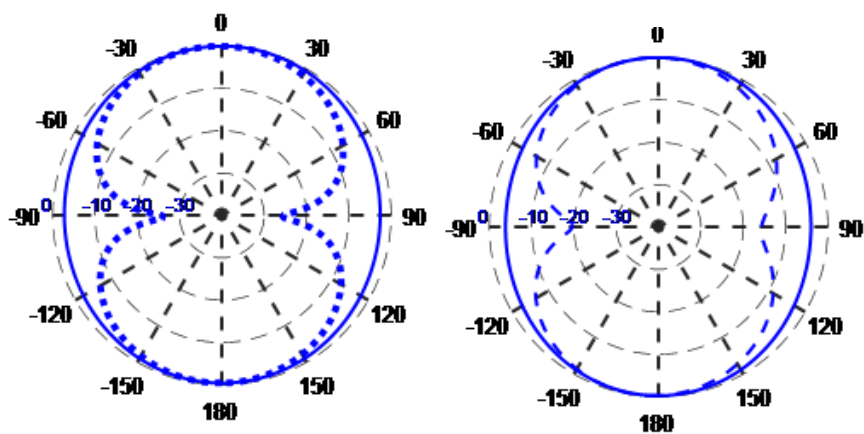


Figure 4.17: The radiation pattern of the filtenna for  $\phi = 90^\circ$  and  $\phi = 0^\circ$  at 1.65 GHz in ON state and 2.56 GHz in OFF state

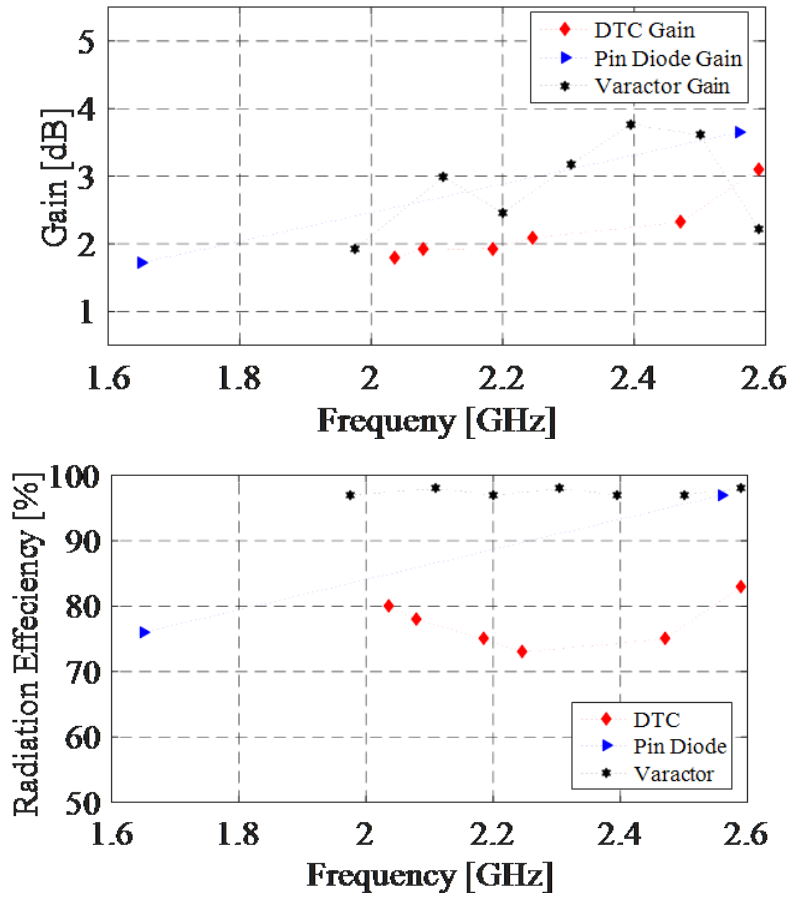


Figure 4.18: Radiation efficiency along with the gain of the filtenna for different switches techniques

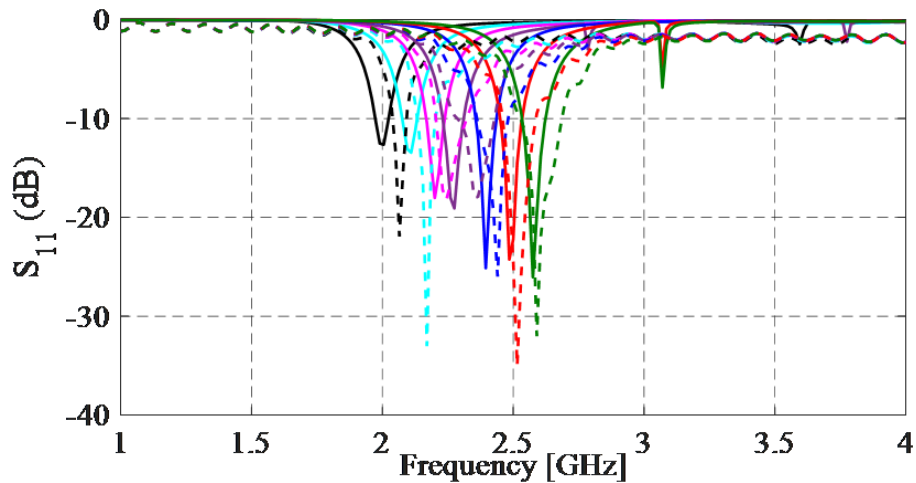


Figure 4.19: The simulated and measured reflection coefficient in dB for different switches configurations using varacator

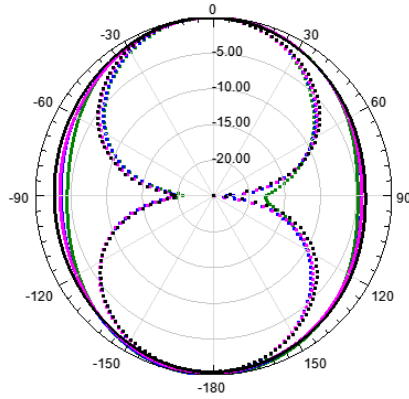


Figure 4.20: The radiation pattern of the filtenna for  $\phi = 90^\circ$  and  $\phi = 0^\circ$  for different varactor capacitance

## 4.5 Impact of Switches' Integration on the Design and Characteristics of the Filtenna

The choice of the reconfiguring component to be integrated within the antenna structure impacts the performance of the antenna and its radiation characteristics. It also impacts the design process of the antenna itself as discussed in the previous sections. In this section, the effects of the various integrated switches onto the design and performance of the presented Filtenna is detailed.

### 4.5.1 Biasing

DTC requires digital input power to achieve switching. However, Pin diodes and varactors require analog input power for biasing. For the PIN diode to operate in the ON state, it requires a voltage of 1 volt with a 10-mA current resulting in 10 mWatt DC input power. Moreover, in the case of varactors the voltage needed reaches 8 V and thus 250 mW dissipated power. However, in the DTC case, 2.75 V with 140 uA current resulting in only 0.385 mWatt DC input power. Therefore, the reconfiguring component requiring less DC input power is the DTC, followed by Pin diodes, then varactors.

### 4.5.2 RF Power Dissipated

The RF power dissipated represents the ohmic losses due to switches and other ohmic factors such as dielectric losses. This power is defined as the difference between the power radiated divided by the gain and the power accepted as shown in Eq. 4.1. The accepted power is the difference between the incident power and the reflected one as shown in Eq. 4.2.

$$P_d = (P_r/G) - P_a \quad Eq.4.1$$

$$P_a = (1 - |S_{11}|^2)P_i \quad Eq.4.2$$

The RF power dissipated is calculated for different switches at various configurations. Since, the dielectric losses are constant for all frequencies, the variation in the power dissipated is due to the capacitance and resistance variation in the switches. In the case of a pin diode, the power dissipated ranges between 15 dBm and 22 dBm. For the varactors, the power dissipated values vary between 4 dBm and 12 dBm. In the case of DTC, the power varies between 20 dBm and 22 dBm. Since the power dissipated represents the ohmic losses, the switch that exhibits the lowest power consumption is the varactor in this case. However, all switches have low RF power consumption.

### 4.5.3 Radiation Efficiency

The radiation efficiency of an antenna is related to how much power can an antenna radiate with respect to a certain accepted power as shown in Eq. 43. The radiation efficiency of the antenna is measured for different switches as shown in Fig. 4.20. It is apparent that the PIN diode reconfigurable Filtenna displays a lower efficiency in comparison to varactors or DTC's tuning. The radiation efficiencies when the PIN diode is integrated ranges between 70% and 97%, for varactors the radiation efficiencies vary between 97% and 90%, for the varactor integrated in this antenna structure the radiation efficiencies vary between 83% and 70%.

$$R_e = P_r/P_a \quad Eq.4.3$$

### 4.5.4 Non-Linearity

A Pin diode is a semiconductor switch that has a nonlinear Current-Voltage curve as clearly illustrated in [58]. When such a switch is integrated into an antenna structure, this nonlinearity effect leads to low radiation efficiency and less radiated power in comparison with varactors and DTC. Moreover, a varactor is a semiconductor diode that relies on increasing its capacitance value by increasing the depletion region. The depletion region increases when reverse voltage is applied. The variation of the capacitance values occurs with respect to the reverse bias. Since the varactor requires reverse voltage, the current will be near zero for all voltage values. Therefore, a varactor has a linear I-V function that can lead to a higher radiation efficiency when integrated in an antenna structure. On the other hand, a DTC is a digital tunable capacitor switch that relies on a linear movement. Therefore, DTC has a linear I-V performance and this leads to a higher radiation efficiency, when integrated in an antenna structure.



## 4.6 Discussion

In this chapter a novel Filtenna system is analyzed with multiple switching components. The proposed technique is based on incorporating a tunable coupledline bandpass filter in the feed line of a wideband antenna. The incorporation of the filter into the wideband antenna feeding network constitutes the proposed filtenna. Prototypes of the tunable coupledline bandpass filter, wideband antenna, and the respective filtenna are fabricated and tested. A good agreement is witnessed between the simulated and the measured results. The integration of a tunable filter into the feeding line of an antenna achieves added selectivity in addition to a distinguished tuning ability. The system is analyzed, simulated and measured when DTC, PIN diodes, and varactors are incorporated for reconfiguration purposes. Conclusions are drawn onto the effect and impact of switches on the Filtenna's performance.

# Chapter 5

## Muli-layered Folded Miniaturized Reconfigurable Antenna

### 5.1 Introduction

Portable devices require the integration of miniaturized antenna structures to ensure multi-band communication requirements, while satisfying the demanding size constraints. Hence, various miniaturization techniques must be applied in antenna designs for portable devices [6, 17, 44, 69–71]. Line meandering is a popular miniaturization method that can be applied to reduce the size of a microstrip line or patch [6]. It increases the electrical length of the line in question without increasing its physical length. For example, in [72], non-uniform meandering is applied on an antenna structure, to produce reduction in size by 45 %. The antenna is then reconfigured by relying on a PIN diode. Slits and slots are also used for miniaturization as presented in [44]. The resulting miniaturized antenna size is reduced by 37.73% by relying on slits that are added on both sides of the antenna. Another miniaturized UHF monopole antenna is proposed in [44] for IoT devices integration. The antenna relies on meandering techniques and shorting pins in order to achieve miniaturization. The design achieves a 50% size reduction in comparison to a simple monopole antenna that operates at 915 MHz.

In this chapter, we aim at exhibiting extreme miniaturization ratios. Hence we present a novel miniaturized reconfigurable loop antenna. This antenna operates over two UHF bands, 575 MHz and 760 MHz. It is a multi-layered antenna that achieves 70% size reduction at 760 MHz and 80% at 575 MHz in comparison to a typical patch antenna operating at the same frequency. The layers contain a ground plane, an impedance matching network, a meandered loop and three tapered folds. To ensure reconfiguration, an RF MEMS switch is placed between the loop and the three folds. The matching network is designed to match two distinct loads to the  $50\Omega$  coaxial feed. The first load is the input impedance of

the radiating structure when the RF MEMS is ON. Whereas, the second load is the input impedance of the antenna when the RF MEMS is OFF. The antenna dimensions are limited to  $40 \times 40 \text{ mm}^2$ , which is suitable for IoT devices with an operation at such low frequencies.

The antenna discussed in this chapter is able to operate in areas that lack traditional wireless infrastructure. This is due to the fact that the antenna operates within the white spaces of TV bands (575 MHz and 760 MHz). Second, novel miniaturization techniques are used to enable operation at 575 MHz and 760 MHz. Non-uniform zigzag meandering is applied in order to miniaturize the size of the loop while enabling its resonance at 760 MHz. The antenna structure achieves a 70% size reduction in order to fit within  $40 \times 40 \text{ mm}^2$  dimensions. In addition, three tapered folds are connected to the top layer loop patch structure, on demand, by relying on an integrated RF MEMS. These folds are tapered and folded across the three sides of the antenna to ensure compactness. As a result, the loop along with the edges folds allow the resonance at 575 MHz. Furthermore, a novel compact matching network is designed to match the two antenna impedances to the 50 ohms coaxial feed. As a result, the multi-layer structure of the antenna that includes the loop patch, folds and the matching network are assembled as one compact structure for a reconfigurable UHF communication.

## 5.2 Antenna Topology and Design

### 5.2.1 Meandered Loop Design

The initial design of the proposed antenna is composed of six layers as shown in Fig. 5.1. Layer 1 is a  $40 \times 40 \text{ mm}^2$  ground plane. Layer 2 is composed of the Rogers RO5880 substrate that is of 1.6 mm thickness and 2.2 dielectric constant. Layer 3 contains a quarter wavelength transformer. This transformer connects the 50 ohms coaxial feed to the loop antenna. Layer 4 is a 1 mm thick foam substrate that has a dielectric constant that is equal to 1.2. Layer 5 is another Rogers RO5880 substrate of 0.51 mm thickness. Layer 6 is the non-uniform zigzag meandered loop antenna.

The single loop antenna is designed such that its circumference corresponds to  $\lambda_g/2$  at 760 MHz [73]. The non-uniform zigzag shape of the antenna is used to maximize the horizontal length and achieve a compact design as shown in Fig. 5.1. The width of the line composing the loop is taken to be 2.1 mm that is translated into a characteristic impedance of 125 ohms. The  $45^\circ$  tilted meandering loop fits a longer path length in a given dimension, leading to miniaturization. The loop has four meandering turns at each side as shown in Fig. 5.1. Non-uniform meandering occurs at the fourth turn of the loop in order to increase the bandwidth of the operating frequency [72].

The quarter wavelength transformer positioned in layer 3 has an  $80\Omega$  char-

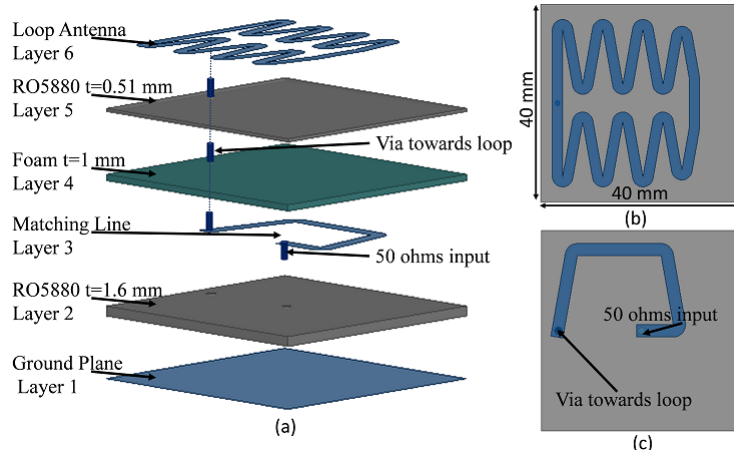


Figure 5.1: Meandered loop antenna (a) cascaded layers, (b) radiating part, and (c) transmission line

acteristic impedance and transforms the loop antenna impedance to the  $50\Omega$  of the RF coaxial input. The quarter wavelength transformer is also meandered in order to ensure further design compactness as shown in Fig. 5.1. The reflection coefficient of the antenna design displays a resonance around 760 MHz with an omnidirectional radiation pattern as shown in Fig. 5.2. At this stage, the antenna exhibits a -7dB gain at 760 MHz with a 70 % size reduction in comparison to a typical patch antenna operating at the same frequency.

## 5.2.2 Reconfigurable Antenna Performance

Achieving an antenna operation at 575 MHz requires an extension of the antenna's total length. Hence, an RF MEMS is integrated within the antenna structure as shown in Fig. 5.3. The Switch connects the main loop antenna patch to an additional section composed of two microstrip lines with a 40 mm length each. The added section surrounds the loop traces as shown in Fig. 5.3. The lines are tapered in order to enhance the bandwidth at 575 MHz, while optimizing at the same time their coupling fields to the main loop patch. The same quarter wave length transformer feeding the antenna structure is maintained to ensure good matching with a 125 ohms characteristic impedance loop as shown in Fig. 5.3. As a result of this process, a reconfiguration in the antenna operation between 760 MHz and 575 MHz is achieved. The position of the RF MEMS, which is used to connect the meandered loop to the tapered microstrip lines, is optimized in order to reach operation at 575 MHz and 760 MHz for different states of the RF MEMS. The RF MEMS acts as a capacitor of 0.12 pF in its OFF state and as a resistor of 0.5 ohms in its ON state. Therefore, when the RF MEMS is OFF the antenna operates at 760 MHz and at 575 MHz when it is ON, as shown in Fig. 5.3. When the RF MEMS is OFF, the antenna's effective electrical

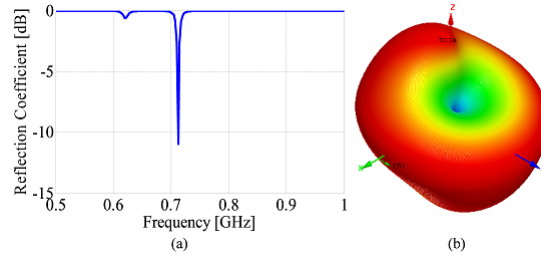


Figure 5.2: Meandered loop antenna (a) reflection Coefficient and (b) radiation pattern

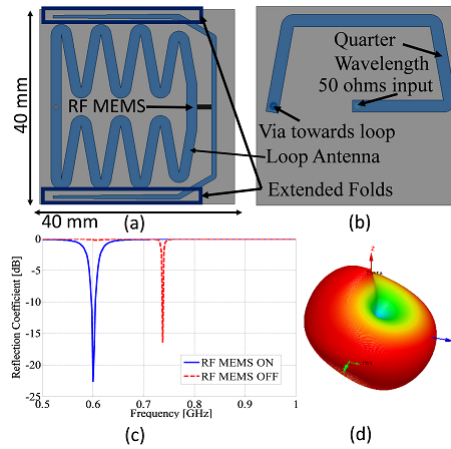


Figure 5.3: Reconfigurable loop antenna (a) loop antenna along with the extended lines, (b) matching line, (c) reflection coefficient results and (d) radiation pattern around 760 MHz

length is due to the meandered loop length, while taking into consideration the coupling with the fold lines. When the RF MEMS is ON, the antenna's electrical length is the length of the meandered loop in addition to the extended tapered microstrip lines. The coupling between the loop, matching line and the folded lines also contribute to the frequency of operation and the total effective length corresponds to half wavelength at 575 MHz. The antenna maintains its  $40 \times 40 \text{ mm}^2$  dimensions equivalent  $0.11\lambda \times 0.11\lambda \text{ mm}^2$  at 575 MHz. It leads to a 70 % size reduction at 760 MHz and 80% at 575 MHz. The addition of the extended folds with the RF MEMS in the OFF state enhances the matching at this frequency and thus adds constructively at 760 MHz. The antenna gain increases from -7 dB to -4 dB. However at 575 MHz, the close proximity between the meandered loop and the extended lines causes the deterioration in the gain results. The proximity increases the coupled fields as shown in Fig. 5.4 and hence increases the coupling. This coupling destructively affects the far field radiation. Hence, the gain is impacted due to the wave being trapped in the non-radiating near field region, which prevents it from reaching the far field region [70].

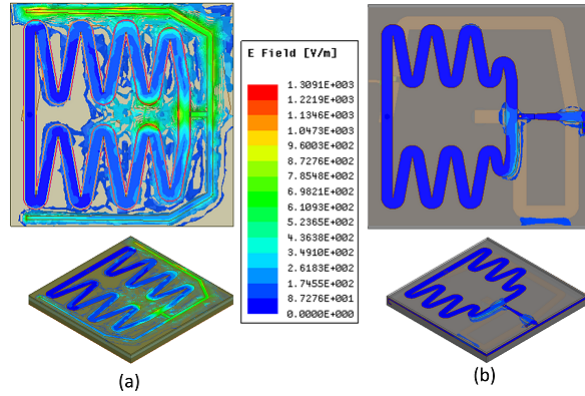


Figure 5.4: Electric Coupled Field for (a) the non-folded design and (b) the folded one

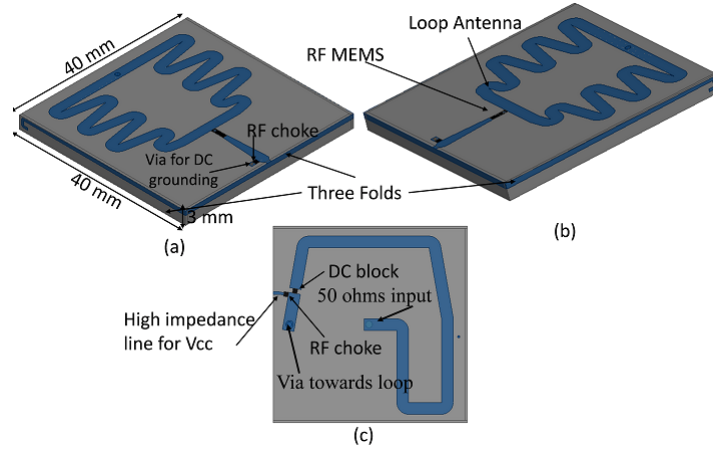


Figure 5.5: Folded loop antenna design (a) left side view, (b) right side view and (c) matching line

### 5.2.3 Folding the reconfigurable structure

In order to reduce coupling and enhance the gain of the antenna, the newly added section is folded to the three sides of the antenna structure as shown in Fig. 5.5 and (b). In this design ADG901 [54] RF MEMS is used. It is composed of 8 pins where two pins are for the input and output RF connection. These pins connect the loop to the folded radiating edges. Four pins are for grounding, one pin is for voltage supply whereas the last pin is for control (CTL). The biasing network of the switch is also integrated within the design as shown in Fig. 5.5. The matching network is optimized to include a quarter wavelength at 575 MHz as shown in Fig. 5.4. When the voltage across the control pin is zero, the RF MEMS is OFF. When the voltage across the CTL is 1.5 volts, the RF MEMS turns ON. To ensure proper biasing, three 20 nH RF Chokes are added. One RF choke connects the

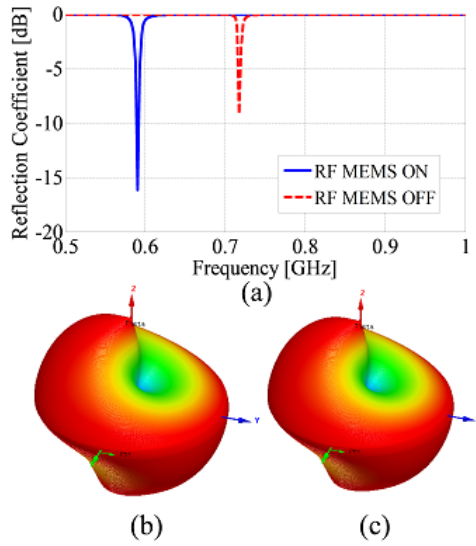


Figure 5.6: The folded loop antenna (a) reflection coefficient, (b) 3D radiation pattern at 575 MHz and (c) 3D radiation pattern around 760 MHz

CTL pin to a controlled power supply. The other RF Choke connects the voltage pin to a 2.7 V voltage supply. The last RF choke connects the ground pin to the ground plane of the antenna. RF chokes are used to eliminate RF leakage from the antenna to the DC power supplies. The respective positions of the various RF chokes are shown in Fig. 5.5. The coupling between the loop antenna and the folds is significantly less as illustrated in Fig. 5.5. It is operational at 760 MHz and 575 MHz for the various RF MEMS states as shown in Fig. 5.6. The folding technique reduces the coupling and increases the antenna gain to reach 0.2 dB at 760 MHz and -4 dB at 575 MHz. From Fig. 5.6, one notices that the obtained resonance at 760 MHz is not well matched to 50  $\Omega$ . Thus, enhancement of the matching network must occur, in order to maintain the operation at 760 MHz when the RF MEMS is off as will be detailed in the section 5.2.4.

### 5.2.4 Enhancing the Matching Network

The state of the RF MEMS impacts the input impedance of the antenna as it will enable its operation at two distinct frequencies. This effect results in the antenna behaving as two different loads respectively. However, the integrated quarter wavelength transformer cannot match different loads at different frequencies to a 50 ohms RF feed. A tuned shunt stub of the matching network can solve this problem and alleviate the mismatch. The tuned shunt stub is able to match the antenna to two different frequencies and for a variation of loads. The proposed matching network is presented in Fig. 5.7 for both antenna impedance states. When the RF MEMS is ON, the antenna input impedance is  $Z_{ON} = 60 + j60$ .

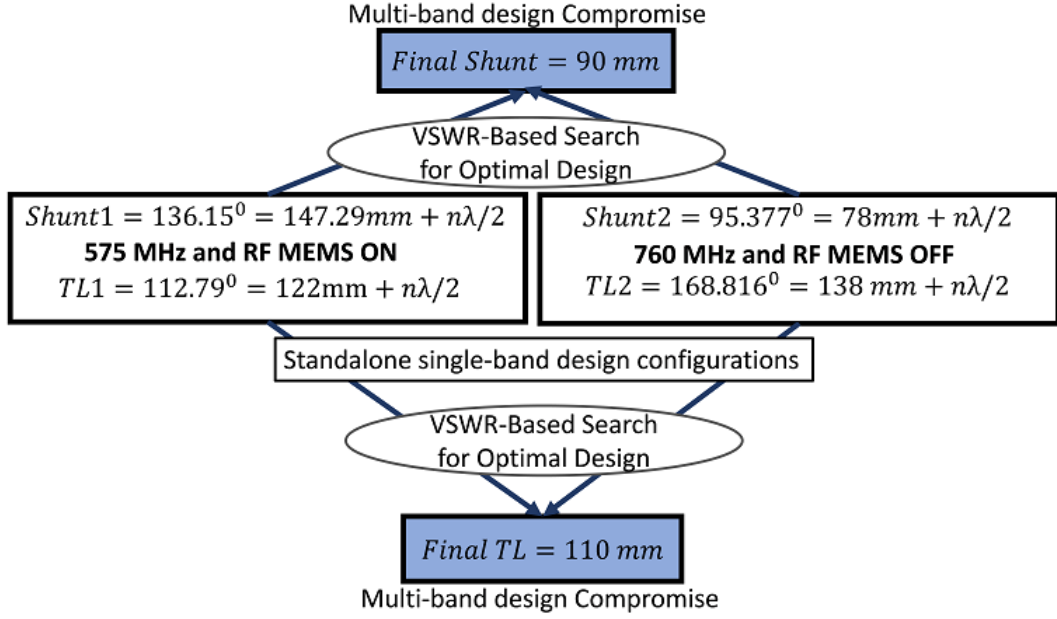


Figure 5.7: Methodology to choose the optimal L- matching network

When the RF MEMS is OFF, its input impedance is  $Z_{OFF} = 1.09 + j8.32$ . To enhance the matching, the transmission line impedance is chosen to be  $Z_O = 80ohms$  as that of the quarter wavelength transformer. The L-matching network is first designed for the two switch states separately. As shown in Fig. 5.7, for the case of RF MEMS ON and the antenna operating at 575 MHz, the matching network needs a shunt stub of 147 mm and a transmission line length of 122mm. Whereas, for the case of RF MEMS OFF and antenna operation at 760 MHz, the matching network needs a shunt sub of 78 mm and a transmission line of 138 mm. In order to reach an acceptable matching for both cases, the final TL and the final shunt stubs are chosen such that both impedances lie within the  $VSWR < 2$  circle for a  $50 \Omega$  input impedance as shown in Fig. 5.8. The final resulting matching network is optimized to match the two input impedances. As a result it is composed of a shunt stub of 90 mm and a transmission line in series of 110 mm. As proven in Fig. 8, the final TL and the final shunt stub transform both  $Z_{OFF}$  and  $Z_{ON}$  into impedances that are located inside the  $VSWR = 2$  circle of the 50 ohms input. This proves that this matching network matches both impedances to the same 50 ohms input.

The final matching network topology is presented in Fig. 5.9. The matching network is also linearly folded in a spiral shape in order to reduce its size and ensure its lodging within the  $40 \times 40 mm^2$  surface underneath the meandered loop antenna. Fig. 5.10 shows the reflection coefficient of the antenna design with the enhanced matching network. As a result, impedance matching is achieved at both frequencies and for both switch states as shown in Fig. 5.10.



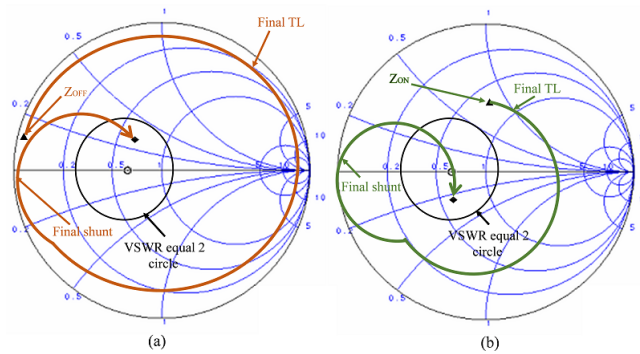


Figure 5.8: Smith chart matching of the (a)  $Z_{OFF}$  and (b)  $Z_{ON}$  with the final TL and shunt

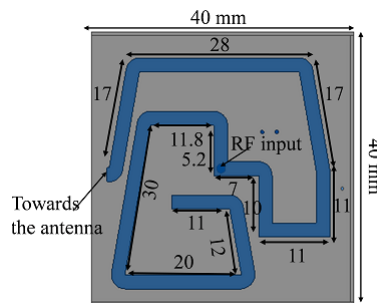


Figure 5.9: Final Matching Network

## 5.3 Reconfigurable Multi-layered Folded Antenna

### 5.3.1 Final Design

The resulting final design, shown in Fig. 5.11, is now composed of nine layers. The first layer is the  $40 \times 40 \text{ mm}^2$  ground plane. The second layer is the Rogers RO5880 substrate that is of 1.6 mm thickness and 2.2 dielectric constant. Layer 3 contains the dual band matching network discussed in Section 5.2.4. It connects the RF source to the input of the loop. The matching network is designed to enable the operation of the loop antenna at 575 MHz when the switch is ON and 868 MHz when the switch is OFF. Layer 4 is a 1 mm thick foam substrate. Layer 5 is another Rogers RO5880 substrate of 0.51 mm thickness. Layer 6 is the non-uniform zigzag meandered loop antenna. The RF MEMS switch is also placed on this layer along with its corresponding biasing network and its connection with the folded edges. Layers 7, 8 and 9 are the three folded edges that are composed of the extended tapered lines. The full dimensions of the design are limited to  $40 \times 40 \times 3.08 \text{ mm}^3$ .

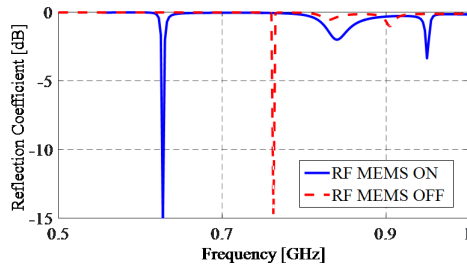


Figure 5.10: The antennas reflection coefficient in dB after adding the L-matching network

### 5.3.2 Feeding

The feeding of the antenna starts with a 50 ohms coaxial connector that is fed into the matching network at layer 3 as shown in Fig. 5.12. The supplied current flows through the matching network into a vertical metallic sheet that transfers these currents from layer 3 into the loop patch on layer 6. The metallic sheet shown in Fig. 5.11 achieves the appropriate matching between the feeding network and the top layer. It has a characteristic impedance of 80 ohms with a height of 1.51 mm, a width of 2.1 mm, and a thickness of 35  $\mu\text{m}$ . When the RF MEMS is OFF, the current flows on the zigzag loop antenna and does not enter the folded edges. Whereas for RF MEMS ON, the current flows on the loop antenna and then passes through the RF MEMS to reach all the folded edges achieving an operating frequency of 575 MHz.

### 5.3.3 Results and Measurements

The design is fabricated and assembled as presented in Fig. 5.13. The folded parts are fabricated separately and attached to the sides of the antenna. To insure continuity, conductive adhesive was soldered to the corners between each folded part. Due to its miniature size, small antenna measurements techniques are implemented in order to ensure accurate validation results [74–77]. A ferrite bead RF Choke is added to the coaxial cable in order to decrease its respective RF leakage. In addition, a balun is added between the cable and the antenna in order to electrically isolate the current paths from the antenna back to the coaxial cable. The antenna measurement setup along the vector network analyzer is shown in Fig. 5.14. Comparisons between the simulation and measured reflection coefficients for both states of the RF-MEMS are shown in Fig. 5.15. Good agreement is noticed between the measurements and simulated results. In the OFF-state, an operation at 760 MHz is obtained with a bandwidth of 3 MHz. While, in the ON state the antenna operates at 575 MHz with a bandwidth of 3 MHz. The radiation efficiency is found to be 40% at 575 MHz and 62% at 760 MHz. Such efficiencies are acceptable when designing miniaturized antennas

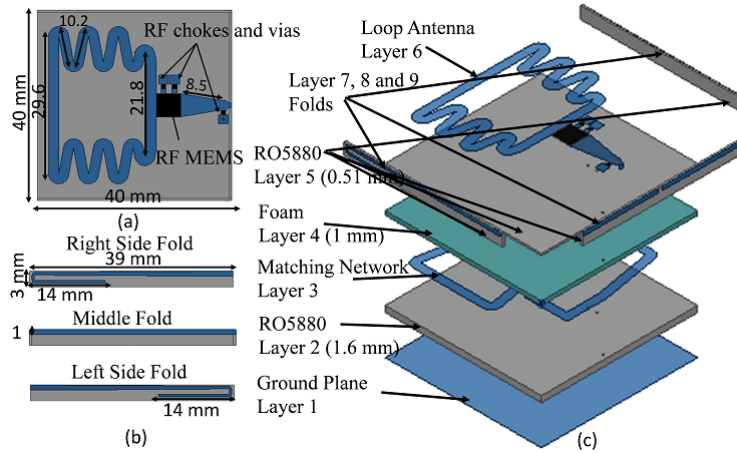


Figure 5.11: Loop Antenna Design, (a) antenna top view, (b) folds view and (c) layers composition view

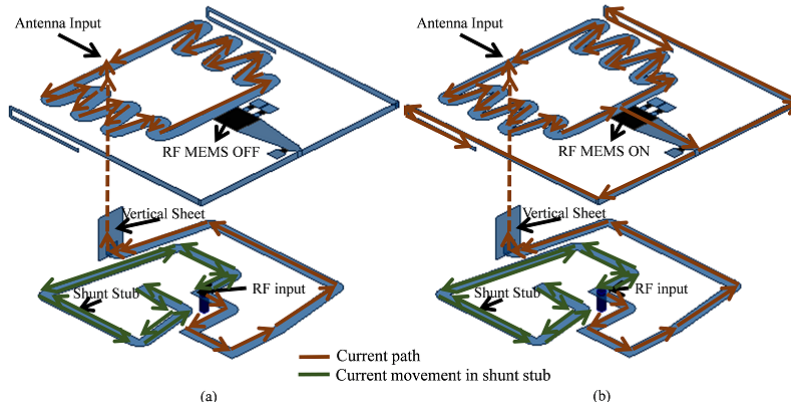


Figure 5.12: Current path for (a) RF MEMS OFF and (b) RF MEMS ON

with high size reduction percentage. The gain is enhanced to reach 1 dB at 760 MHz and -4 dB at 575 MHz. Fig. 5.16 shows simulated and measured radiation patterns of the co and cross polarization of the antenna when the RF MEMS is OFF in the x-z and y-z plane cuts. It has an omnidirectional pattern which is desired for portable applications as defined by [78].

The compactness and efficiency of the proposed antenna are finally benchmarked using the following figure of merit (FOM) which is none other than their RE per unit of electrical area (area normalized to the effective wavelength at the operating frequency of the antenna).

Its equation is shown in Eq. 5.1:

$$FOM = RE / (100 * A_{Normalized}) \quad \text{Eq. 5.1}$$

$$\text{with } A_{Normalized} = Area_{Antenna} / \lambda^2 \quad \text{and} \quad \lambda = c / ((\epsilon_r)^{0.5} f) \quad \text{Eq. 5.1}$$

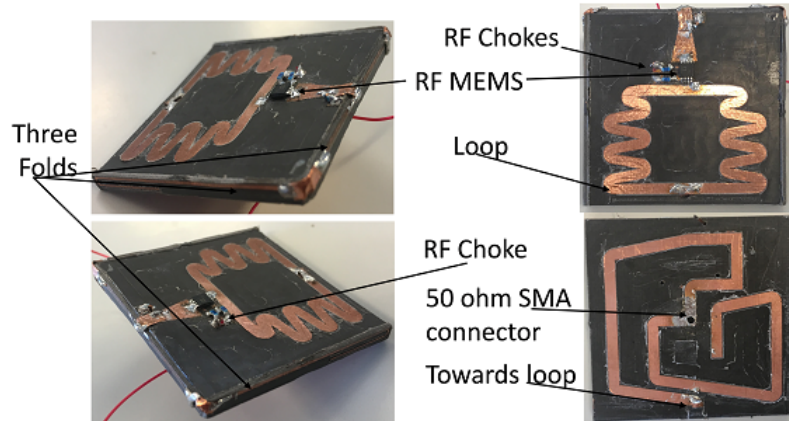


Figure 5.13: Final Prototype

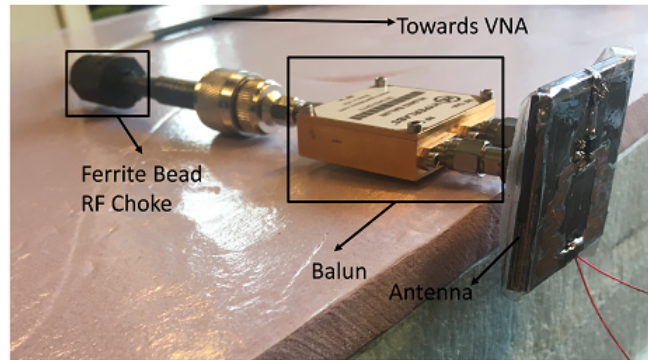


Figure 5.14: Small Antenna Measurements

Where the RE denotes the power conversion efficiency of the antenna, the  $A_{Normalized}$  takes into account the active area of the antenna normalized to the square of the largest wavelength,  $\lambda$  is the wavelength,  $c$  is the speed of light,  $\epsilon_r$  is the relative permittivity and  $f$  is the frequency of operation.

The FOM of the proposed antenna built is calculated and included in a table for comparison with several state-of-the-art work as presented in literature. Table 5.1 highlights the out performance of the proposed technique and design architecture. Such performance is highlighted by maintaining both high efficiency values despite the miniaturization aspect of the whole antenna design.

## 5.4 Discussion

In this paper, a novel compact reconfigurable loop antenna is designed. The antenna design relies on a non-uniform zigzag meandering and extreme folding in order to reduce its size. The antenna also relies on tapering and a customized

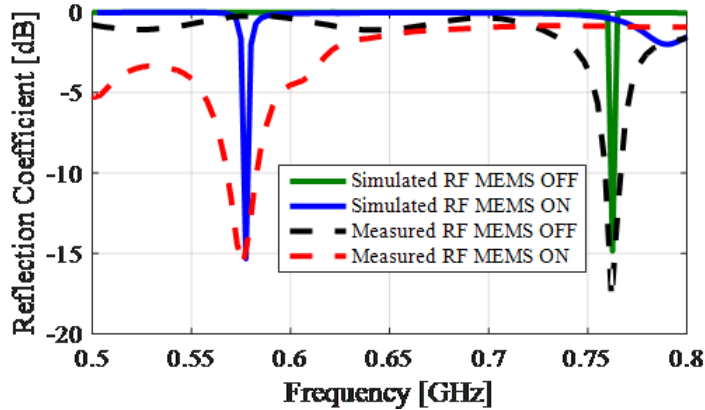


Figure 5.15: Simulated and Measured Reflection Coefficient in dB for different switch state

Table 5.1: Comparative table between the proposed design and literature

References	Antenna Dimensions in Function of largest $\lambda$	Number of Switches	Radiation Efficiency (%)	FOM
[79]	$0.26\lambda * 0.26\lambda$	24	50% at 1.2 GHz	3.69
[33]	$0.145\lambda * 0.13\lambda$	3	52% at 1.5 GHz	31
[32]	$0.15\lambda * 0.13\lambda$	2	50% at 700 MHz	30
[69]	$0.375\lambda * 0.2\lambda$	1	73% at 2.4 GHz	6.8
[40]	$0.17\lambda * 0.1\lambda$	2	65% at 3.5 GHz	5.88
[44]	$0.1\lambda * 0.1\lambda$	14	1.5% at 95 MHz	1.5
[17]	$0.18\lambda * 0.18\lambda$	0	35% at 915 MHz	10.8
Proposed Work	$0.11\lambda * 0.11\lambda$	1	62% at 760 MHz	33.05

matching network that matches the antenna across two frequency bands and for various loads. In addition, the antenna design relies on a layered volumetric structure in order to limit its size to  $40 \times 40 \times 3.08 \text{ mm}^3$ , despite its very low frequency of operation. This antenna operates at UHF for portable devices within the frequency bands of 575 MHz and 760 MHz. The antennas miniaturization aspect is determined to be 70% at 760 MHz and 80% at 575 MHz. It achieves a 40% radiation efficiency at 575 MHz as well as 62% radiation efficiency at 760 MHz. The proposed design maintains high efficiency values despite its high miniaturization aspect of the whole antenna design. The antenna is fabricated and measured where the results agree greatly with simulated ones.

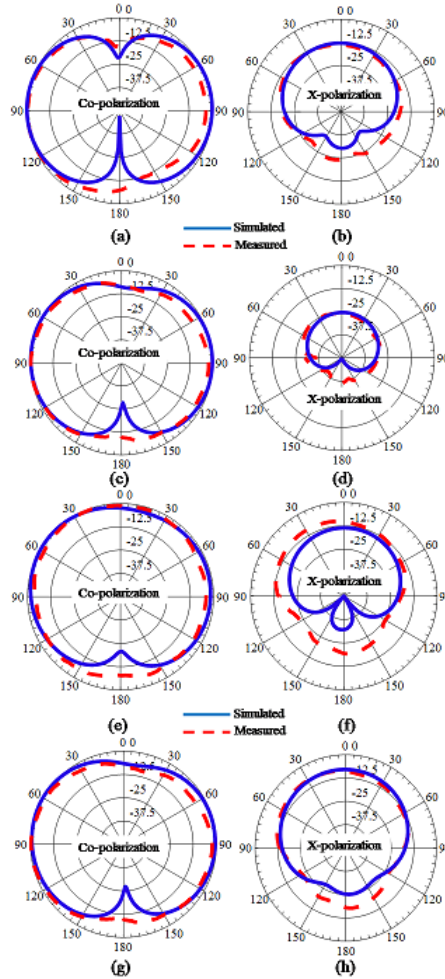


Figure 5.16: Simulated and Measured radiation patterns (a) Co-polarization at 575 MHz in the x-z plane, (b) cross-polarization at 575 MHz in the x-z plane, (d) cross-polarization at 575 MHz in the y-z plane, (c) Co-polarization at 575 MHz in the y-z plane, (e) Co-polarization at 760 MHz in the x-z plane, (f) cross-polarization at 760 MHz in the x-z plane, (g) Co-polarization at 760 MHz in the y-z plane, (h) cross-polarization at 760 MHz in the y-z plane.

# Chapter 6

## A Digitally Reconfigurable Volumetrically Folded Miniaturized Antenna

### 6.1 Introduction

IoT devices' communication should satisfy extreme sensitivity (i.e. as low as -137 dBm), along with ultra-low power consumption, bidirectional communication and localization capabilities. In addition, an IoT device must operate over several bands that target ISM, GSM and LTE. To that extent, the integration of compact frequency reconfigurable antennas allows IoT devices to achieve the required functionalities over the various frequency bands. As an example, the authors in [80] present a diversity antenna design for IoT devices with a 60% radiation efficiency at 2.45 GHz. On the other hand, in [81] a miniaturized inverted-F antenna is discussed. The designed antenna operates at 868 MHz with a radiation efficiency of 45%.

The reconfiguration in the antenna operation can be achieved using electrical switches such as pin diodes, varactors, micro electro-mechanical switches (MEMS) [82] or through the integration of digital tunable capacitors [83]. For example, in [23], a digital tunable capacitor is used on an antenna for IoT to ensure frequency reconfiguration.

The presented antenna targets the LoRa Europe and US bands (868 MHz and 915 MHz), GSM (1.8 GHz) and LTE (2.1 GHz) bands which makes it suitable for IoT devices' integration. This antenna resorts to only one DTC in order to achieve reconfiguration. In addition, it resorts to several miniaturization techniques to ensure compactness. These techniques are folds, slits and slots along the radiating element. The antenna is also able to achieve high radiation efficiencies that are above 88% with gains that vary between 0.2 dB and 3.2 dB.

In this chapter, the antenna relies on a novel folded structure that uses a sin-

gle bowtie arm and a reflective ground plane to efficiently perform at the required bands. The structure also contains several folds, slots and slits that ensure compactness. Furthermore, the antenna is able to tune its operating frequency within different bands by resorting to a single DTC. The position of the integrated DTC is optimized between the single arm bowtie and the reflective ground plane to allow proper reconfiguration. The antenna maintains an enhanced radiation efficiency (88%) with high size reduction (84%) at 868 MHz in comparison to a typical patch antenna operating at the same frequency. An additional feature of this antenna is based on its ability to exhibit different radiation patterns for different bands. For example, at the ISM band an omnidirectional pattern is obtained as required for IoT communication. As for LTE and GSM bands, the structure produces an end fire pattern which is suitable for long distance communication. These patterns ensure that the antenna is able to achieve versatile functionality over different bands as required for modern IoT devices.

## 6.2 A Volumetrically Folded Antenna Design

This antenna is proposed for portable IoT devices. Therefore, it is desired to satisfy IoT communication standards that mainly require small antenna designs that do not exceed  $50 * 50 mm^2$  while maintaining a good radiation efficiency with the ability of multi-band connections. Hence, our objective is to design a compact antenna with overall dimension that does not exceed  $50x50mm^2$ . Such antenna must be able to communicate across ISM, GSM and LTE bands on demand while maintaining an acceptable radiation efficiency. In this section, a detailed analysis of the various design steps is illustrated.

### 6.2.1 Folded Two Arms Bowties

As a first step, a typical two arms bowtie antenna is designed to operate at 868 MHz with a height of  $0.25\lambda$  and a width of  $0.375\lambda$  [84] as shown in Fig. 6.1. The corresponding antenna overall dimensions are  $110x50 mm^2$  with a peak gain of 9 dB. One arm of the bowtie is positioned on the substrate's top surface while the second arm on its bottom surface. Folding is then applied on the antenna structure as shown in Fig. 6.2 to decrease its overall dimensions while maintaining the same frequency of operation [84]. More specifically the top arm of the bowtie is folded vertically with the folded part lying on the bottom surface of the substrate. As for the bottom arm, its folded part resides on the top surface of the substrate. The connection between the folded parts and the corresponding bowtie arms is done through vertical conductive sheets along the substrate. In addition, tapered slots and slits are also added in optimized locations on the antenna surface in order to further decrease its overall dimensions [85]. The corresponding structure is presented in Fig. 6.2. The tapered slits and slots are



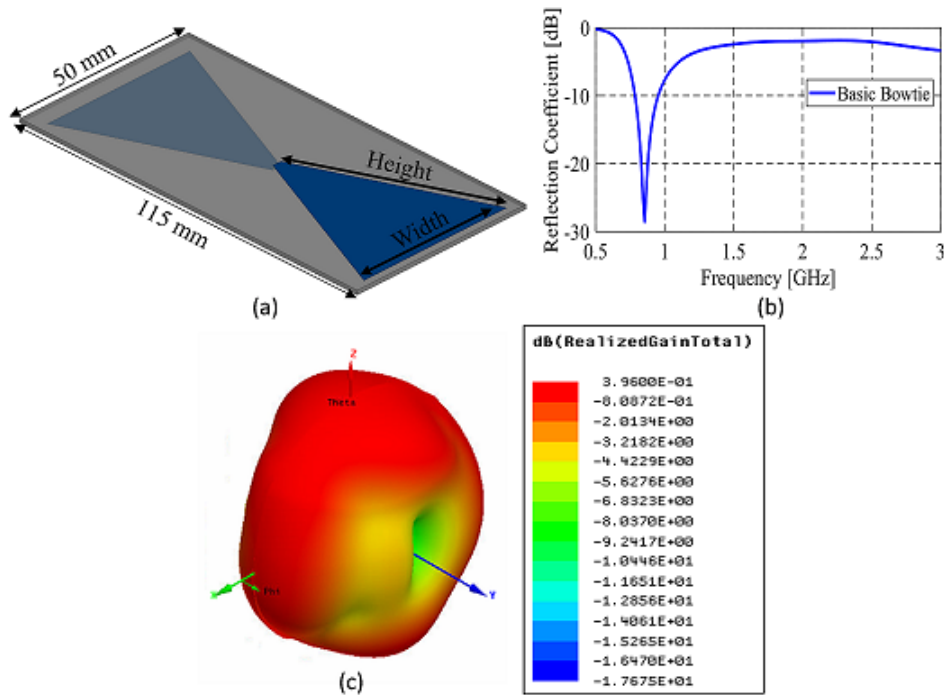


Figure 6.1: Basic bowtie antenna (a) design, (b) reflection coefficient and (c) gain plot

positioned at locations with maximum intensity of the current distribution. As a result, the size of the antenna is reduced by 18% to reach  $95 \times 50 \text{ mm}^2$ .

## 6.2.2 Semi-Bowtie Design

In order to further reduce the dimensions of the antenna while enhancing its operation, an arm of the bowtie is replaced by a reflective plane as shown in Fig.6.3. The reflector plane contributes to the bowtie arms operation and performance by additionally and constructively contributing to the antenna radiation. At the same time, it comprehensively replaces the need for a second arm of the bowtie. The reflectors dimensions ( $30 \times 50 \text{ mm}^2$ ) along with its separation from the bowtie patch enable the antenna to resonate at 868 MHz as shown in Fig. 6.3.

The location, type and topology of the excitation and antenna feeding play a major role in the antennas full operation. In this design, the feeding of the antenna is chosen as a coplanar waveguide feed. To achieve such feeding, an additional triangular reflector is added to the right side of the bowtie as shown in Fig. 6.4. The two reflectors are connected to the ground of the CPW feed while the semi-bowtie is connected to its input. The wave propagates asymmetrically between the semi-bowtie and the reflector thus leading to the operation across two

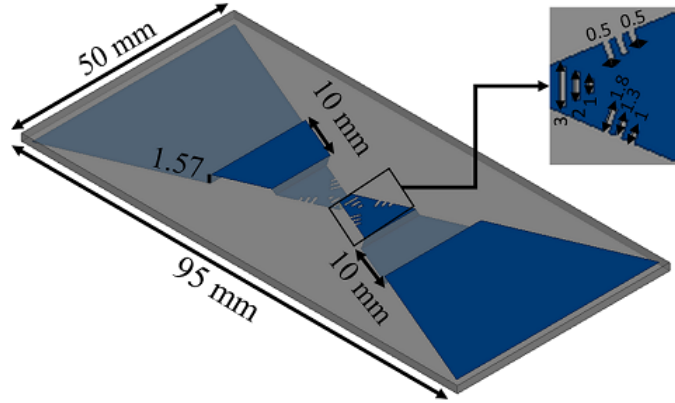


Figure 6.2: Folded two arm bowtie with slot and slit integration

frequencies as shown in Fig. 6.3. This feeding technique enhances the electric field distribution between the bowtie and reflectors and thus enhances the impedance matching at the required frequencies as shown in 6.3. As a result of all the proposed design techniques, the antenna design reaches 40% size reduction ( $50 * 70mm^2$ ) at 868 MHz with an enhanced omnidirectional pattern and a realized gain of 6 dB as shown in Fig. 6.3.

Additional size reduction can be achieved by applying 3D folding on both edges of the antenna as shown in Fig. 6.4. This folding is applied in order to achieve a  $50 * 50mm^2$  surface dimension that is considered acceptable for IoT devices.

Due to the folding of antenna edges, the antenna's input impedances gained an additional reactive effect that lead to mismatching at the targeted frequencies. The input impedance is shifted from 50 ohms to  $19+50j$  at 868 MHz and to  $88-121j$  at 2.1 GHz as shown in 6.5.

So far, the antenna has an overall dimension that is suitable for IoT devices. However, and in order to cancel out the capacitive and inductive values of the antenna's input impedance, a digitally tunable capacitor is added to the feed line of the bowtie. The DTC is added at an optimized location such that it adds capacitively at frequencies around 868 MHz and inductively at frequencies around 2.1 GHz. Furthermore, the variation of the capacitance values plays also an important role in canceling various imaginary parts of the input impedances at different frequencies thus matching the antennas at those frequencies.

For example, if this capacitor holds a 2.12 pF capacitance, then matching will be achieved at 868 MHz, thus satisfying ISM band. If this capacitor has 0.38 pF capacitance, then matching will be achieved at 2.1 GHz, hence satisfying the LTE band. Therefore, a digital tunable capacitor is required to be added to the feeding line of the antenna such that its variable capacitance and resistive values lead to frequency reconfiguration across the desired frequencies.

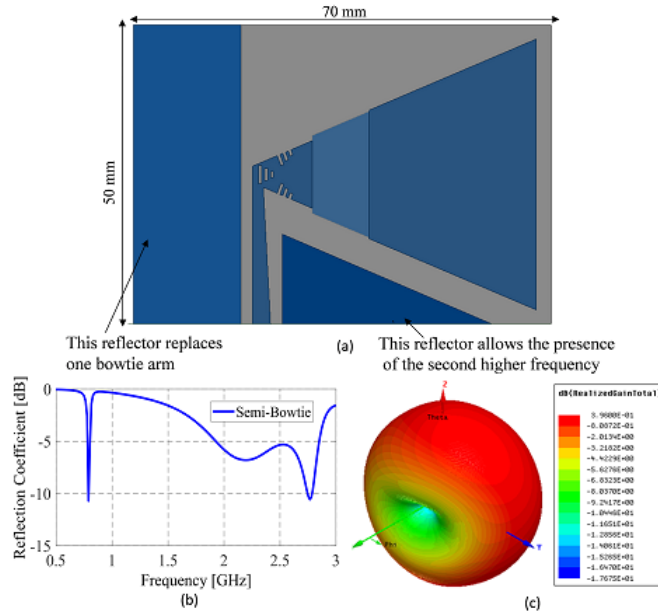


Figure 6.3: Semi bowtie antenna (a) design, (b) reflection coefficient and (c) gain pattern at 868 MHz

## 6.3 Digitally Reconfigurable Semi Bowtie Antenna

### 6.3.1 Reconfigurable Semi-Bowtie

In order to allow the antenna to operate across different communication bands while maintaining the same physical dimensions, frequency reconfiguration is required. In this design, the antenna resorts to one digital tunable capacitor.

The final antenna structure, shown in Fig. 6.6, is composed of the semi-bowtie antenna design that is based on a waveguide coplanar feeding mechanism (CPW). The antenna is of  $50 \times 50 \times 10 \text{ mm}^3$  dimensions mounted on a Rogers RO5880 substrate with a dielectric constant of 2.2 and a thickness of 1.57 mm. The first layer constitutes the folded part of the bowtie arm. The second layer is the Rogers RO5880 substrate. The third layer contains the bowtie arm, the reflected ground planes, the digital tunable capacitor and the biasing network. The final layer is the two 3D folds. The right fold contains a part of the bowtie arm. Whereas the left one contains a part of the reflective ground plane. The folds are mounted on another RO5880 substrate.

Two reflector ground planes are present in the design. The first ground plane acts as a reflector to replace the second bowtie arm. The second ground plane is a triangular shaped conductive section that acts as a reflector in order to ensure the operation of the antenna at GSM and LTE bands. Both ground planes are

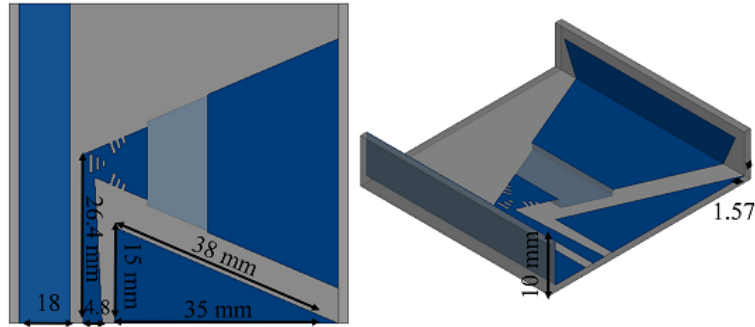


Figure 6.4: 3D folded semi-bowtie design

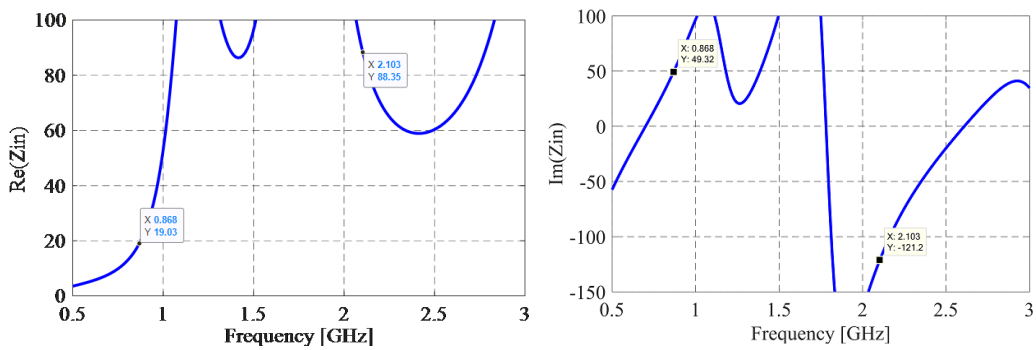


Figure 6.5: Input impedance of the antenna (a) Real and (b) Imaginary

part of the coplanar waveguide feeding. The DTC is loaded near the feed of the antenna in between the first ground plane and the bowtie as shown in Fig. 6.6. The capacitance of the DTC adds to the capacitance resulting from the separation between the bowtie and the ground plane, hence leading to a shift in the operational frequency. The variation of the capacitance and resistance of the DTC allows further tuning of the antennas operating frequency. Four high impedance lines are added between the ground plane and the bowtie radiating element to act as control lines for the DTC. These lines are of high impedance so that their effect is minimal on the performance of the antenna. At the end of each line a 110 nH RF choke is added. These chokes prevent the RF leakage back to the microcontroller. The high impedance lines also allow the passage of the serial peripheral interface (SPI) commands from the microcontroller to the DTC. The SPI three lines are the serial interface clock input, serial interface latch enable input, and the serial interface data input. When the serial interface clock input is fed by a clock of 38.4 nsec period and when the serial interface latch enable input is fed by a raising pulse, the DTC is reads the 5 bits input from the serial interface and thus changes its capacitance and resistance accordingly. The proposed antenna resorts to the capacitance and resistance variation of the DTC in order to tune and reconfigure its operating frequencies. The DTC is positioned

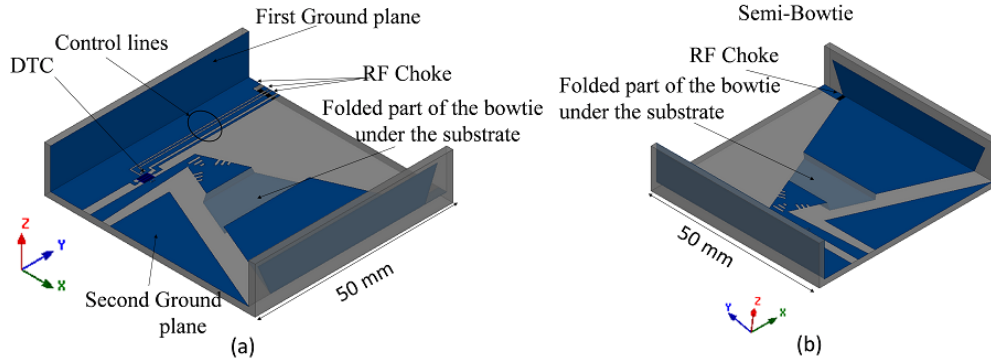


Figure 6.6: Semi Bowtie Antenna design (a) left tilted 3D view presenting the left folded side and (b) right tilted 3D view representing the right folded side

in a shunt position within the feeding CPW line, as shown in Fig. 6.6. Frequency tuning is achieved by activating the DTC component first and then varying its digital 5-bit binary input to tune its capacitance. The DTC employed in this work is the pe64907 from Peregrine Semiconductor [9]. It achieves 32 different capacitance values (or states), which can be tuned by resorting to a digital 5-bit binary ( $2^5=32$ ) digital input.

The modeling of the DTC component accounts for its constant inductive effect of 0.7 nH and its variable capacitance and resistance [23]. The different capacitance and resistance values can be calculated as described in Eq. 6.1 and Eq. 6.2 [23]:

$$C_s = 0.056state + 0.85 \quad (pF) \quad \text{Eq. 6.1}$$

$$R_s = 20 / (state + 20 / (state + 0.7)) + 0.7 \quad (\Omega) \quad \text{Eq. 6.2}$$

where state corresponds to the decimal value of the corresponding 5 bits sequence.

The activation and control of the 32 different states of the DTC can be achieved using a microcontroller. In this work, the Nucleo-RL54 is used to control the DTC operation in order to supply the corresponding 5 bits sequence for each state [9]. The initial sequence is 00000 (state 0) while the thirty-first sequence is 11111 (state 31). In state 0, the DTC has a capacitance of 0.85 pF, a resistance of 0.7  $\Omega$  and an inductance of 0.7 nH while in state 31 the DTC achieves a capacitance of 2.586 pF, a resistance of 1.33  $\Omega$  and an inductance of 0.7 nH [9]. At state 0, the capacitance of the DTC is 0.85 pF with a 0.7  $\omega$  resistance. This impedance adds up to the antennas input impedance and leads to the shift in frequency from 2.6 GHz to 2.1 GHz as shown in Fig. 6.7. As the states increase, the DTC's capacitance and its resistance increase leading to a larger shift in frequency. At state 9, the antenna shifts its frequency down to 1.8 GHz. It operates

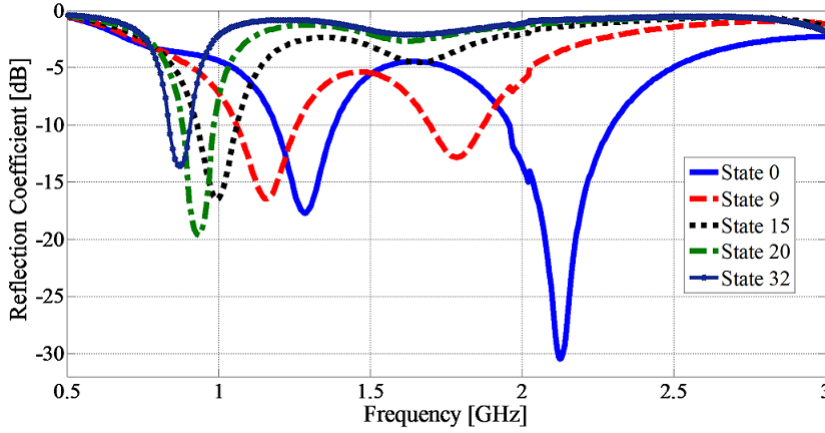


Figure 6.7: Reflection coefficient of the antenna at different states

at 915 MHz at state 20 and 868 MHz at state 31 as shown in Fig. 6.7. It is observed that the shift down in frequency is mainly due to the increase in the DTC capacitance.

### 6.3.2 Measurements and Results

The antenna prototype is fabricated and assembled as shown in Fig. 6.8. The folds are attached to the antenna by conductive adhesives. The antenna exhibits an overall size reduction that is equivalent to 84% at 868 MHz. Therefore, small antenna measurement techniques must be implemented in order to ensure accurate results [74–77]. A Ferrite bead RF Choke is cascaded with the coaxial cable in order to decrease the RF leakage. In addition, a balun is added between the cable and the antenna in order to electrically isolate the current paths from the antenna back to the coaxial cable. During the antenna measurements, the balun and the ferrite bead RF choke are connected to the vector network analyzer as shown in Fig. 6.9.

Comparison between the simulation and measured reflection coefficients for different DTC states are shown in Fig. 6.10. Good agreement is noticed between the measurement and simulated results.

The radiation patterns for the proposed design are presented in Fig. 6.11 at different frequencies for states 0, 9, 15, 20 and 31 in the  $\phi = 90^\circ$  plane cut. The antenna has a dipole shape radiation pattern at 1GHz, 915 MHz and 868 MHz as shown in 6.11. Whereas, at 1.8 GHz and 2.1 GHz, the antenna produces an almost end fire radiation pattern.

Table 6.1 presents the antenna radiation efficiency percentage and size reduction for various DTC states. The measured antennas radiation efficiency at 2.1 GHz is equal to 97% with a gain equal to 2.7 dB. This is achieved when the DTC is in state 0 and due to the fact that the length of the semi-bowtie antenna is

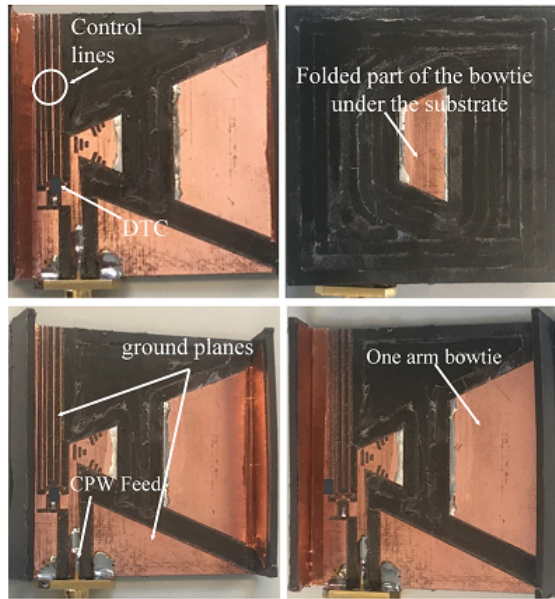


Figure 6.8: Fabricated prototype of the semi bowtie antenna design

Table 6.1: Antenna radiation efficiency and size reduction for various DTC states along with its corresponding frequency

Frequency [GHz]	State [decimals]	Size Reduction [%]	Radiation Efficiency		Gain	
			Sim.	Meas.	Sim.	Meas.
0.868	31	84	88	85	0.2	0.19
0.915	20	82	87	84	0.5	0.41
1	15	80	86	84	0.8	0.78
1.8	9	32	96	95	1.8	1.7
2.1	0	0	98	97	3.2	3.17

equivalent to half-wavelength at this frequency.

At 1.8 GHz, the antenna produces a radiation efficiency of 96%. The antenna operates at 1.8 GHz when the DTC is at state 9 and thus its capacitance value and ohmic losses are higher in comparison to state 0. In addition, the proposed antenna features a size reduction of almost 32% in comparison to a typical  $\lambda/2$  patch at 1.8 GHz with a gain equal to 1.5 dB.

In state 20, the radiation efficiency is found to be 87 % at 915 MHz with a size reduction of almost 82% in comparison to a typical dipole operating at the same frequency with a gain around 0.4 dB. In addition, at state 32, the radiation efficiency is found to be 88% at 868 MHz with a gain equal to 0.2 dB and a size reduction of 84% in comparison to a typical dipole operating at the same frequency. The decrease in the antenna size, and the high capacitance and resistance value of the DTC in states ranging between 20 and 32, impact the

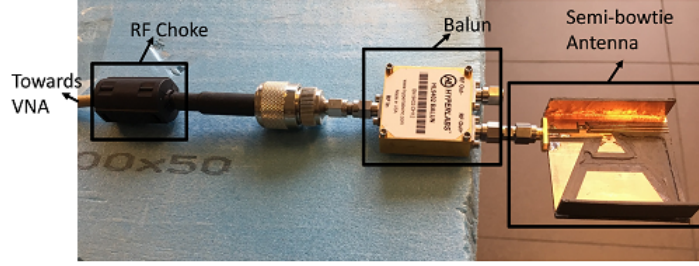


Figure 6.9: Small antenna measurements techniques for the bowtie antenna design

Table 6.2: Comparative table between the proposed design and literature

References	Antenna Dimensions in Function of largest $\lambda$	Number of Switches	Radiation Efficiency (%)	FOM
[79]	$0.26\lambda * 0.26\lambda$	24	50% at 1.2 GHz	3.69
[33]	$0.145\lambda * 0.13\lambda$	3	52% at 1.5 GHz	31
[32]	$0.15\lambda * 0.13\lambda$	2	50% at 700 MHz	30
[69]	$0.375\lambda * 0.2\lambda$	1	73% at 2.4 GHz	6.8
[40]	$0.17\lambda * 0.1\lambda$	2	65% at 3.5 GHz	5.88
[17]	$0.18\lambda * 0.18\lambda$	0	35% at 915 MHz	10.8
Proposed Work	$0.14\lambda * 0.14\lambda$	1	84% at 868 MHz	42.85

radiation efficiency and gain of the antenna. Nevertheless, such efficiency and gain are acceptable for IoT applications.

The compactness and efficiency of the proposed antenna are finally benchmarked using the following figure of merit (FOM) which is none other than their radiation efficiencies (RE) per unit of electrical area (area normalized to the effective wavelength at the operating frequency of the antenna). Its equation is shown in Eq. 6.3:

$$FOM = RE / (100 * A_{Normalized}) \quad \text{Eq. 6.3}$$

$$\text{with } A_{Normalized} = Area_{Antenna} / \lambda^2 \quad \text{and} \quad \lambda = c / ((\epsilon_r)^{0.5} f)$$

Where the RE denotes the power conversion efficiency of the antenna, the  $A_{Normalized}$  takes into account the active area of the antenna normalized to the square of the largest wavelength,  $\lambda$  is the wavelength,  $c$  is the speed of light,  $\epsilon_r$  is the relative permittivity and  $f$  is the frequency of operation. The FOM of the proposed antenna built is calculated and included in a table for comparison with several state-of-the-art work as presented in literature. Table 6.2 highlights the out performance of the proposed technique and design architecture. This performance maintains both high efficiency values despite the miniaturization aspect of the complete antenna design.



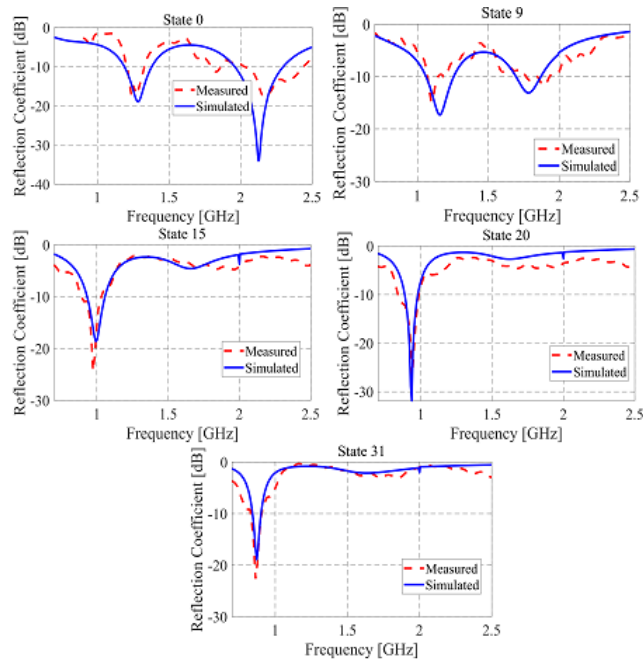


Figure 6.10: Simulated and Measured Reflection Coefficient in dB for different DTC States

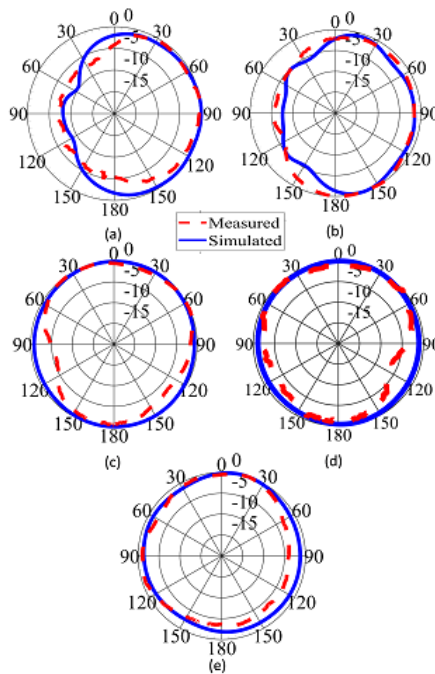


Figure 6.11: The radiation pattern of the antenna at (a) 2.1 GHz, (b) 1.8 GHz, (c) 1 GHz, (d) 915 MHz and (e) 868 MHz from different DTC state at phi 90°

## 6.4 Discussion

A frequency reconfigurable compact semi-bowtie antenna design is proposed in this paper. The antenna is proposed for IoT devices. It operates at the European and US LoRa, GSM and LTE bands. It resorts to only one digital tunable capacitor in order to operate at the required frequency bands. The antenna also presents 84% size reduction at 868 MHz, 82% at 915 MHz and 32% at 1.8 GHz. Also, its gain varies between 0.2 - 2.7 dB while maintaining a high radiation efficiency (88%-98%). The antenna is fabricated and measured where the measurements are in good agreement with the simulations.

# Chapter 7

## Novel Reconfigurable Transmit/Receive System

### 7.1 Introduction

The design of a reconfigurable RF front end transmit/receive (TX/RX) system for IoT communication is presented in this chapter. It targets both European and US ISM bands in addition to the WLAN IEEE 802.11 g commercial wireless standard key specifications. It includes the design of a reconfigurable Filtenna and a reconfigurable bandpass filter as examined in Chapter 4. Also, it explains the choice of the wideband mixer, LNA and the saw filter. Prototypes of the blocks are fabricated and measured. The reception of the reconfigurable RF frontend TX/RX system is then tested. A 433MHz downconverted signal is measured at the IF output of the receiver for different carrier frequencies 868 MHz, 915 MHz and 2.45 GHz.

The main objective of this chapter is in the design of a multi-standard reconfigurable TX/RX system. The TX/RX system is designed to have a superheterodyne architecture [10] in order to be able detect different modulation schemes for different applications.

### 7.2 Block Diagram of the Proposed TX/RX System

A typical block diagram of the proposed system, which incorporates crucial components for both reception and transmission such as lownoise amplification, reconfigurable bandpass filtering, downconversion mixer, and proper detection of an RF signal in ISM and WiFi bands, is presented in Fig. 7.1. The role of each unit is discussed herein.

The RF section of the receiver includes a low noise amplifier (LNA), a re-

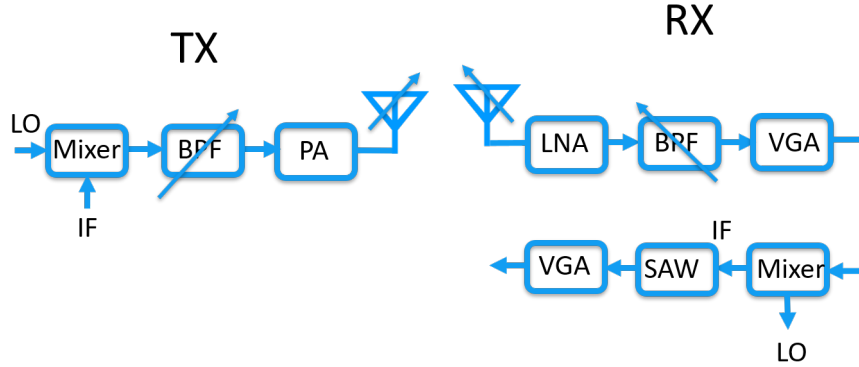


Figure 7.1: Block Diagram of the proposed TX/RX System

configurable RF band-pass filter (BPF), a variable gain RF amplifier as the pre-amplifier of the mixer, and an RF-to-IF down-converter (mixer). Following the down-converter is an IF SAW filter for channel selection and suppressing unwanted mixing products and then an IF variable gain amplifier (VGA).

The I/Q demodulator is the second frequency converter, which down-converts the signal frequency from IF to BB. The demodulator contains two mixers, and it converts the IF signal into I and Q signals i.e.,  $two90^\circ$  phase shifted BB signals. A low-pass filter (LPF) follows the mixer in I and Q each channel to filter out the unwanted mixing products and to further suppress interferers. The filtered I and Q BB signals are amplified by BB amplifiers, and then the ADC converts the amplified BB signals into digital signals for further processing in the digital base-band. It is similar to the superheterodyne receiver that a superheterodyne transmitter also consists of BB, IF, and RF three sections.

The gain control in the IF section probably occupies about 75% of the overall gain control range or more. It is rare to see that the gain control is implemented in the analog BB section for this radio architecture. The reason for this is that the BB section either in the receiver or in the transmitter has I and Q two channels, and it is hard to keep the I and Q channel magnitude imbalance within an allowable tolerance over the BB gain variation range.

In this work, the WLAN IEEE 802.11 g standard and the ISM standard, whose key specifications are listed in Table 7.1, is considered.

### 7.3 Design Considerations for the TX/RX System system

In the superheterodyne TX/RX System, most of the desired signal gain is provided by the IF blocks. At fixed intermediate frequencies, it is relatively easier to obtain high and stable gains. The power consumption for achieving high gain

Table 7.1: Targeted Commercial Wireless Standard Key Specifications

Minimum Requirements	WiFi	LoRa (Europe)	LoRa (USA)
Frequency (MHz)	2.4-2.48 GHz	863-870 MHz	902-928 MHz
Receiver Bandwidth		125-250 KHz	125-500 KHz
Channel Spacing	20 MHz	10 Channels	10 Channels
Modulation	QPSK 1/2 coding rate OFDM	DSSS with Chirp	DSSS with Chirp
Data Rate (Mbps)	16 Mbps	250-50 Kbps	980-21.9 Kbps
Sensitivity	<-79 dB	-100	-100
Dynamic Range	>50	70	70
Adjacent Channel Rejection (dB)	>13	27	27

at IF is significantly lower than that if the same gain is developed at RF.

It is necessary to have a good frequency plan for a superheterodyne TX/RX System to successfully operate over a specified frequency band.

The sensitivity and linearity or the noise figure (NF) and IIP3, of a receiver are tightly dependent on the gain distribution over the receiver chain. To obtain a lower noise figure or a higher sensitivity receiver, it is preferred to make the front-end block from the antenna port through the LNA to the RF down-converter input port with a high gain. In this case, the receiver noise figure may be mainly determined by the front-end block noise figure, and the back section of the receiver chain from the down-converter input to the ADC output has minor impact on the overall noise figure. However, the high front-end gain will degrade the receiver linearity since the overall IIP3 of the receiver decreases with the front-end block gain increase. In receiver design, it is necessary to have proper gain distribution, which is able to take care of the tradeoff between sensitivity and linearity, or noise figure and IIP3, of the receiver for an appropriate performance.

## 7.4 Receiver Performance Evaluation

Three important figures, which are related to the noise figure (NF), gain, and 1dB input compression point (PIN, 1dB) of the crucial receiver blocks, are computed before measuring the reception of the built receiver for different carrier frequencies. These are the receiver noise figure (NFRX), 1dB input compression point (PIN, 1dB), and total dynamic range (TDR).

Table 7.2 presents the computed restrictions in terms of modulation, bit error rate (BER), Carrier to noise ratio, etc.

Table 7.3 is also used to compute the level diagram evaluation of the proposed receiver.

The total noise figure of the receiver. It is found to be approximately 4 dB, which matches the value of the required noise figure to detect and MDS of -133 dBm for both targeted ISM and WLAN IEEE 802.11 g commercial wireless

Table 7.2: Receiver Requirements

Requirements	QPSK	LoRa 868	LoRa 868	LoRa 915	LoRa 915
BER	2%	0.10%	0.10%	0.10%	0.10%
Eb/No (dB) from Fig. 2.37 and BER 2%	3	5	5	5	5
Add increments from LO , filter and I and Q imbalance (dB)	1	1	1	1	1
Bit rate (KHz)	16000	250	50	980	21.9
Spread Factor	NA	12	7	10	7
Noise Bandwidth (KHz)	8000	85334	915	100352	401
Sensitivity	-79	-100	-100	-100	-100
signal power (dBm)	-76	-97	-97	-97	-97
intermodulation Response	-50	-50	-50	-50	-50
Dynamic Range	60	70	70	70	70
delta R	3	3	3	3	3
Carrier to Noise Ratio	7.09	-19.33182095	-6.624510897	-14.10299957	-6.627002578
CNR with added marjin	8	-20	-7	-15	-7

Table 7.3: Receiver Spread Sheet

Reciever Spreed sheet	Antenna	Diplexer	LNA	RF BPF	RF Amplifier	MIXER	IF VGA	IF VGA
Part number	Novel Reconfigurable Filtenna		MAAL-009120	Novel Reconfigurable Filter	MAAL-007304	CSM4T	IDTF1240NBGI	IDTF1240NBGI
current mA			11.5		11.5		160	160
Power Gain dB		-2.6	25.5	-2.6	25.5	-9	-11.5	20
Cascaded Power Gain dB		-2.6	22.9	20.3	45.8	36.8	25.3	45.3
Pout dBm	-107	-109.6	-84.1	-86.7	-61.2	-70.2	-81.7	-61.7
NF dB	0	2.6	1.7	2.6	6.5	9	4	4
Cascaded NF dB		2.6	6.54	6.55	6.59	6.59	6.59	6.6
NF Contribution (%)		39.39	59.7	0.1515	0.6061	0	0	0.1515
IIP3 dBm		100	-6	100	-6	18	47	47
Cascaded IIP3		100	-6	14.3	-6	17.78	41.6	47

standard as presented in Table 7.4 .

To compute the 1dB input compression point (PIN, 1dB) of the receiver, the 1dB input compression points of the crucial blocks, along with their associated gains, are listed in their corresponding data sheets and in Table 7.3 . Table 7.3 also presents the cascaded IIP3 the whole receiver, it then used to calculate the 1dB input compression point of the receiver, and it is found to be 47 dBm. The total dynamic range is 170 dB, which is more than that required for both modulation schemes.

## 7.5 Receiver Design

The Receiver is designed, fabricated and assembled as presented in the Fig. 7.2

For this setup, two frequency generator are placed as the RF and LO generators as shown in Fig. 7.2. The frequency generator connected to the LNA is used to put in an RF signal, where  $F_{RF} = 2.45$  GHz and  $P_{RF} = -10$  dBm, at the input of the reconfigurable receiver. The VCO frequency is represented by another frequency generator, whose output has the following  $F_{LO} = 2.017$  GHz

Table 7.4: Receiver Main Performance Evaluation

Reciever Main Performance Evaluation	QPSK	LoRa 868	LoRa 868	LoRa 915	LoRa 915
Bit rate (KHz)	16000	250	50	980	21.9
Rx Sensitivity (MDS)	-120.3691001	-110.088779	-129.7857891	-109.3847397	-133.3685563
Intermodulation Rejection	108.9127334	102.059186	115.190526	101.5898265	117.5790375

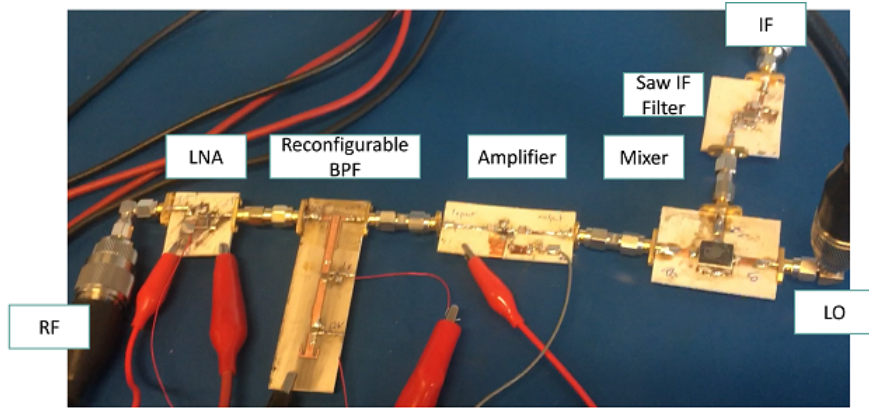


Figure 7.2: Receiver Fabricated System

and  $P_{LO} = -10$  dBm values. The output of the reconfigurable receiver, while its interrelated blocks, is monitored on the signal analyzer. The actual measurement is illustrated in Fig. 7.3. The measured output power of the receiver, which demonstrates a 433MHz downconverted signal for the tested case, is shown in Fig. 7.3.

## 7.6 Transmitter Design

The Transmitter is designed, fabricated and assembled as presented in the Fig. 7.4. The transmission band satisfy the standard spectral mask as shown in Fig. 7.5

For this setup, two frequency sweepers replace the tunable filtenna and the VCO, as shown in Fig. 7.4. The frequency generator connected to the mixer is used to put in an IF modulated signal, where  $F_{IF} = 433$  MHz and  $P_{IF} = 0$  dBm, at the input of the reconfigurable receiver. The VCO frequency is represented by another frequency generator, whose output has the following  $F_{LO} = 2.017$  GHz and  $P_{LO} = 10$  dBm values. The output of the reconfigurable transmitter, while its interrelated blocks, is monitored on the signal analyzer. The actual measurement is illustrated in Fig. 7.6. The measured output power of the system, which demonstrates a 2.454 GHz upconverted signal for the tested case, is shown in Fig. 7.6.

## 7.7 Transmit/Receive Design

The Transmitter and the receiver are now reconfigured and placed as a TX/RX system in order to test the functionality of the whole system with the presence of the reconfigurable filtenna. The system is presented in Fig. 7.7.

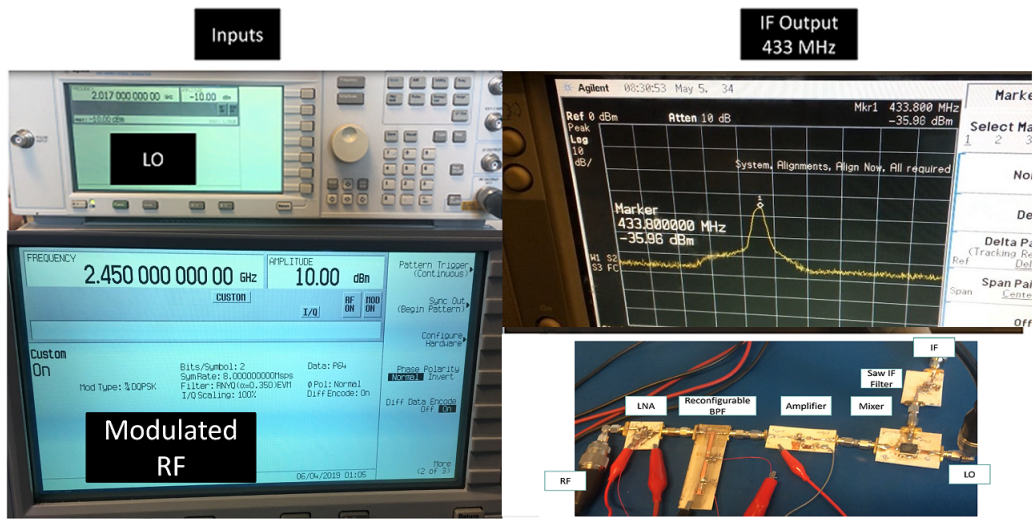


Figure 7.3: Testing Scenario

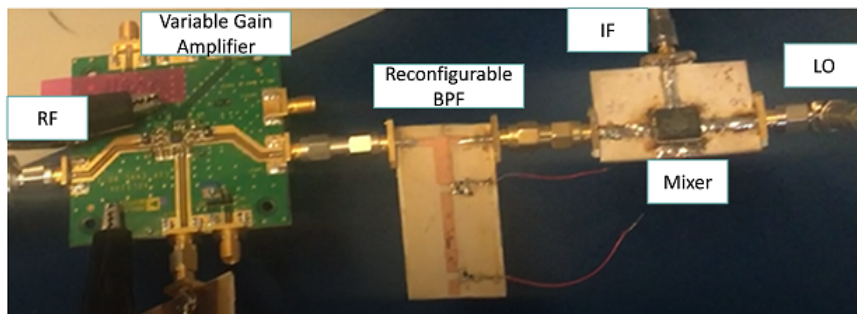


Figure 7.4: Transmitter Fabricated System

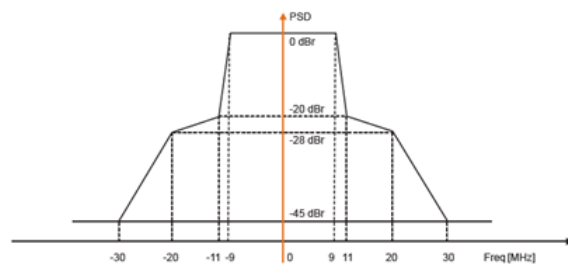


Figure 7.5: Standard Spectral Mask [10]



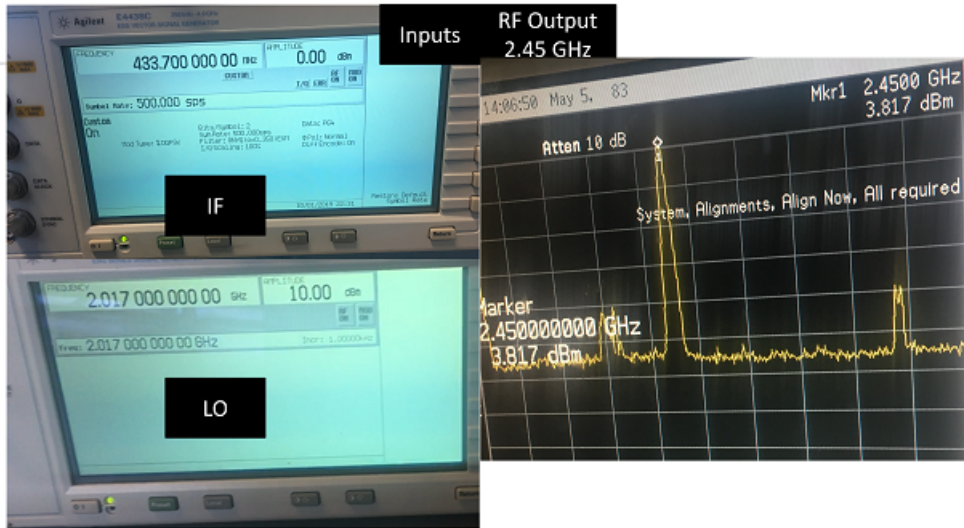


Figure 7.6: Transmitter testing Scenario



Figure 7.7: Assembled TX/RX System

For this setup, two frequency generators are used. The first one provides LO signal for both the transmitter and the receiver as shown in Fig. 7.7. The second generator provides the complex I/Q modulated signal. The frequency generator connected to the mixer is used to put in an IF modulated signal, where  $F_{IF} = 433$  MHz and  $P_{IF} = 9$  dBm, at the input of the reconfigurable receiver. The VCO frequency is represented by another frequency generator, whose output has the following  $F_{LO} = 2.017$  GHz and  $P_{LO} = 10$  dBm values. The output of the reconfigurable transmitter, while its interrelated blocks, is transmitted by the filtenna. On the receiver side, the receiver filtenna captures the modulated RF signal. After this signal passes through the RF receiver block, it gets down-converted into 433 MHz by the mixer, filtered using a SAW filter, amplified using a VGA as shown in Fig. 7.7.

## 7.8 Conclusion

The design of a reconfigurable multi-standard RF frontend TX/RX System is reported in this Chapter. The targeted commercial wireless standard are European ISM, US ISM and WLAN IEEE 802.11 g. This chapter details the design of the Filtenna (receiving antenna), lownoise amplifier (LNA), tunable coupledline bandpass filter, singleended balanced mixer, voltagecontrolled oscillator (VCO), and variable gain IF amplifier receiver blocks. Prototypes of the designed blocks are fabricated and measured. A good agreement is witnessed between the simulated and the measured results. Three measurement setups are then carried out to test the reception of the assembled tunable RF frontend sensing receiver. In each experiment, the IF output of the receiver reveals a downconverted signal in the 433 MHz vicinity.

# Chapter 8

## Conclusions and Future Work

In this dissertation, the design of antennas and a transmit/receive system for mobile and IoT devices is presented. The design process is initiated by investigating a PIFA structure. The PIFA is then reconfigured by relying on a variety of switching techniques. In addition, this reconfigurable miniaturized PIFA is integrated into a MIMO configuration where a new technique for isolation enhancement is proposed. Such enhancement is based on dynamically and selectively trapping the coupling between the antenna elements simultaneously with their operation at the corresponding frequencies. As a result, isolation is highly enhanced in preparation for further integrated antennas in a world of billions of connected devices. The full MIMO system is also analyzed with respect to the various reconfiguration techniques. Conclusions are drawn on the impact of each reconfiguration mechanism on the radiated power, efficiency, gain and power dissipated. Such conclusions define the design of communication systems in any IoT terminal.

As a proof of concept and in order to further enhance these analyses, antennas are designed in extreme miniaturization techniques operating at UHF bands. Such design challenge defies the antenna designer to maintain the necessary needed requirements while satisfying the design constraints. As a result, two reconfigurable antennas are designed and investigated. The first design resorts to only one RF MEMS and maintains high radiation efficiency values despite its elevated miniaturization aspect. The antenna is fabricated and measured where the results agree greatly with simulated ones. The second antenna resorts to a digital tunable capacitor (DTC) in order to tune its operation while avoiding the incorporation of analog and traditional switching components. The proposed digitally tuned antenna operates at the European and US LoRa, GSM and LTE bands. It resorts to only one DTC in order to operate at the required frequency bands. The antenna is fabricated and measured where the measurements are in good agreement with the simulations.

Furthermore conclusions are drawn on the impact of DTC on small antennas' operation. As a last step a transmit/receive system is proposed. This system also includes a reconfigurable filtenna front-end. The reconfigurable filtenna is

Table 8.1: Comparison between Different Switching Techniques

Analysis	Pin Diodes	MEMS	Varactors	DTC
Number of Switches	2	2	1	1
Control	Analog	Analog	Analog	Digital (easily integrated in software defined systems)
Biasing (input dc power)	low DC power requirement (10 mW)	noticeable DC power requirement (171 mW)	high DC power requirements (250 mW)	Extremely Low DC power Requirements (0.13 mW)
Antenna Gain	Abrupt Variation in the Gain	Less Abrupt Variation in the Gain Values	Smooth Transition in the Gain Values	Approximately Constant Gain over Different Frequencies
Power Radiated and Radiation Efficiency	Low Radiation Efficiency can be improved in PIN diode is placed away from the radiating structure	Considerably high radiation efficiency	High radiation efficiency	Considerably high radiation efficiency
Non- Linearity	Non-Linear	Linear	Linear	Linear
Reliability	Reliable	Non-Reliable	Reliable	Reliable

digitally tuned and aims at increasing the channel selectivity and enhancing the filtering ability of the system. The transmit/receive system also relies on dynamic components that are either reconfigurable or wideband in order to cater for the reconfigurable front end.

Some guidelines are presented below can help designers determine which switch to use and when:

1- If the number of switches is a constraint for the antenna designer, then tunable capacitors (DTC and Varactors) are advantageous over ON/OFF switches (PIN Diode and RF MEMS).

2- If the designer is restricted with a low dc input power, DTC become the most suitable choice after which comes pin diode, RF MEMS then varactors in increasing order of dc power consumption.

3- The design of an efficient antenna with high power radiated is always a need. Varactors and DTC have less impact on the antennas' radiation efficiencies than MEMS and pin diodes.

4- Non-linearity affects the antenna performance and radiation efficiency, so linear switches like MEMS and DTC are preferable over varactors and pin diodes.

## 8.1 Future Work

This work can be further extended into a variety of applications and devices that cater for the future of communication well within 5G and beyond. The main future extensions of this work can be summarized in the below:

1- Investigating of the impact of communication efficiency within an increased number of connected devices.

2- Study the interference emanating from neighbouring devices especially in a hyper IoT scenario where a vast number of devices are connected and exist in the vicinity of each other.

3- Investigate and study the enhanced DC isolation with an increased number of antenna elements in a extended MIMO scenario.

- 4- Investigate enhanced isolation and extreme miniaturization aspects in Massive MIMO scenarios
- 5- understand the impact of switching components on the antennas and transceiver systems in a Massive MIMO environment.
- 6- The reconfigurable transceiver system can be further designed on a chip to have an SoC reconfigurable microwave transceiver.
- 7- The analysis of switches can be further extended to mm wave antennas.
- 8- Novel reconfigurable transceivers at mm wave that caters the required standards and frequencies can be designed.

# Appendix A

## Abbreviations

DC	Direct Current
DSSS	Direct Sequence Spread Spectrum
DTC	Digital Tunable Capacitor
GPS	Global Positioning System
GSM	Global System for Mobile Communications
IoT	Internet of Things
ISM	Industrial, Scientific and Medical
LTE	Long Term Evolution
MEMS	Micro-Electromechanical Switch
MIMO	Multiple Input Multiple Output
PIFA	Printed Inverted F Antenna
PIN	Positive-Intrinsic-Negative
QPSK	Quadrature Phase Shift Keying
RF	Radio-Frequency

# Bibliography

- [1] L. Huitema, M. Koubeissi, C. Decroze, and T. Monediere, “Compact and Multiband Dielectric Resonator Antenna with Reconfigurable Radiation Pattern,” *Proceedings of the Fourth European Conference on Antenna and Propagation*, 2010.
- [2] L. H. Trinh, F. Ferrero, L. Lizzi, R. Staraj, and J. Ribero, “Reconfigurable Antenna for Future Spectrum Reallocations in 5G Communications,” *IEEE Antennas and Wireless Propagation Letters*, vol. 15, no. , pp. 1297–1300, 2015.
- [3] L. Yang and T. Li, “Box-folded four-element MIMO antenna system for LTE handsets,” *Electronics Letters*, vol. 51, no. 6, pp. 440–441, 2015.
- [4] B. Mun, C. Jung, M.-J. Park and B. Lee, “A Compact Frequency-Reconfigurable Multiband LTE MIMO Antenna for Laptop Applications,” *IEEE Antennas and Wireless Propagation Letters*, vol. 13, no. , pp. 1389–1392, 2014.
- [5] G. Li, H. Zhai, Z. Ma, C. Liang, R. Yu and S. Liu, “Isolation-Improved Dual-Band MIMO Antenna Array for LTE/WiMAX Mobile Terminals,” *IEEE Antennas and Wireless Propagation Letters*, vol. 13, no. , pp. 1128–1131, 2014.
- [6] A. Boukarkar, X. Qi Lin, Y. Jian, L. Ying Nie, P. Mei, and Yi Qiang Yu, “A Miniaturized Extremely Close-Spaced Four-Element Dual-Band MIMO Antenna System With Polarization and Pattern Diversity,” *IEEE Antennas and Wireless Propagation Letters*, vol. 17, no. 1, pp. 134–137, 2018.
- [7] S.-P. U. Pui-In Mak and R. P. Martins, “Two-step channel selectiona novel technique for reconfigurable multistandard transceiver front-ends,” *IEEE Transactions on Circuits and SystemsI: Regular Papers*, vol. 52, no. 7, pp. 1302–1315, 2005.
- [8] e. a. Yumei Huang, “A high-linearity wcdma/gsm reconfigurable transceiver in 0.13- m cmos,” *IEEE Transactions on Microwave Theory And Techniques*, vol. 61, no. 1, 2013.

- [9] I. Peregrine Semiconductor, “SMP1340 Series: Fast Switching Speed, Low Capacitance, Plastic Packaged PIN Diodes, PE64907 datasheet,” 2017.
- [10] G. Qizheng, *RF System Design of Transceivers for Wireless Communications*. Springer Publishing Company, Incorporated, 1st ed., 2010.
- [11] Statista, “Internet of Things (IoT) connected devices installed base worldwide from 2015 to 2025,” 2015.
- [12] J. Volakis, *Antenna Engineering Handbook*. McGraw-Hill, 2009.
- [13] H. T. Chattha, M. Nasir, Q. H. Abbasi, Y. Huang and S. S. AlJaafreh, “Compact Low-Profile Dual-Port Single Wideband Planar Inverted-F MIMO Antenna,” *IEEE Antennas and Wireless Propagation Letters*, vol. 12, no. , pp. 1673–1675, 2013.
- [14] T. Zhang, R. Li, G. Jin, G. Wei, and M. Tentzeris, “A Novel Multiband Planar Antenna for GSM/UMTS/LTE/Zigbee/RFID Mobile Devices,” *IEEE Transactions on Antennas and Propagation*, vol. 59, no. 11, pp. 4209–4214, 2011.
- [15] C. Lam, and E. Y. Rowell, “Multiple Frequency Band and High Isolation Mobile Device Antennas Using a Capacitive Slot,” *IEEE Transactions on Antennas and Propagation*, vol. 60, no. 8, pp. 3576–3582, 2012.
- [16] M. Zheng, H. Wang and Y. Hao, “Internal Hexa-Band Folded Monopole/Dipole/Loop Antenna with Four Resonances for Mobile Device,” *IEEE Transactions on Antennas and Propagation*, vol. 60, no. 6, pp. 2880–2885, 2012.
- [17] R. Caso, A. Michel, M. Rodriguez-Pino and P. Nepa, “Dual-Band UHF-RFID/WLAN Circularly Polarized Antenna for Portable RFID Readers,” *IEEE Transactions on Antennas and Propagation*, vol. 62, no. 5, pp. 2822–2826, 2014.
- [18] R. Caso, A. Michel, M. Rodriguez-Pino and P. Nepa, “Dual-Band UHF-RFID/WLAN Circularly Polarized Antenna for Portable RFID Readers,” *IEEE Transactions on Antennas and Propagation*, vol. 62, no. 5, pp. 2822–2826, 2014.
- [19] Y. Tawk, J. Costantine and C. G. Christodoulou, *Antenna Design for Cognitive Radio*. Artech House, 2016.
- [20] J. Costantine, Y. Tawk, S. Barbin and C. G. and Christodoulou, “Reconfigurable Antennas: Design and Applications,” *Proceedings of the IEEE Journals*, vol. 103, no. 3, pp. 424–437, 2015.



- [21] J. Kovitz, H. Rajagopalan, and Y. Rahmat-Samii, "Design and Implementation of Broadband MEMS RHCP/LHCP Reconfigurable Arrays Using Rotated E-Shaped Patch Elements," *IEEE Transactions on Antennas and Propagation*, vol. 63, no. 6, pp. 2497–2507, 2015.
- [22] H. Rajagopalan, J. M. Kovitz and Y. Rahmat-Samii, "MEMS Reconfigurable Optimized E-Shaped Patch Antenna Design for Cognitive Radio," *IEEE Transactions on Antennas and Propagation*, vol. 62, no. 3, pp. 1056–1064, 2014.
- [23] J. Costantine, Y. Tawk, J. Woodland, N. Flaum, Ch. G. Christodoulou, "Reconfigurable antenna system with a movable ground plane for cognitive radio," *IET Microwaves, Antennas and Propagation*, vol. 8, pp. 858–863, 2014.
- [24] C.Y. Chiu, J. Li, S. Song and R. D. Murch, "Frequency-Reconfigurable Pixel Slot Antenna," *IEEE Transactions on Antennas and Propagation*, vol. 60, no. 10, pp. 44921–4924, 2012.
- [25] P. Bahramzy, O. Jagielski, S. Svendsen and G. F. Pedersen, "Compact Agile Antenna Concept Utilizing Reconfigurable Front End for Wireless Communications," *IEEE Transactions on Antennas and Propagation*, vol. 62, no. 9, pp. 4554–4563, 2014.
- [26] T. Chiu, C. Hung and K. Hsu, "Reconfigurable resonant module for multi-band antenna design," *IET Microwaves, Antennas and Propagation*, vol. 10, no. 3, pp. 326–332, 2016.
- [27] I. Elfergani, T. Sadeghpour, R. Abd-Alhameed, A. Hussaini and J. Noras, "Reconfigurable antenna design for mobile handsets including harmonic radiation measurements," *IET Microwaves, Antennas and Propagation*, vol. 6, no. 9, pp. 990–999, 2012.
- [28] J. H. Lim, G. T. Back, Y. I. Ko, C. W. Song and T. Y. Yun, "A Reconfigurable PIFA Using a Switchable PIN-Diode and a Fine-Tuning Varactor for USPCS/WCDMA/m-WiMAX/WLAN,," *IEEE Transactions on Antenna and Propagation*, vol. 58, no. 7, pp. 2404–2411, 2010.
- [29] S. Youngje, "Multi-band reconfigurable antenna for mobile handset applications," *IET Microwaves, Antennas and Propagation*, vol. 8, no. 11, pp. 864–871, 2014.
- [30] J.H. Lim, C.W. Song, Z.J. Jin and T.Y. Yun, "Frequency reconfigurable planar inverted-F antenna using switchable radiator and capacitive load," *IET Microwaves, Antennas and Propagation*, vol. 7, no. 6, pp. 430–435, 2013.

- [31] S. Lee and Y. Sung, “Reconfigurable PIFA with a parasitic strip line for a hepta-band WWAN/LTE mobile handset,” *IET Microwaves, Antennas and Propagation*, vol. 9, no. 2, pp. 108–117, 2015.
- [32] S. W. Lee, and Y. Sung, “Compact Frequency Reconfigurable Antenna for LTE/WWAN Mobile Handset Applications,” *IEEE Transactions on Antennas and Propagation*, vol. 63, no. 10, pp. 4572–4577, 2015.
- [33] G. Chaabane, V. Madrangeas, M. Chatras, E. Arnaud, L. Huitema, and P. Blondy, “High-Linearity 3-Bit Frequency-Tunable Planar Inverted-F Antenna for RF Applications,” *IEEE Antennas and Wireless Propagation Letters*, vol. 16, no. , pp. 983–986, 2016.
- [34] Q. Bai, R. Singh, K. L. Ford, T. O’Farrell and R. J. Langley, “An Independently Tunable Tri-Band Antenna Design for Concurrent Multiband Single Chain Radio Receivers,” *IEEE Transactions on Antennas and Propagation*, vol. 65, no. 12, pp. 6290–6297, 2017.
- [35] J. L. Mattei, L. Huitema, P. Queffelec, J. F. Pintos, Ph. Minard, A. Sharahia, B. Jamnier, F. Ferrero, R. Staraj, D. Souriou, and A. Thakur, “Suitability of Ni-Zn Ferrites Ceramics With Controlled Porosity as Granular Substrates for Mobile Handset Miniaturized Antennas,” *IEEE Transactions on Magnetics*, vol. 47, no. 10, pp. 3720–3723, 2011.
- [36] Y. He, Z. Pan, X. Cheng, Y. He, J. Qiao, and M. Tentzeris, “A Novel Dual-Band, Dual-Polarized, Miniaturized and Low-Profile Base Station Antenna,” *IEEE Transactions on Antennas and Propagation*, vol. 63, no. 12, pp. 5399–5408, 2015.
- [37] A. Rida, L. Yang, S. Basat, A. Ferrer-Vidal, S. Nikolaou, and M. Tentzeris, “Design, Development and Integration of Novel Antennas for Miniaturized UHF RFID Tags,” *IEEE Transactions on Antennas and Propagation*, vol. 57, no. 11, pp. 3450–3457, 2009.
- [38] G. Mumcu, K. Sertel, and J. Volakis, “Miniature Antenna Using Printed Coupled Lines Emulating Degenerate Band Edge Crystals,” *IEEE Transactions on Antennas and Propagation*, vol. 57, no. 6, pp. 1618–1624, 2009.
- [39] M. S. Sharawi, *Printed MIMO Antenna Engineering*. Artech House, 2014.
- [40] B. Lee, F. J. Harackiewicz and H. Wi, “Closely Mounted Mobile Handset MIMO Antenna for LTE 13 Band Application,” *IEEE Antennas and Wireless Propagation Letters*, vol. 13, no. , pp. 411–414, 2014.
- [41] M. S. Sharawi, “Printed MIMO Antenna Systems: Current Misuses and Future Prospects,” *IEEE Antennas and Propagation Magazine*, vol. 59, no. 2, pp. 162–170, 2017.

- [42] A. Ramachandran, S. Mathew, V. Rajan, V. Kesavath, “A Compact Triband Quad-Element MIMO Antenna Using SRR Ring for High Isolation,” *IEEE Antennas and Wireless Propagation Letters*, vol. 16, no. , pp. 1409–1412, 2017.
- [43] A. Toktas, “G shaped band notched ultra wideband MIMO antenna system for mobile terminals,” *IET Microwaves, Antennas and Propagation*, vol. 11, pp. 718–725, 2017.
- [44] K. R. Jha, B. Bukhari, Ch. Singh, Gh. Mishra, and S. K. Sharma, “Compact Planar Multi-Standard MIMO Antenna for IoT Applications,” *IEEE Transactions on Antennas and Propagation*, vol. 66, pp. 3327–3336, 2018.
- [45] P.S. Kildal and K. Rosengren, “Correlation and capacity of MIMO systems and mutual coupling, radiation efficiency, and diversity gain of their antennas: simulations and measurements in a reverberation chamber,” *IEEE Communications Magazine*, vol. 42, no. 12, pp. 104–112, 2004.
- [46] Y. Tawk, J. Costantine and C. G. Christodoulou, “Reconfigurable Filtennas and MIMO in Cognitive Radio Applications,” *IEEE Transactions on Antennas and Propagation*, vol. 62, no. 3, pp. 1074–1083, 2014.
- [47] S. Saeed, C. Balanis, and C. Birtcher, “Inkjet-Printed Flexible Reconfigurable Antenna for Conformal WLAN/WiMAX Wireless Devices,” *IEEE Antennas and Wireless Propagation Letters*, vol. 15, no. , pp. 1979–1982, 2016.
- [48] P. Y. Qin, Y. J. Guo, L. Y. Ji, “A Wideband Polarization Reconfigurable Antenna With Partially Reflective Surface,” *IEEE Transactions on Antennas and Propagation*, vol. 64, no. 10, pp. 4534–4538, 2016.
- [49] W. Lin, H. Wong, and R. W. Ziolkowski, “Wideband pattern-reconfigurable antenna with switchable broadside and conical beams,” *IEEE Antennas and Wireless Propagation Letters*, vol. 16, pp. 2638–2641, 2017.
- [50] M. Ng Mou Kehn, . Quevedo-Teruel, and E. Rajo-Iglesias, “Reconfigurable loaded planar inverted-f antenna using varactor diodes,” *IEEE Antennas and Wireless Propagation Letters*, vol. 10, pp. 466–468, 2011.
- [51] F. A. Asadallah, J. Costantine, Y. Tawk, and C. G. Christodoulou, “Isolation Enhancement in MIMO Reconfigurable PIFAs for Mobile Devices,” *Proceeding in the IEEE 11th International European Conference on Antennas and Propagation*, pp. 3803–3805, March 2017.
- [52] S. Inc., “SMP1320 Series: Fast Switching Speed, Low Capacitance, Plastic Packaged PIN Diodes, SMP 1320-079LF datasheet,” 2002.

- [53] J. Tech., “High Frequency Ceramic Solutions,” 2015.
- [54] A. Devices, “Wideband, 40 dB Isolation at 1 GHz, CMOS 1.65 V to 2.75 V, SPST Switches, ADG 901 datasheet,” 1965.
- [55] S. Inc., “SMV1247-SMV1255 Series: Hyperabrupt Junction Tuning Varactors, SMV1247-SMV1255 datasheet,” 2002.
- [56] G. Saggio, *Principles of Analog Electronics*. Hoboken: CRC Press, 2015.
- [57] G. Rebeiz, *RF MEMS*. Hoboken, NJ: Wiley-Interscience, 1st ed., 2004.
- [58] S. Inc., “Design With PIN Diodes, SMP 1340-079LF application note,” 2002.
- [59] S. Inc., “SMVXX Product Brief,” 2014.
- [60] A. Devices, “ADG9xx Wideband CMOS Switches,” 2014.
- [61] M. Pozar, *Microwave Engineering*. John Wiley and Sons, 1998.
- [62] P. Gardner, M. R. Hamid, P. S. Hall, J. Kelly, F. Ghanem, and E. Ebrahimi, “Reconfigurable Antennas for Cognitive Radio: Requirements and Potential Design Approaches,” *Institution of Engineering and Technology Seminar on Wideband, Multiband Antennas and Arrays for Defence or Civil Applications*, p. 8994, 2008.
- [63] B. E. CareySmith, P. A. Warr, P. R. Rogers, M. A. Beach, G. S. Hilton, “Flexible frequency discrimination subsystems for reconfigurable radio front-ends,” *EURASIP Journal on Wireless Communications and Networking*, vol. 3, p. 354363, 2005.
- [64] W. Tang; J. S. Hong, and Y. H. Chun, “Compact Tunable Microstrip Band-pass Filters with Asymmetrical Frequency Response,” *38th European Microwave Conference (EuMC)*, p. 599602, 2008.
- [65] H. L. Zhang, H. L. Zhang, and B. J. Hu, “Tunable bandpass filters with constant absolute bandwidth,” *9th International Symposium on Antennas Propagation and EM Theory (ISAPE)*, p. 12001203, 2010.
- [66] Y. Tawk, J. Costantine, and C. G. Christodoulou, “A Varactor-Based Reconfigurable Filtenna,” *IEEE Antennas and Wireless Propagation Letters (AWPL)*, vol. 11, p. 716719, June 2012.
- [67] A. H. Ramadan, M. Al-Husseini, K. Y. Kabalan, A. El-Hajj, Y. A. Tawk, C. G. Christodoulou, and J. Costantine, “A narrowband frequency-tunable antenna for cognitive radio applications,” *6th European Conference on Antennas and Propagation (EUCAP)*, p. 32733277, April 2012.

- [68] I. STMicroelectronics, “SMP1320 Series: Fast Switching Speed, Low Capacitance, Plastic Packaged PIN Diodes, STM32 Microcontrollers datasheet,” 2019.
- [69] M. W. Young, S. Yong, and J. T. Bernhard, “A Miniaturized Frequency Reconfigurable Antenna with Single Bias, Dual Varactor Tuning,” *IEEE Transactions on Antennas and Propagation*, vol. 63, no. 3, pp. 946–951, 2015.
- [70] J. Oh and K. Sarabandi, “A Topology-Based Miniaturization of Circularly Polarized Patch Antennas,” *IEEE Transactions on Antennas and Propagation*, vol. 61, no. 3, pp. 1422–1426, 2013.
- [71] R. M. Bichara, F. A. Asadallah, J. Costantine, and M. Awad, “A Miniaturized Folded Antenna for IoT Devices,” *Proceeding in the IEEE International Symposium on Antenna Measurements and Applications*, pp. 1–2, September 2018.
- [72] M. Fallahpour, M. Tayeb Ghasr, and R. Zoughi, “Miniaturized Reconfigurable Multiband Antenna For Multiradio Wireless Communication,” *IEEE Transactions on Antennas and Propagation*, vol. 62, no. 12, pp. 6049–6059, 2014.
- [73] C. A. Balanis, *Modern Antenna Handbook*. John Wiley and Sons, 2007.
- [74] K.L.Wong and K.P.Yang, “Modified planar inverted F antenna,” *IEEE Electronics Letters*, vol. 34, no. , pp. 7–8, 1998.
- [75] J. Volakis, Chi-Chih Chen, and K. Fujimoto, *Antennas: Miniaturization Techniques and Applications*. McGraw-Hill, 2010.
- [76] R. Ludwig and G. Bogdanov, *RF Circuit Design Theory and Applications*. New Jersey: Pearson Education, 2009.
- [77] Zh. Su, K. Klionovski , R. M. Bilal, and A. Shamim, “A Dual Band Additively Manufactured 3-D Antenna on Package With Near-Isotropic Radiation Pattern,” *IEEE Transactions on Antennas and Propagation*, vol. 66, no. 7, pp. 3295–3305, 2018.
- [78] “ISM-Band and Short Range Device Antennas, SWRA046A, application report,” *Application Report*, 08-2005.
- [79] N. Nguyen-Trong, A. Piotrowski, L. Hall, and Ch. Fumeaux, “A Frequency- and Polarization-Reconfigurable Circular Cavity Antenna,” *IEEE Antennas and Wireless Propagation Letters*, vol. 16, no. , pp. 999–1002, 2017.

- [80] Chang Ch., Lin W., Lin Y., and Lio W., “Diversity Antenna Design for Compact Devices of IoT Uses,” *IEEE International Workshop on Electromagnetics: Applications and Student Innovation Competition*, pp. 1–3, July 2016.
- [81] F. Ferrero and L. Lizzi, “Feasability of an Ultra Narrow Band Antenna for The Internet of Things,” *IEEE International Symposium on Antennas and Propagation*, pp. 776–777, July 2015.
- [82] Tomattal P., Gaddil R., Morrelll L., Joshil V., Bishop B., “Radiated Efficiency of Aperture Tuned Antennas: Comparison of MEMS Digital Variable Capacitor and Fixed Ceramic Capacitors,” *IEEE MTT-S International Microwave Symposium*, pp. 1–4, 2014.
- [83] Sh. L. Chen, P. Y. Qin, W. Lin, Y. J. Guo, “Pattern-Reconfigurable Antenna with Five Switchable Beams in Elevation Plane,” *IEEE Antennas and Wireless Propagation Letters*, vol. 17, pp. 454–457, 2018.
- [84] T. A. Milligan, *Modern Antenna Design*. Wiley, 2005.
- [85] K. Fujimoto and H. Morishita, *Modern Small Antennas*. Cambridge, 2013.